EVALUATING THE PERFORMANCE OF UNDERWATER ACOUSTIC ARRAYS FOR MULTI-ANGLE SWATH BATHYMETRY APPLICATIONS

by

Ying Wang

B.A.Sc, Xi'an University of Technology, 2000

THESIS SUBMITTED IN PARTIAL FULFILLMENT
OF THE REQUIREMENTS FOR THE DEGREE OF
MASTER OF APPLIED SCIENCE
In the School
of
Engineering Science

SIMON FRASER UNIVERSITY

Summer 2005

APPROVAL

Name: Ying Wang

Degree: Master of Applied Science

Title of Thesis: Evaluating the Performance of Underwater Acoustic Arrays for Multi-Angle Swath Bathymetry Applications

Examining Committee: Dr. Dong In Kim, Chair
Professor of Engineering Science
Simon Fraser University

Dr. John S. Bird, Senior Supervisor
Professor of Engineering Science
Simon Fraser University

Dr. Rodney Vaughan, Supervisor
Professor of Engineering Science
Simon Fraser University

Dr. Andrew H. Rawicz, Examiner
Professor of Engineering Science
Simon Fraser University

Date Approved: July 22, 2005

SIMON FRASER UNIVERSITY

PARTIAL COPYRIGHT LICENCE

Abstract

Transducer array performance is widely recognized as a significant factor in determining the accuracy of target detection and bottom imaging in sonar systems. This thesis proposes methods to evaluate the performance of multi-element acoustic arrays used in a multi-angle swath bathymetry sonar system. The evaluation of array performance is accomplished through measurements of beam patterns, the inter-element spacing, and crosstalk between array elements. The Beam Pattern Measurement System developed by the Underwater Research Lab is used to produce beam patterns from which the inter-element spacing is estimated by applying the inverse Fourier Transform. The crosstalk between array elements is investigated by exciting a single element and measuring the phase and magnitude of induced signals on non-excited array elements. A coupling matrix is constructed from measurements and used to predict the impact of crosstalk on the beam pattern and angle-of-arrival estimation with some limitations. The techniques developed to evaluate array performance are applied to three arrays and the results are presented in this thesis.

Acknowledgements

I would like to express my gratitude to all those who made it possible for me to complete this thesis. I would like to thank my supervisor, Dr. John S. Bird, for his continual support and guidance throughout the research for this thesis. It is really a great honor to work with him. I would also like to thank Dr. Rodney Vaughan and Dr. Andrew H. Rawicz. I value the opinions and time taken by them. I want to thank all my colleagues in the Underwater Research Lab, Jinyun Ren, Sabir Asadov, and Geoff Mullins, for their help and valuable hints. Also, my friends, Jinze Li and Dong Sun, both of whom helped me with the thesis writing and defense, encouraged and supported me, were of great help in the difficult times of my thesis work. Finally, I appreciate my parents, uncle and brother in China for their consistent support, understanding and trusting me.

Table of Acronyms

Sonar	Sound Navigation and Ranging
URL	Underwater Research Laboratory
AOA	Angle of Arrival
SBS	Swath Bathymetry Sidescan
MASB	Multi-angle Swath Bathymetry
BPMS	Beam Pattern Measurement System
FPGA	Field Programmable Gate Array
ICS	Interactive Circuits and System Ltd.
RMS	Root-mean-square
SNR	Signal-to-nose ratio
GUI	Graphical User Interface
FT	Fourier Transform
IFT	Inverse Fourier Transform
GPIB	General Purpose Interface Bus

Table of Contents

List of Figures

List of Tables

Chapter 1

Introduction

It is recognized that the acoustic channel is the only feasible means of underwater communications over any appreciable distance [1]. *Sonar*, derived from the acronym for Sound Navigation and Ranging, is one of the most important applications of the underwater acoustic communication channel. It uses transmitted and reflected underwater sound waves to detect and locate submerged objects or measure distance. Over the last several decades, sonar systems have improved and are widely used to explore the underwater world in applications such as oceanographic research, navigation, submarine detection, mine location and bottom mapping.

This thesis outlines a unique bottom imaging sonar system developed by the Underwater Research Lab (URL) at Simon Fraser University, and then focuses on the characteristics of the multi-element transducer arrays used in this sonar system and evaluates their performance.

1.1 Motivation for Research

The primary objective of this research is to evaluate the performance of multi-element transducer arrays used in multi-angle swath bathymetry sonar systems. This evaluation includes measurement of beam patterns, estimation of the inter-element spacing,

and investigation of crosstalk and estimating the impact of crosstalk on array performance.

The array beam pattern describes the response of the transducer array as a function of angle relative to the array. The inter-element spacing is important because the accuracy of target location in a multi-angle swath bathymetry sonar depends on the accuracy of the measured relative positions of the array elements. The overall performance of the sonar system is therefore dependent on the beam pattern and knowledge of the inter-element spacing, and investigating these characteristics is central to this research work.

Another area of focus in this work is the investigation of crosstalk in multi-element arrays for narrow band sonar systems. Many other aspects of array performance have been well analyzed including the impact of noise, pulse length, multi-path interference, and footprint shift effects [2, 3, 4], but crosstalk between different transducer elements has been either neglected or modelled with computationally complex models. For example, in [5] a computer model is proposed for crosstalk but it requires an accurate and complex geometrical description of the array. Since crosstalk can have a significant effect on array performance, a goal of this thesis is to propose a simple yet accurate experimentally based method by which crosstalk is easily measured and that does not require a detailed description of the array.

1.2 Contribution and Scope of Research

There are two major contributions of this research work. (1) An algorithm is designed to estimate the distance between elements of linear transducer arrays. This is accomplished by applying the inverse Fourier Transform to beam pattern data collected from the transducer. The accurate estimation of inter-element distance is crucial to

estimating target location because the calculation of the arrival angle partially depends on the spacing. Prior to my research, inter-element distances of transducer arrays were usually assumed to be identical to their designed values, which is not likely correct. Furthermore, the estimation of inter-element distance makes it possible to employ a transducer array for target location even if its internal geometrical parameters were previously unknown. (2) A simple and practical method is developed to quantitatively measure crosstalk of different transducer arrays, and to provide important insight into its effects on transducer performance. Before this research work, the crosstalk level was estimated approximately from the variation between the actual individual beam pattern of each transducer element and the ideal one [6]. However, a specialized measurement system is a required to obtain beam patterns. With the approach proposed in this thesis, the crosstalk level can be measured with common test instruments (function generator and oscilloscope). Crosstalk levels can also be estimated by numeric methods, but these methods require detailed geometrical and material information for the arrays [5]. By comparison, the method proposed in this thesis can be used to explore crosstalk without a geometrical or material description of the arrays. Furthermore, the results of the crosstalk measurements give information related to the impact of crosstalk on beam patterns and angle-of-arrival estimation.

In this thesis, we investigate only the steady state beam patterns and crosstalk, and do not consider the transient effects. Investigating the transient effects can provide a means to separate electrostatic and acoustic crosstalk between array elements, but is considered to be beyond the scope of this thesis. Also, this thesis focuses only on linear multi-element arrays composed of elements with a large ratio of length to thickness. Crosstalk in such arrays is less complicated than that in arrays with similar length and thickness, so the proposed methods to measure crosstalk and analyze the impact

of crosstalk may not be applicable to other arrays. Finally, the analysis of crosstalk effect on array performance is done under the assumption of an infinite boundary. This assumption is not always satisfied as housing effects may contribute to crosstalk. Thus, neglecting housing effects decreases the accuracy of estimating the impact of crosstalk on array performance. Nevertheless, housing effects are usually evident and since the goal is to design arrays without housing interactions characterizing them was considered not necessary.

1.3 Outline of Research

This thesis is organized into five chapters. This chapter introduces the principles and historical development of sonar systems to place my work in context. Chapter 2, Beam Pattern and Beam Pattern Measurement System, describes the system in the Underwater Research Lab at Simon Fraser University used to measure beam patterns of transducers. In Chapter 3, Element Spacing of Transducer Arrays, a method to determine distance between array elements is examined. Chapter 4, Crosstalk Measurement and Analysis, explains what crosstalk is, proposes a method to measure it, explores its causes, and analyzes its effects on transducer performance. Finally, Chapter 5 summarizes the research work, and suggests directions for future work.

1.4 Background

Sonar remotely detects and locates objects by taking advantage of the behavior of sound in water. There are two fundamental categories of sonar systems: *passive* or *active*. Passive sonars are essentially "listening" devices that respond to sounds emitted by objects in water. Such instruments can be used to detect seismic events, ships, submarines, and marine creatures - anything that emits sound on its own.

Active sonars are devices that produce sound waves of specific controlled frequencies and durations and listen for the echoes of these emitted sounds returned from remote objects in the water. For example, sonars used to measure ocean depths are active sonars because they emit a sound pulse and listen for the echo from the bottom [7]. The sonar systems discussed in this thesis are all active sonars.

This section gives a brief description of sonar systems, and is divided into two subsections. The first one introduces the fundamental principles of an active sonar system; and the second one outlines the evolution of the multi-angle swath bathymetry sonar system specific to this thesis.

1.4.1 Components and Principles of an Active Sonar System

Typically, an active sonar system is composed of four basic components: a control and data processing device, a transmitter, a receiver, and a transducer.

The operating sequence of an active sonar is as follows: (1) The control and data processing device signals the transmitter system to produce a sound pulse, or *ping*. (2) The transmitter generates an oscillating electric signal with frequency characteristics that can be uniquely distinguished. (3) The transmit transducer converts the oscillating electric signals into acoustic signals that propagate through the water. (4) Upon the return of the sound waves as echoes from the sea floor or other targets in the water, the receive transducer converts the sound waves back into electrical signals. (5) The receiver amplifies the electrical signals and passes them on to the control and data processing device. (6) The control and data processing device records and processes the amplified signals and then triggers the next ping [8].

In underwater acoustics, the transducer refers to a diversity of devices that are capable of providing an acoustic output in response to another form of input, or another form of output in response to an acoustic input. The main forms of input or

output are mechanical, thermal, magnetic, and electrical. For this thesis, the class of acoustic transducers that perform a conversion between electrical and acoustic energy is of interest. A transducer that converts electrical signals into acoustic signals is called a projector, and a transducer that converts acoustic signals into electrical signals is called a hydrophone. When an electrical field is applied to a projector, the projector will change shape, producing mechanical vibrations that are transmitted into the water as oscillating pressures or sound waves. Conversely, when acoustic waves arrive at a hydrophone, the hydrophone vibrates in response to the pressure changes and produces a voltage that corresponds to these changes.

Knowledge of transducer material properties is key in determining the performance of the transducer. Various materials, such as nickel, terfenol and ceramic, have found wide use in underwater acoustic transducers [9]. The most popular materials, however, are piezoelectric ceramics due to their superior piezoelectrical characteristics [9].

Also, the shape of transducers is designed to meet specific requirements for underwater applications. For example, spherical transducers are omnidirectional while rectangular bars can discriminate direction.

1.4.2 Development of Sonar Systems

The first sonar system was invented in 1906 by Lewis Nixon, as a way of detecting icebergs. Interest in sonar increased during World War I to enable detection of enemy submarines. In 1915, Paul Langevin invented the first sonar system capable of detecting submarines. It used the piezoelectric properties of a quartz crystal to convert electrical signals to underwater compression waves and vice versa. Later on, with the invention and refinement of acoustic transducers, more advanced forms of sonar were developed. Historically, the simplest sonar system, the single-beam depth sounder,

evolved gradually to today's modern multi-beam, sidescan, swath bathymetry sidescan and multi-angle swath bathymetry sonars [7].

Recently, the performance of sonar systems has improved considerably, particularly because of the availability of high speed digital signal processing hardware and software. At the same time, well-designed acoustic transducers also significantly improve the measurement accuracy and resolution achievable. Especially, recent research by John Bird and Paul Kraeutuer used a small linear transducer array of only six piezoelectric elements to successfully implement a multi-angle swath bathymetry sonar [10].

1.4.2.1 Single-Beam Depth Sounder

The *single-beam depth sounder* is the earliest and most basic sonar system. It uses a projector to generate a sound pulse and transmit it vertically down into the water. The sound pulse propagates through the water, and is reflected back upon striking the ocean bottom. The projector which generated the sound pulse now acts as a hydrophone to detect the first echo. The time between the generation of the sound pulse and the earliest detection of the first echo is used to calculate the depth of the bottom, using a known velocity of sound in water.

The single-beam depth sounder is simple and easy to build, but its characteristics limit the measurement to a point that is exactly under the transducer. To image an area of sea floor, a laborious grid of measurements is required. It also assumes the sea floor is relatively flat, otherwise the first echo may not be from the point directly below the transducer [7].

1.4.2.2 Multibeam Sonar

In order to improve the single point measurement of the single-beam depth sounder, *multibeam sonar* was developed to image more than one point with a single ping. In this system, neighboring transducer elements interfere with each other constructively or destructively to provide specific look directions. Therefore, projector arrays and hydrophone arrays are capable of generating and detecting sound waves whose amplitudes vary as a function of angular location. Furthermore, some systems take advantage of electronic *beamsteering*, where digital signal processing is used to process the waves simultaneously so as to generate the effect of "steering" a beam. A major drawback of multibeam sonar systems, however, is that they require a large number of transducer elements to achieve high angular resolution, which is very costly [7].

1.4.2.3 Sidescan Sonar

To minimize the cost problem encountered with multibeam sonar, *sidescan sonar* was developed to generate high-resolution images for lower cost. The fundamental principle of this technique is actually similar to that of a single-beam depth sounder. However, unlike a single-beam echo sounder which is pointed downwards and only records the time between sound generation and the arrival of the first return echo, sidescan sonar is pointed sideways and collects a time sequence of backscattered signals after the first echo. The first bottom echo is received, followed by continuous returns from points further and further away from the first scatterer. By analyzing the relationship between signal magnitude and time, a sidescan sonar is able to yield information not only about the distance to the seabed, but also the backscatter strength of the seabed, thus giving clues to its material composition [11]. However, a sidescan sonar can only produce two dimensional images and can not determine the

depth of each point in the image.

1.4.2.4 Swath Bathymetry Sidescan Sonar

With a two-element transducer array, *swath bathymetry sidescan* (SBS) sonar can build three dimensional underwater images. The method utilizes the phase difference between two transducer elements to obtain the angle-of-arrival (AOA) of targets. Figure 1.1 helps explain the underlying principle of SBS sonar.

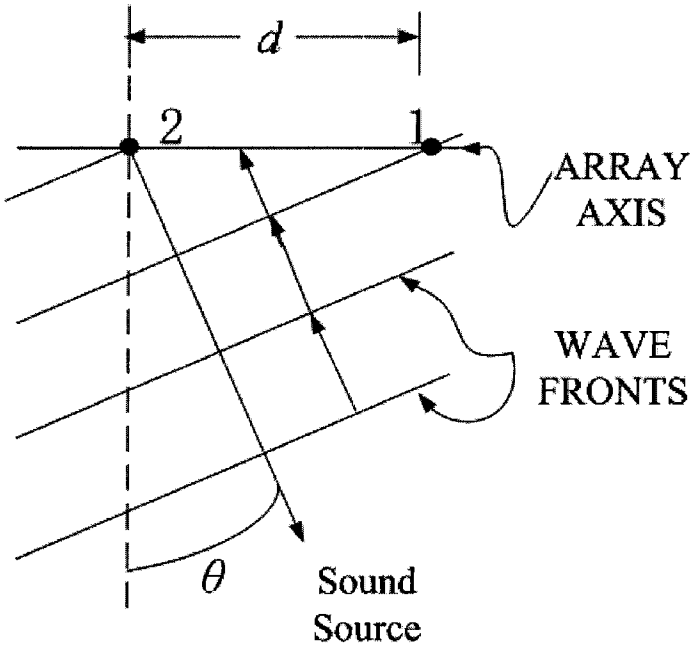

Figure 1.1: Transducer array in an SBS sonar

As shown in Figure 1.1, two transducer elements, labeled as 1 and 2, are spaced with distance d. The AOA, θ, refers to the angle between the direction of the signal and the plane perpendicular to the hydrophone array axis, and is also named the *physical angle*. The phase difference between two adjacent elements of the transducer array corresponding to the signal from direction θ, is defined as the *electrical angle*

and is obtained from:

$$\phi = 2\pi \frac{d}{\lambda} sin\theta \tag{1.1}$$

where d is the distance between elements of the transducer array, and $\lambda = c/f_c$ is the wavelength. The sound speed, c, is approximately 1500 m/s in water.

The position of a target is determined by the AOA together with the propagation time for the signal to travel from the transducer to the seabed and from the seabed back to the transducer. Because the transducer only contains two elements, the system works when only one target is present at a given distance. In other words, only one angle-of-arrival can be estimated. In more complex situations, where more than one signal arrives at the hydrophone simultaneously, the phase measurement from the two-element SBS system is corrupted. This produces a distorted underwater image. Although this limitation impairs its overall acceptance, SBS sonar is still widely used in less demanding bottom imaging applications [7].

1.4.2.5 Multi-angle Swath Bathymetry Sonar

In 1997, John Bird and Paul Kraeutuer constructed a *multi-angle swath bathymetry* (MASB) sonar that estimates the AOA of multiple reflected signals arriving concurrently at a transducer array [10]. MASB sonar employs a transducer array consisting of N equally spaced elements (N is usually 6), and has successfully produced three dimensional images of the bottom [12, 13]. The geometry for this system is illustrated schematically in Figure 1.2, where d is the space between two adjacent transducer elements, and r is the distance between the scatterers and the transducer array.

In the MASB system, adaptive filters, such as Least Squares, Least Mean Squares, etc, are used to estimate the angle-of-arrival of targets from observed data. As many as $N-1$ targets can be located using an N-element transducer array with this system. In the signal processing algorithms, it is assumed that the inter-element spacing is

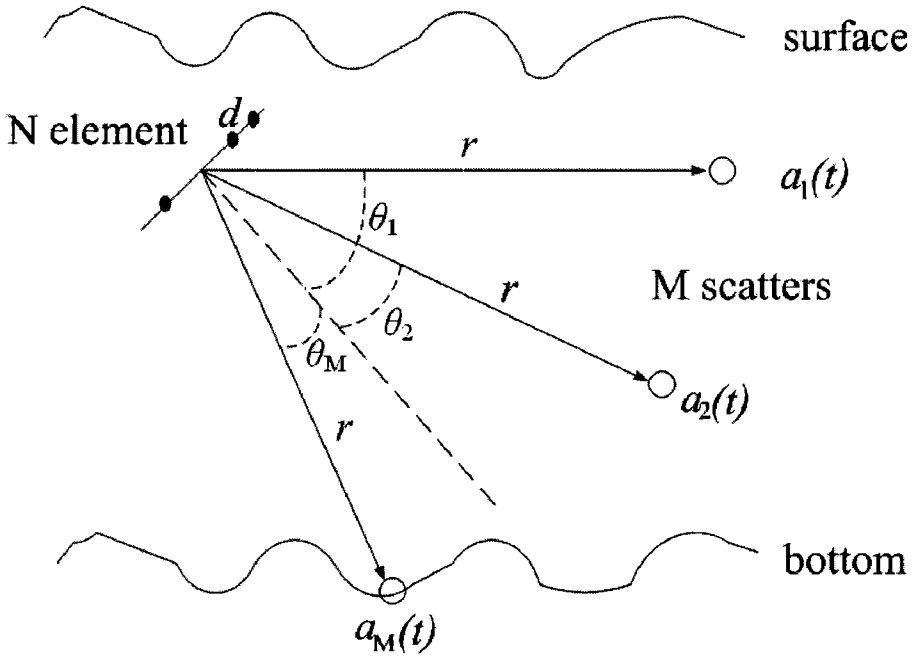

Figure 1.2: N-element transducer array in an MASB sonar

known, and that there is no crosstalk between array elements. This thesis addresses the situation where neither of these assumptions is satisfied, and proposes methods to estimate the inter-element spacing and to explore crosstalk levels between elements.

Summing up, the historical progression of sonar systems was single-beam depth sounder, multi-beam sonar, sidescan sonar, SBS sonar and finally MASB sonar. It is the MASB and their multi-element transducer arrays that are utilized in the URL, and are the focus of this thesis.

Chapter 2

Beam Pattern and Beam Pattern Measurement System

This chapter describes beam patterns of transducer arrays and the Beam Pattern Measurement System (BPMS) used in the Underwater Research Lab. The chapter is divided into three sections: the first section describes beam patterns; the second section describes the BPMS in detail; the last section demonstrates the graphical user interfaces utilized to perform beam pattern measurements and display beam patterns.

2.1 Beam Patterns

This section describes beam patterns and presents ideal beam patterns for an individual transducer element and an element that is embedded in a transducer array. To provide a general picture of the transducer arrays under consideration in this thesis, the front view and side view of a multi-element transducer array are illustrated in Figure 2.1. A detailed description of the configuration of the multi-element transducer arrays can be found in Chapter 4.

Generally speaking, the beam pattern, denoted by $B(\theta)$ in this thesis, describes a transducer's response to a plane-wave acoustic signal as a function of angular direction relative to the transducer, and is determined primarily by the shape of the transducer.

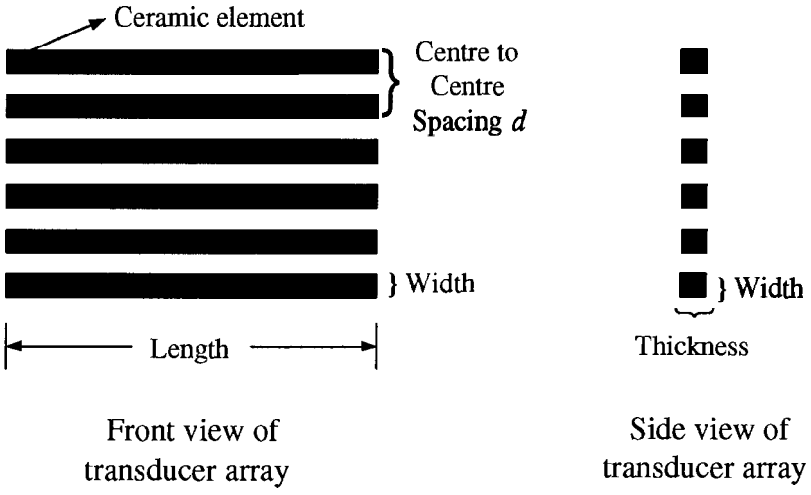

Figure 2.1: Typical configuration of a six-element transducer array

The beam pattern of a transducer is reciprocal, which means that the beam pattern will be the same whether the transducer is used as a projector or a hydrophone. Beam patterns are quite complex because in the real world they are three-dimensional. To simplify the plots, a Cartesian or polar coordinate is used to show the beam in the plane of interest which is perpendicular to the long dimension of the array. For ease in use and maximum versatility, the beam pattern plots are usually shown on a decibel scale.

Transducers can be designed to have different types of beam patterns, from omnidirectional to very narrow. For example, a spherical transducer has an omnidirectional beam pattern, and provides no direction discrimination, while a line transducer has a directional beam pattern that varies as a function of spatial angle. The width of the beam pattern between points 3 dB down from the peak is generally defined as *beamwidth*, and represented in this thesis by ψ_B. Figures 2.2 and 2.3 plot an omnidirectional and directional beam pattern versus spatial angle θ in both Cartesian and polar coordinates. As shown in 2.2 and 2.3, the omnidirectional beam pattern has

equal response in the range of $[-90^0, 90^o]$, and the directional beam pattern has a beamwidth of about 20^o.

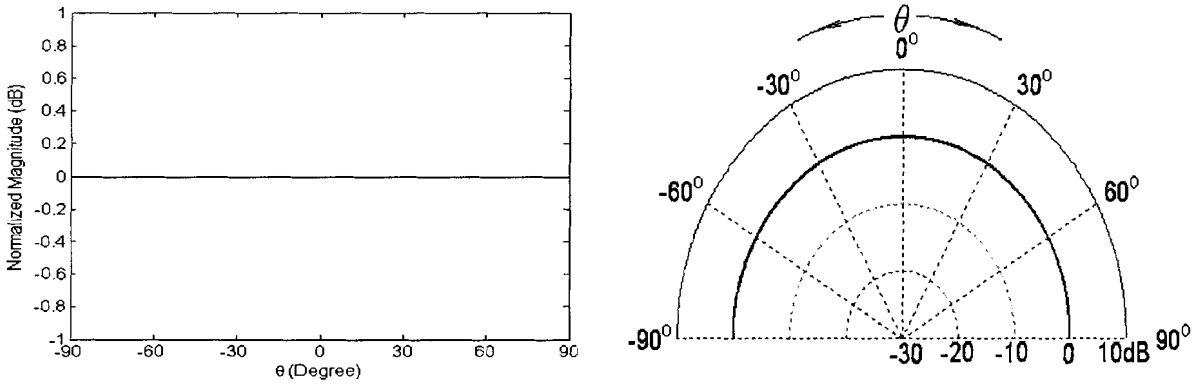

(a) (b)

Figure 2.2: Omnidirectional beam pattern in a (a) Cartesian and (b) polar coordinate

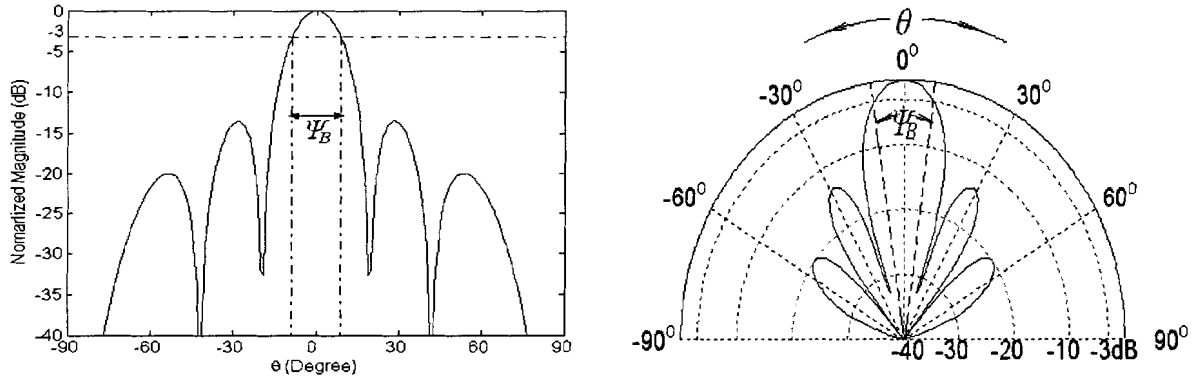

(a) (b)

Figure 2.3: Directional beam pattern in a (a) Cartesian and (b) polar coordinate

For a line transducer with a length of L m, the beamwidth is approximated by [8]:

$$\psi_B \approx 50\frac{\lambda}{L} \tag{2.1}$$

where λ is the wavelength, and ψ_B is the beamwidth in degrees and depends on the ratio of wavelength to transducer dimension. For a directional beam pattern

as shown in Figure 2.3, a point with zero response (-∞ in dB) is called a null and the beam pattern between two nulls is called a lobe. The central biggest lobe is called the main lobe, while the other lobes are called side lobes. As the ratio of wavelength to transducer dimension becomes smaller, the beamwidth decreases, and the main lobe becomes narrower, accompanied by an increase in the number of side lobes. Theoretically, the first side lobe for a uniform line transducer is at -13 dB [9]. Side lobes are undesirable because they can produce spurious signals from strong off-axis scatterers, and result in artifacts in the image. Consequently, for a particular application, a compromise has to be reached between the beamwidth and level of side lobes. *Shading* (varying the magnitudes of the driving signals across a transducer array) is used to trade off beamwidth and side lobe level for a linear transducer array [9]. In beam steered sonar systems, the beamwidth is typically used as a measure of the angular resolution. Hence, angular resolution is a function of the dimension of the transducer [8].

A rectangular transducer element is treated as a line source, with a length equal to the edge of the rectangular element parallel to the plane of the beam pattern under consideration [9]. Since the beam patterns examined in this thesis are in the plane perpendicular to the array, it is the width of the transducer elements as shown in Figure 2.1 that is considered for beamwidth. The transducer arrays (A, B and C) investigated in this thesis are composed of rectangular elements with small width compared to the wavelength. For example, the ratio of the wavelength to width is about 4.4 in array A. Therefore, the individual transducer element of the arrays under investigation is characterized by an approximately omnidirectional beam pattern.

When a transducer element is assembled into an array as shown in Figure 2.1, its beam pattern is affected by the boundary or baffle. In the case that the acoustical

impedance of the material between the piezoelectric ceramic elements is much lower than that of the elements (i.e., soft baffle condition), the pattern shaping function of each single element is a cosine function [14] as shown in Figure 2.4, with resulting beamwidth of about 90^o. The spaces between transducer elements in arrays A, B and C used in this thesis are filled with corprene, Syntactic Foam, or paper with impedance around 413, 1500, and 1000 $kg/(m^2s)$, respectively. Compared to the impedance of ceramics, which is around 10^6 $kg/(m^2s)$, the impedances of the filling material are relatively small. Therefore, the cosine pattern shaping function applies to all the multi-element transducer arrays investigated in my research.

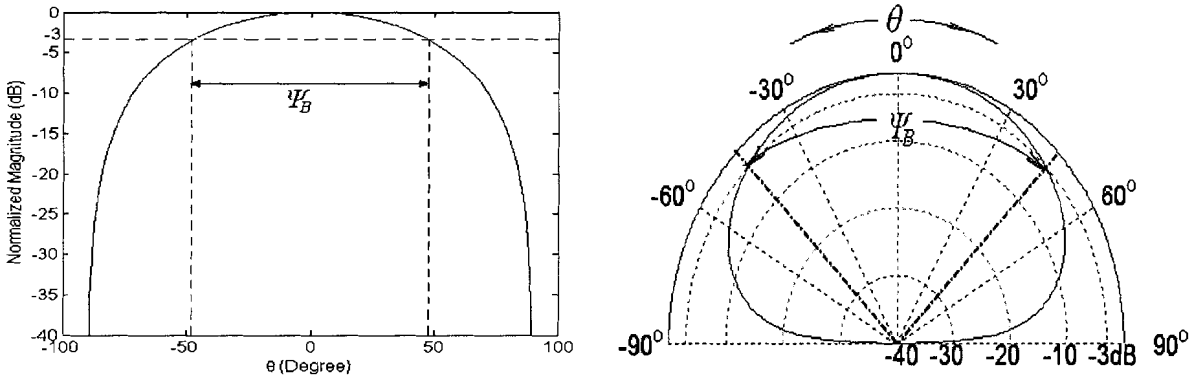

(a) (b)

Figure 2.4: Cosine pattern in a (a) Cartesian and (b) polar coordinate

2.2 Beam Pattern Measurement System

In the previous section, the ideal beam pattern for a transducer element is presented. In this section, the system used in the URL to obtain beam patterns, the Beam Pattern Measurement System, is described. To depict the system clearly, this section is divided into seven subsections: the first subsection outlines the setup and introduces the primary components of the BPMS; the second subsection briefly introduces what

is signal and what is noise in a measurement; the third subsection presents pictures of three transducer arrays which are investigated and compared throughout my thesis; the fourth subsection characterizes the amplifier used in the BPMS; the fifth subsection introduces important features of the A/D board; the sixth subsection illustrates the bandpass sampling method employed in this thesis; the last subsection describes the noise performance of the BPMS.

2.2.1 Outline of the Beam Pattern Measurement System

The BPMS in the URL is composed of a personal computer, a Field Programmable Gate Array (FPGA) manufactured by RPA Electronics Design [15], an A/D board manufactured by Interactive Circuits and System Ltd (ICS) [16], a transmitter, a receiver amplifier, a stepper motor, a projector and a hydrophone (array under test).

A picture of, and an illustrative side view of the water tank used to make beam pattern measurements are shown in Figure 2.5. The test tank dimensions are $4m \times 4m \times 2m$. The projector is mounted at the lower right hand corner of the test tank, while the hydrophone under test is mounted on a rotating pole at the opposite diagonal corner at the same depth as the projector. In the URL, the projector and hydrophone are set with their length dimension parallel to the rotation axis for measuring beam patterns in the plane perpendicular to the hydrophone array long dimension. A stepper motor rotates the hydrophone array under test in uniform increments. For typical beam pattern measurements, the hydrophone is stepped in the range of $[-90^o, 90^o]$, where $0°$ is oriented to directly align the acoustic axis of the hydrophone array under test with the acoustic axis of the projector.

A flow chart illustrating how the BPMS works is shown in Figure 2.6. The personal computer signals the A/D board to trigger the FPGA board. Meanwhile, the clock signal of the FPGA is constantly sent to the A/D board to synchronize the FPGA

(a)

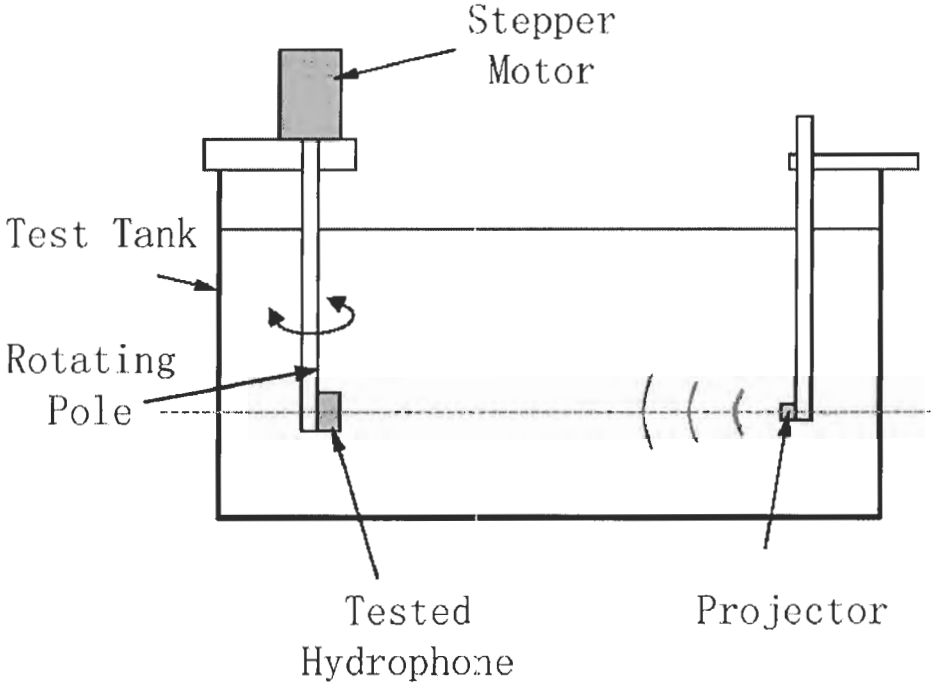

(b)

Figure 2.5: (a) Picture and (b) side view of the test tank (adapted from diagram by Robert Huxtable, 2005 by permission)

and A/D board. Once the FPGA is triggered, it produces pulses and sends them to the sonar transmitter, which in turn generates a square wave and applies it to the projector. The peak to peak output voltage of the transmitter can be adjusted between $0v$ and $600v$. In response to the voltage, the rectangular elements of the projector vibrate and produce acoustic waves that subsequently propagate through the water. When these acoustic waves arrive at the hydrophone, they compress and decompress the ceramic elements to produce a corresponding electrical signal. The amplifier with a computer controlled gain amplifies the signal that has been attenuated by the propagation loss through the tank. Afterwards, the amplified signal is sampled by the A/D board. Finally, the PC records the digitized received signal, directs the hydrophone array to rotate one step (usually 1^o), and begins the next cycle. A comprehensive description of the BPMS can be found in [17].

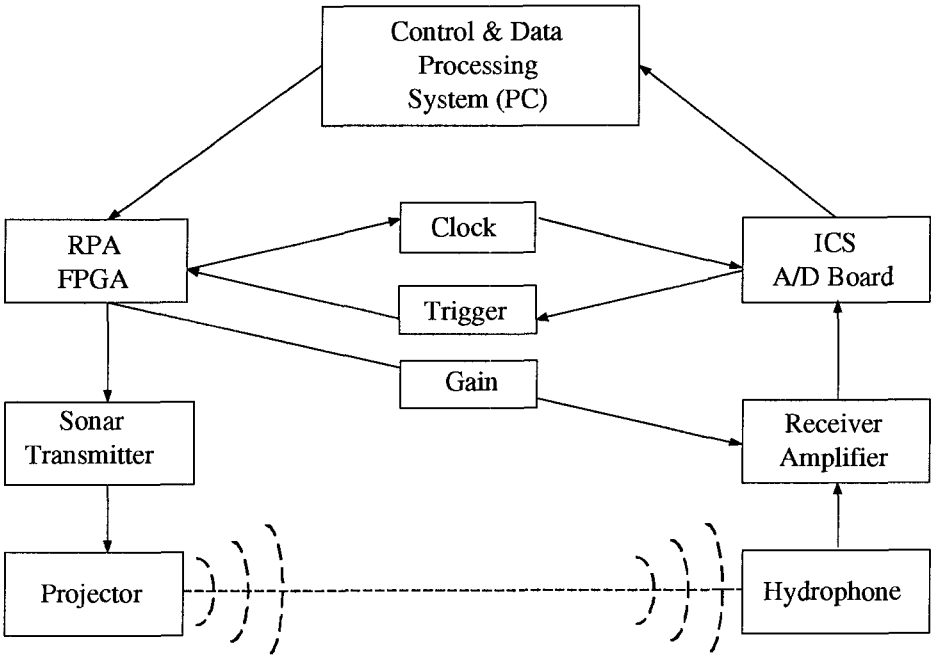

Figure 2.6: Configuration of the BPMS

2.2.2 Signal and Noise

In general, the word "signal" refers to useful information conveyed by some communications medium, while the word "noise" refers to anything else on that medium. Noise present in acoustic research can be classified into two categories: *ambient* and *electronic*. Ambient noise is the noise caused by the surrounding environment, and it enters the system through the transducer; electronic noise is the noise caused by the electronic components in the sonar system, including chips, resistors etc. The root-mean-square (RMS) level of noise $n(t)$ during time interval $[0, T]$s is defined as:

$$V_{Nrms}(V) = \sqrt{\frac{1}{T}\int_0^T |n(t)|^2 dt} \tag{2.2}$$

Generally, noise levels are compared using a decibel scale, hence,

$$\begin{aligned} V_{Nrms}(dB) &= 20\log_{10} V_{Nrms} \\ &= 10\log_{10}(\tfrac{1}{T}\textstyle\int_0^T |n(t)|^2 dt) \end{aligned} \tag{2.3}$$

The noise level of the BPMS is characterized later in this section.

In order to describe the quality of the measurement signal environment, the *signal-to-noise ratio*, or *SNR*, commonly expressed in decibels, is used to indicate the signal strength relative to background noise. If V_S and V_N represent the magnitudes of signal and noise respectively, SNR can be formulated as:

$$SNR = 20\log_{10}\frac{V_s}{V_N} \tag{2.4}$$

2.2.3 Transducers

Every transducer element has a specific resonant frequency determined by its dimensions, at which its oscillation amplitude in response to an electrical or acoustic stimulus is maximum. Around this resonant frequency, a transducer behaves like a

bandpass filter, removing higher order harmonics and passing only the fundamental component. Transducer arrays consisting of a number of elements with identical resonant frequencies are used in sonar systems because they are better than a single transducer element in regard to power radiation and directional discrimination. Figure 2.7 pictures three transducer arrays, denoted as arrays A, B and C, analyzed and compared throughout this thesis. Array A was built by the URL, array B was made by Simrad [18], and array C was made by Benthos [19]. All three arrays are prototype arrays to be used with the URL MASB sonar. The resonant frequencies of all these arrays are around 300 kHz.

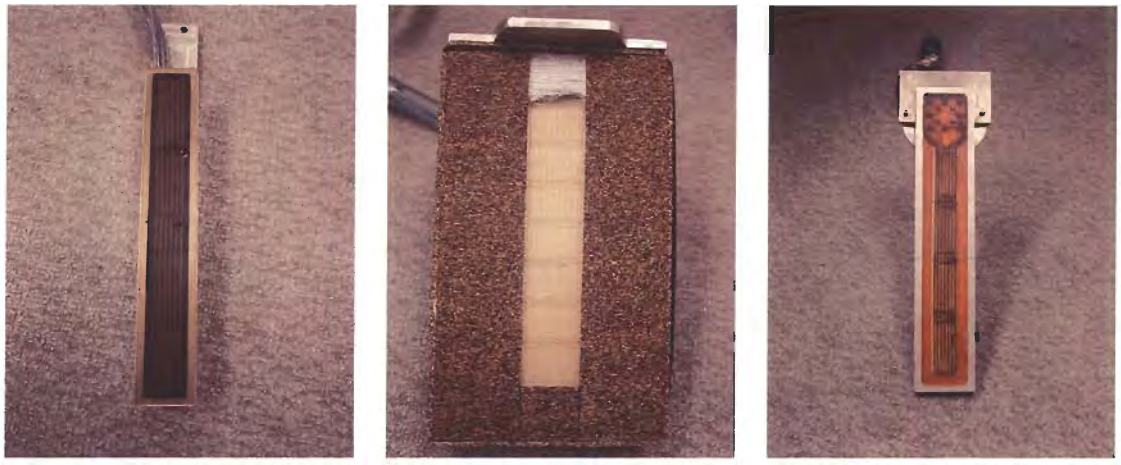

(a) (b) (c)

Figure 2.7: Arrays (a) A, (b) B and (c) C

A typical hydrophone signal as received by one of these arrays is depicted in Figure 2.8. A hydrophone signal takes time to stabilize at steady state, and the transient responses before and after the steady state are called the leading edge and trailing edge, respectively. It is evident from Figure 2.8 that during the transient response, the peak values of the hydrophone signal varies with time. Consequently, in the leading and trailing edges, the demodulated signals arriving at the same time at successive

transducer elements differ not only in phase, but also in magnitude. In order to guarantee that there are only phase delays among transducer elements, we locate the steady state, and only analyze the steady state signal while not considering the transient part of the signal.

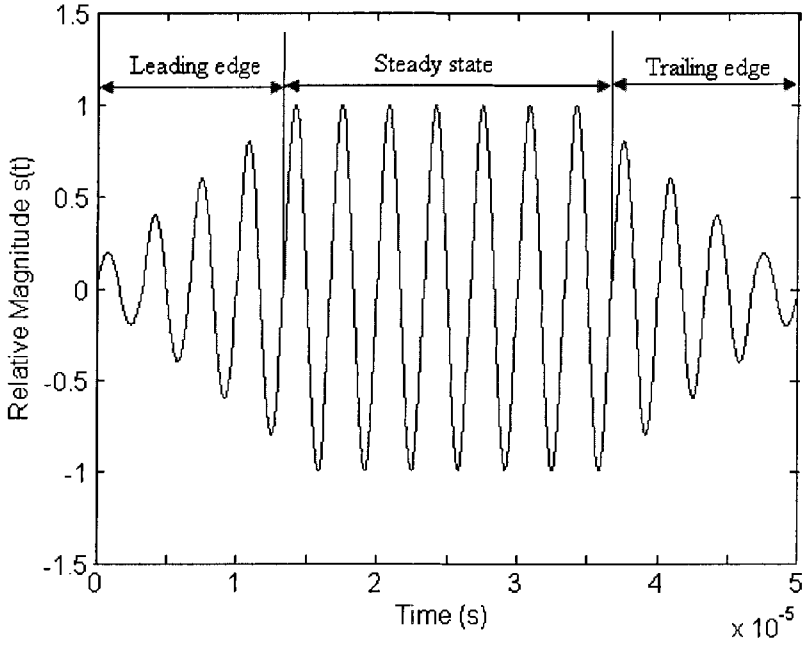

Figure 2.8: A hydrophone signal

2.2.4 Amplifiers

In the BPMS, an 8-channel amplifier is used to compensate for the energy lost during propagation before the hydrophone signal is digitized by the A/D board. A block diagram of a single amplifier channel is illustrated in Figure 2.9.

The multiple stage amplifier shown in Figure 2.9 offers a gain of 20 to 60 dB. The pre-amp is a unity gain amplifier. The gain of the second amplifier is controlled by a voltage from the FPGA, and its amplifying range is from 0 to 40 dB. The last stage provides 20 dB amplification. There are losses due to the passive roll-off filters

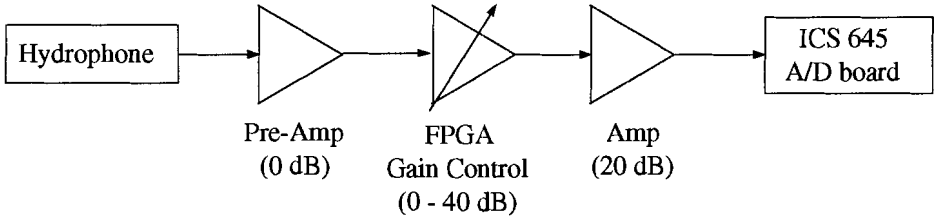

Figure 2.9: Block diagram of amplifier

in the circuit, resulting in an actual maximum amplifier gain of 19.6 dB to 53 dB. Also, the amplifier is driven by a ±5V DC supply, which limits the maximum output of the amplifier to be ±5V. Figure 2.10 describes the actual gain characteristics at a frequency of 300 kHz for channel 3 versus the gain command of FPGA in the range of 0 to 255.

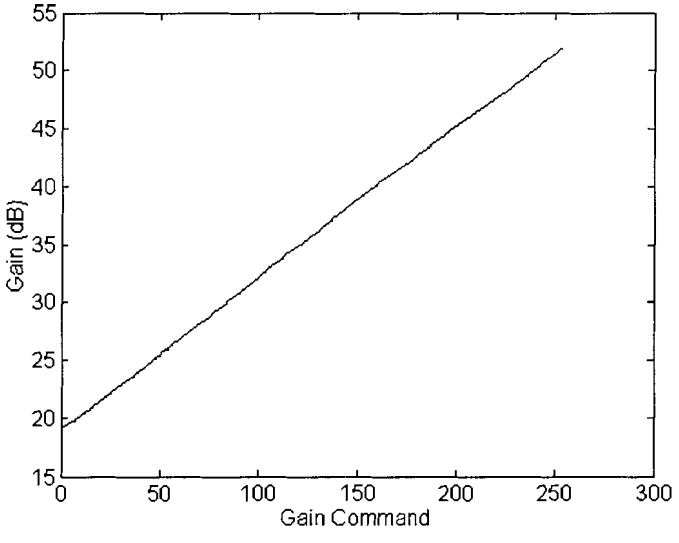

Figure 2.10: Gain vs gain command

Also, the amplifier acts as a wide bandpass filter. Figure 2.11 shows the magnitude and phase of the frequency response of channel 3 over the range of [40k, 700k] at a gain command of 0. As suggested by Figure 2.11, the gain of the amplifier achieves maximum value around 160 kHz.

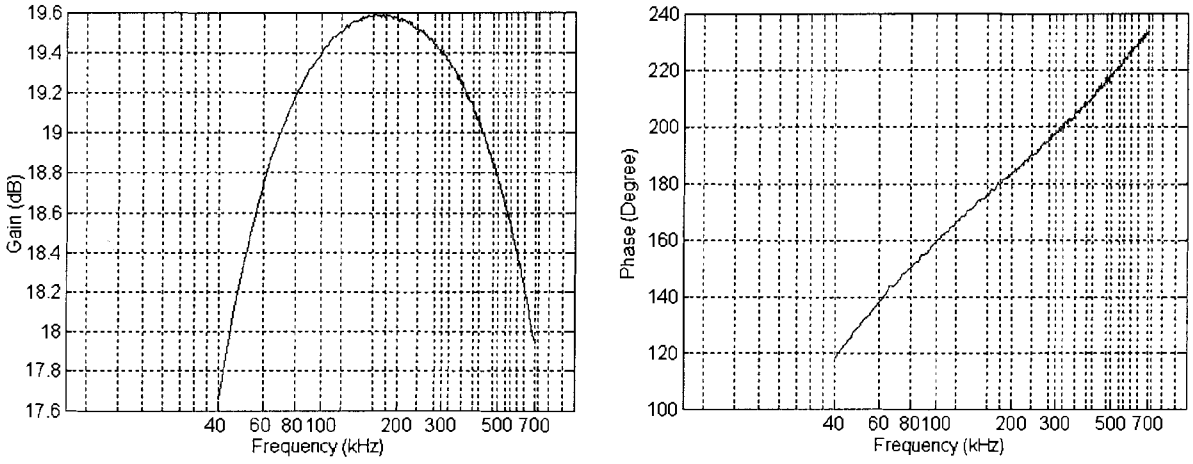

(a) (b)

Figure 2.11: (a) Gain and (b) phase of amplifier vs frequency

2.2.5 A/D Board

The ICS-645 is an 8-channel, 16 bit, high-speed A/D converter PCI board [20]. The ICS-645 offers external or internal clock and trigger options. In the BPMS, the A/D board is programmed to be internal triggered, and sends out a trigger signal to the FPGA; an external sampling clock is applied to the A/D board from the FPGA, which accomplishes synchronization between the A/D and FPGA boards.

The ICS-645 provides simultaneous sampling on all 8 channels, and therefore there is no phase error between channels. The highest sampling rate is 20MHz/channel. The oversampling ratio of the board can be programmed to be either 1, 2, 4, or 8. Consequently, the highest output data rate is either 20M, 10M, 5M or 2.5M Hz respectively. The oversampling rate we used in all beam pattern measurements is 8. The input scale of the A/D board is $[-1, +1]$ V giving $[-32768, +32767]$ (16-bit resolution). As a result, although the analog amplifier can produce an output in the range of $[-5, +5]$ V, the full input scale of the A/D board limits the maximum magnitude of the amplified signal to be less than 1 V. The dynamic range of the A/D

board is 89 dB in the decimation by 8 mode [20].

2.2.6 Bandpass Sampling

The bandpass sampling method employed in the BPMS to convert the bandpass signal to baseband is described as follows. More details about this method can be found in [21]. The continuous bandpass signal from the hydrophone can be represented as:

$$x(t) = Acos(\omega_c t + \alpha) \tag{2.5}$$

where A is the amplitude, $\omega_c = 2\pi f_c$ is the angular frequency and α is the phase angle. Equation (2.5) can be expanded into:

$$x(t) = A[cos(\omega_c t)cos(\alpha) - sin(\omega_c t)sin(\alpha)] \tag{2.6}$$

If we assume:

$$\begin{aligned} I(t) &= Acos(\alpha) \\ Q(t) &= Asin(\alpha) \end{aligned} \tag{2.7}$$

where $I(t)$ and $Q(t)$ are in-phase and quadrature components of the bandpass signal respectively. Then, Equation (2.6) becomes:

$$x(t) = I(t)cos(\omega_c t) - Q(t)sin(\omega_c t) \tag{2.8}$$

Conventional quadrature demodulation is implemented by multiplying the incoming signal with a replica of the carrier wave and filtering out harmonic terms. This basic scheme is outlined in Figure 2.12. Even though the conventional demodulation scheme is inexpensive and simple, the mismatch of amplitude and phase between the I and Q channels often limits system performance [22]. The method employed in the URL BPMS significantly improves the coherence between two parallel channels, and is described as follows.

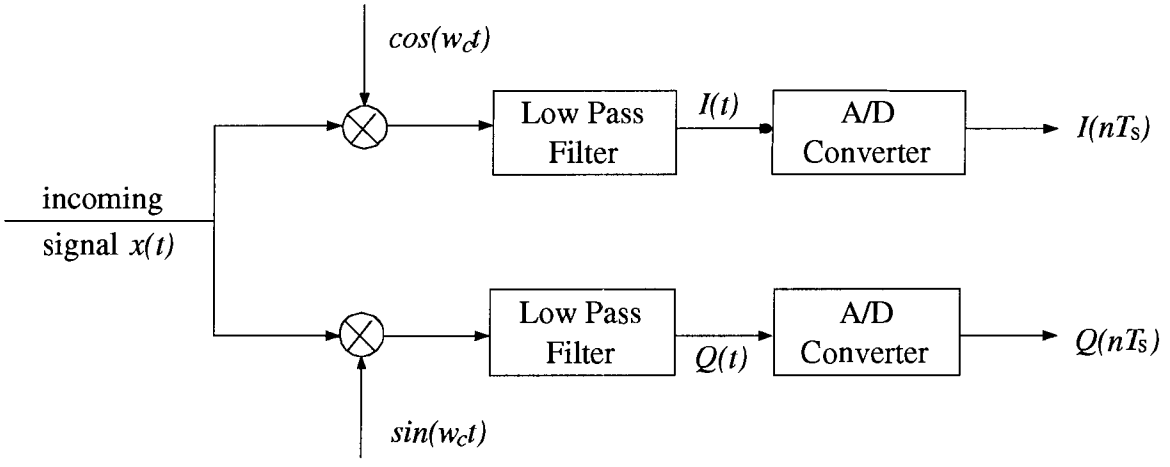

Figure 2.12: A conventional demodulator

It is evident from Equation (2.8) that $I(t)$ and $Q(t)$ are obtained from sampling the bandpass signal $x(t)$ at the moment of $sin(\omega_c t) = 0$, $cos(\omega_c t) = 1$ and $cos(\omega_c t) = 0$, $-sin(\omega_c t) = 1$, respectively. This process is illustrated in Figure 2.13. The thing to note is that $I(t)$ and $Q(t)$ samples are one quarter of a period apart in time, but the envelope of a narrowband signal does not change much in this time, and therefore the $I(t)$ and $Q(t)$ samples may be considered as being taken at the same time.

Considering $sin(\omega_c t)$ and $cos(\omega_c t)$ are out of phase by 1/4 period, if we sample the bandpass signal $x(t)$ $4N$ times the frequency of f_c, the first and the $N+1$ sampled data of every period are $I(t)$ and $Q(t)$. For example, if f_c is 300 kHz, the sampling frequency f_s can be 1.2 MHz, 2.4 MHz, $\cdots$. For $f_s = 1.2$ MHz, the $1st$ and $2nd$ of each cycle are $I(t)$ and $Q(t)$; but for $f_s = 2.4$ MHz, the $1st$ and $3rd$ of every period are $I(t)$ and $Q(t)$, and so on. Hence, by sampling, the received signals are converted into baseband signals $I(t)$ and $Q(t)$, for which the magnitudes and phases can be

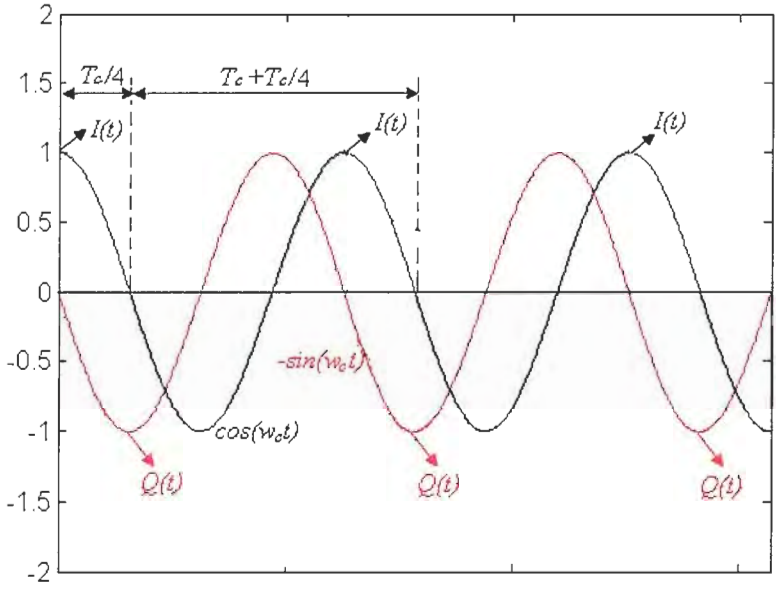

Figure 2.13: Illustration of sampling

expressed as:

$$\begin{aligned} A &= \sqrt{I(t)^2 + Q(t)^2} \\ \alpha &= \arctan \frac{Q(t)}{I(t)} \end{aligned} \tag{2.9}$$

2.2.7 Noise Description of the BPMS

The RMS noise of the BPMS versus the gain command from the FPGA ([0, 255]) is shown in Figure 2.14. The measurement of noise level is accomplished by applying different inputs to the amplifier. Shorting out the input and leaving the input open approximate the minimum and maximum noise level of the system. Also shown is the noise level measured with a typical hydrophone, array A, connected to the input of the amplifier. In addition, the noise level determined theoretically in the case of array A connected to the amplifier is plotted.

The noise plotted in Figure 2.14 approximately describes the noise of the AD

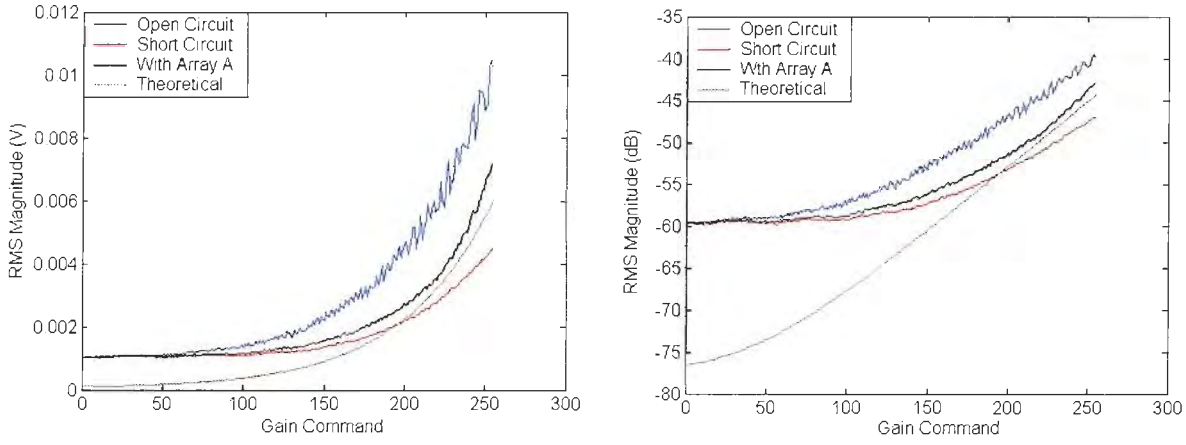

(a) (b)

Figure 2.14: (a) Absolute value and (b) decibel level of RMS noise in the BPMS

board plus the amplified noise of the multi-stage amplifier and hydrophone if there is one connected to the amplifier. While the noise of the AD board is independent of the gain of the amplifier, the noise of the amplifier and hydrophone is amplified, and therefore, depends on the gain of the amplifier. To aid in describing this dependence, the multi-state amplifier is shown schematically in Figure 2.15. The input noise N_0

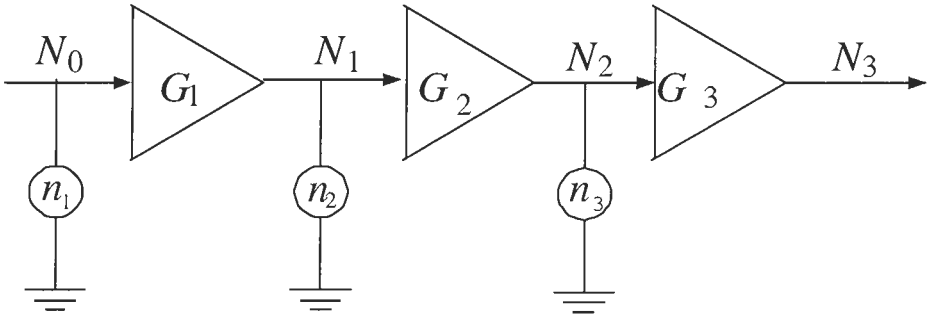

Figure 2.15: The multi-state amplifier

is from the hydrophone, which is amplified with gain of G_1, G_2, and G_3. The various noise components at each amplifying stage, n_1, n_2 and n_3, are added to N_0. Finally,

the noise N_3 at the output of the amplifier is [23]:

$$N_3 = G_1 G_2 G_3 N_0 \sqrt{1 + \frac{n_1^2}{N_0^2} + \frac{n_2^2}{G_1^2 N_0^2} + \frac{n_3^2}{G_1^2 G_2^2 N_0^2}} \tag{2.10}$$

As we mentioned earlier, $G_1 = 1$, and $G_3 = 10$, so Equation (2.10) becomes:

$$N_3 = 10 G_2 N_0 \sqrt{1 + \frac{n_1^2 + n_2^2}{N_0^2} + \frac{n_3^2}{G_2^2 N_0^2}} \tag{2.11}$$

The noise in the BPMS is N_3 plus the noise of the A/D board which is approximately -90 dB. Compared to the amplifier noise, whose smallest value is around -60 dB, the A/D noise can be neglected. The dependence of the noise of the BPMS on the FPGA controlled gain in the range of 0 to 255 is as plotted in Figure 2.14. It is noted that the measured noise level is much higher than the theoretical value at the lower gain (16 dB difference at the gain of 0). Meanwhile, since the measured and theoretical noise levels are close at the higher gain, we can tell from Equation (2.11) that some noise, the cause of which is unknown so far, is picked up during the third stage amplification. Nevertheless, as shown later, the signal-to-noise ratio is high enough so that the difference between the measured and theoretical noise level does not affect measurements at the lower gain. [1]

Since the noise level of the system is known, the maximum signal-to-noise level achievable can be calculated by subtracting the noise level from the max output level of the system, which is 1 V. Consequently, the signal-to-noise ratio of the system is obtained and plotted in Figure 2.16. The thing to note is that this SNR is the raw SNR before any further processing, such as filtering and averaging the steady state of incident signals, which are explained in the later section.

[1]Note that the amplifiers were those that were available for beam pattern measurements at the time. These amplifiers need to be redesigned for better noise performance at low gain.

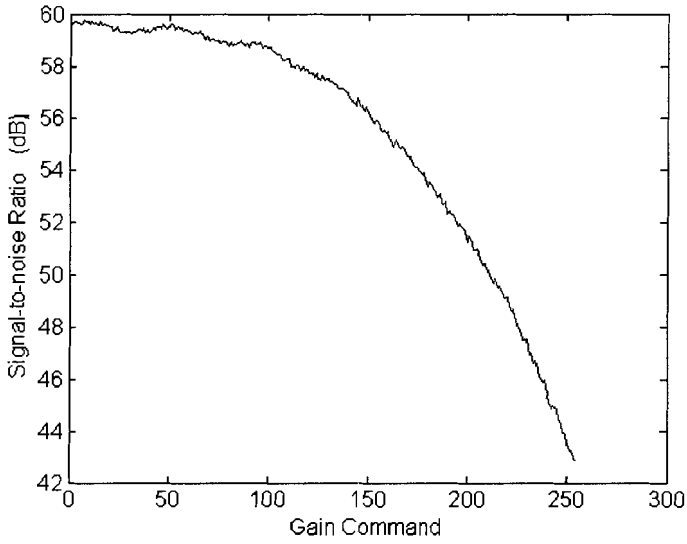

Figure 2.16: Signal-to-noise ratio of the BPMS

As suggested in Figure 2.16, a higher SNR, which indicates better performance of the BPMS in producing more accurate beam pattern measurements and angle-of-arrival estimations, is achieved at the lower gain. In practice, the difference between the effects for an SNR of 43 dB at the gain of 255 and 60 dB at the gain of 0 is not very significant for typical beam pattern measurements and angle-of-arrival estimations.

2.3 GUIs of the BPMS

We outlined the BPMS and its noise performance in the previous section. In this section, we focus on two routines: one is designed for making beam pattern measurements, and the other one is for displaying beam patterns.

2.3.1 GUI for Beam Pattern Measurements

The BPMS is controlled from MATLAB. The MATLAB Graphical User Interface (GUI) shown in Figure 2.17 was built to simplify the use of the BPMS. All beam

pattern measurements are performed through this GUI. To help explain, the GUI is divided into three parts as labeled in Figure 2.17, each of which will be described in detail in the following discussion. The parameters necessary for measurements can be edited in Part I. The default parameters usually used in our beam pattern measurements are listed and briefly described in Table 2.1.

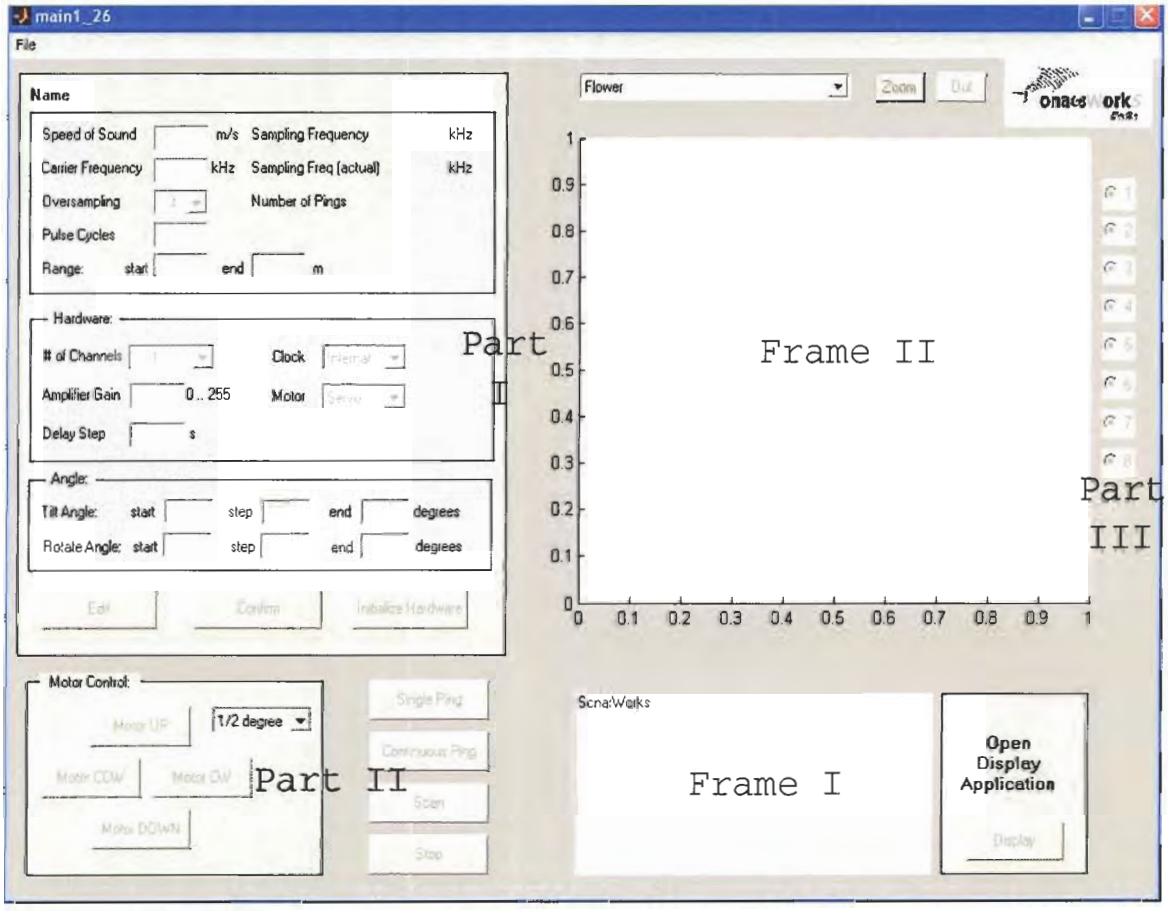

Figure 2.17: The GUI for beam pattern measurements

In part II, users can control the hydrophone to align it directly with the projector, and also, can start or stop a measurement. This alignment is accomplished by rotating the stepper motor in a clockwise or counterclockwise direction. All beam pattern

Table 2.1: Beam pattern measurement parameter defaults

Parameter	Description	Value
Sound Speed	Speed of sound in water(m/s)	1482
Carrier Frequency	Frequency at which the projector and hydrophone will operate	300 kHz
OverSampling	Number of samples per cycle (≥ 4)	8
Pulse Cycles	Number of cycles that will be transmitted one ping	100
Range	Range from which samples will be taken (m)	3.5
	Range at which taking samples will be ended (m)	5
Number of Channels	Number of elements in the hydrophone	6
Amplifier Gain	Gain of the amplifier [0, 255]	0
Delay Step	Angular size between each step of the stepper motor	1
Clock	Clock signal of the A/D board (Internal/External)	External
Rotate Angle	Angle from which the hydrophone will start rotating	-90^o
	Angle at which the hydrophone will stop rotating	90^o

measurements are initiated by activating "scan", and can be interrupted at any time by "stop".

Part III is divided into two frames to display the status of the current process and collected data. As a command is being executed, its information is displayed in Frame I; and after the operation is finished, the collected data is displayed in Frame II. The channel to be displayed can be selected from the radio button on the right of the Frame II. The method for displaying data can be set from the popup menu above

Frame II. All the methods are listed and described as follows.

- Flower plot

  The flower plot is used to align the hydrophone with the projector before a beam pattern measurement starts. If the hydrophone and the projector fall into line, there will be no phase difference across the hydrophone face. Therefore, the received signal of each hydrophone element supposedly differs from the others the least. Hence, if we assume the x axis and y axis represent the in-phase and quadrature component of the bandpass signal respectively, the plots of all channels will have the greatest overlap when the projector and the hydrophone are aligned. Figure 2.18 is plotted for further illustration.

  Figure 2.18(a) represents the case when the angle between the projector and array A is -50^o; (b) represents the best case we can obtain from aligning array A with the projector; (c) represents the case when the angle between the projector and array A is 50^o. In these plots, the points around $[0, 0]$ represent the initial state without the signal arriving, and the deviation around $[0, 0]$ is caused by noise; the points with the maximum distance from $[0, 0]$ represent the data collected from the steady state; the lines between $[0, 0]$ and the most distant points represent transient responses. In this way, the flower plot helps us align the hydrophone with the projector during beam pattern measurements.

- Oscilloscope plot

  The oscilloscope plot represents the signal collected from the hydrophone in the way an oscilloscope does. In such a plot, the x axis represents the distance between the hydrophone and the projector, and the y axis represents the amplitude of the bandpass signal. Figure 2.19 reproduces the third channel shown in Figure 2.18(b) in an oscilloscope plot.

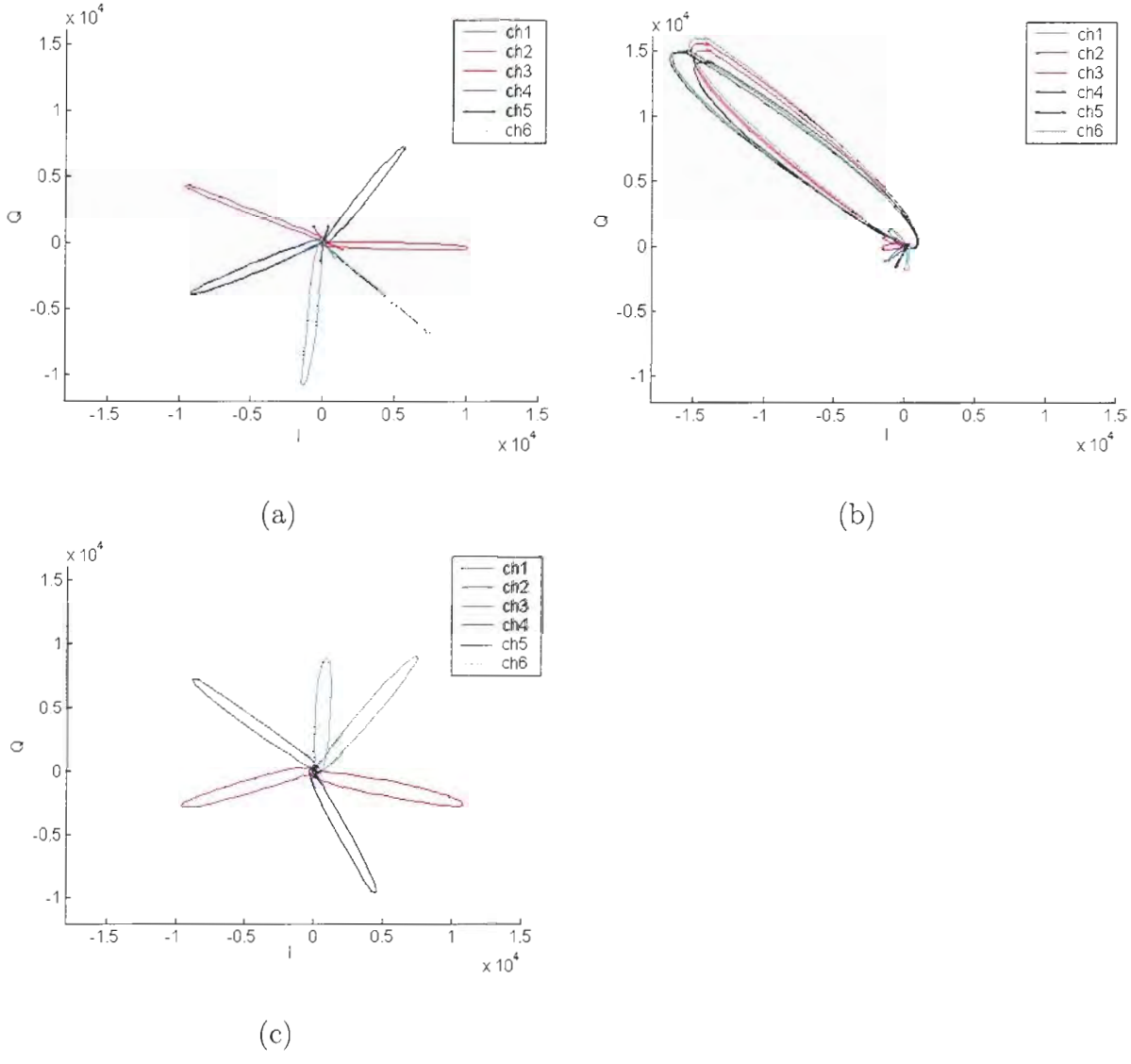

(a) (b)

(c)

Figure 2.18: Flower plot at (a) $\theta = -50^o$, (b) $\theta = 0^o$, and (c) $\theta = 50^o$,

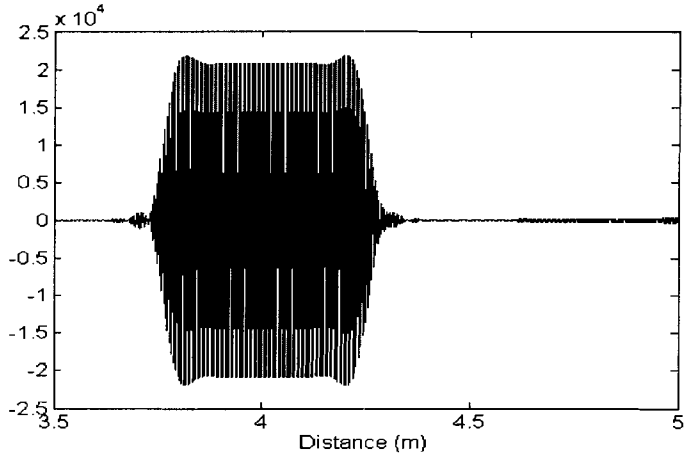

Figure 2.19: Oscilloscope plot

- Envelope plot

  The envelope plot represents the complex baseband signal down converted from the received signal. In this display, the in-phase and quadrature components of the bandpass signal are plotted as a function of range. The envelope plot in Figure 2.20 illustrates the baseband signal converted from the bandpass signal shown in Figure 2.19.

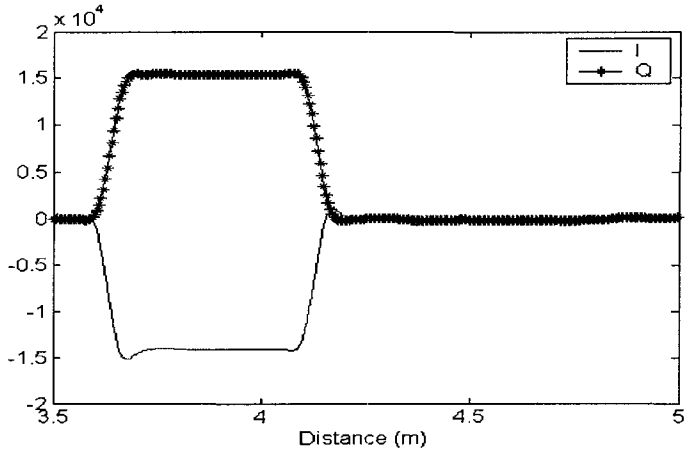

Figure 2.20: Envelope plot

In Figure 2.20, the plain line represents the in-phase component, and the line plotted in "*" represents the quadrature component. It is evident that the signal contains leading edge and trailing edge transients before and after the steady state. In order to ensure that the signal is constant across all the hydrophone elements at each ping, the location of the steady state response is estimated in the display program.

2.3.2 GUI for Beam Pattern Display

After a beam pattern measurement is accomplished, another GUI, designed to display the beam patterns (shown in Figure 2.21), is called by clicking on the display button of "Open Display Application" in the GUI shown in Figure 2.17.

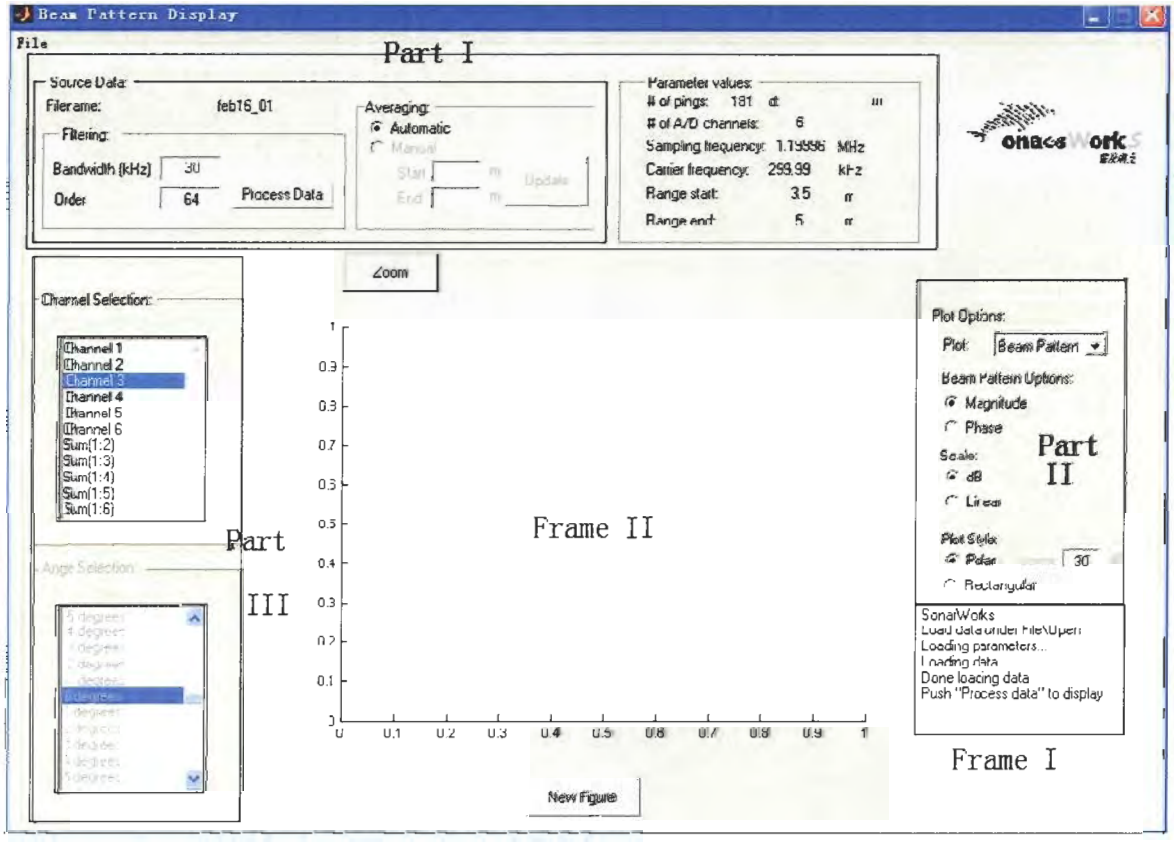

Figure 2.21: The GUI for beam pattern display

The GUI shown in Figure 2.21 is separated into three parts and two frames for further explanation. Part I displays the parameters that were described in the previous subsection. Also, in Part I, users can edit variables that will be applied when processing data.

- The bandwidth and order in the filtering frame specify the filter that will be applied to the data collected from the beam pattern measurement. The filter allows the signal as well as noise in the signal band to pass, and removes the noise outside this band. The default values of the bandwidth and filter order are 30 kHz and 64, respectively.

- The averaging option is for determining the method to locate the steady state signal for averaging. This can be achieved either automatically or manually. Automatic averaging locates the steady state signal by finding the steepest point on the leading and trailing edges of the signal, and averages over 1/4 to 3/4 of the range between these two points. Manual averaging requires users to specify the start and end averaging range.

After all these parameters are set up, clicking the button "Process Data" activates a series operations that are applied to the data. Each step being performed is shown in Frame I, and the beam pattern will be displayed in Frame II.

In part II, users can select display methods from five options: flower plot, envelope plot, beam pattern, aperture function, and relative angle. While both the flower plot and envelope plot give a graphical image of the data collected at a certain angle as shown in Figures 2.18 and 2.20, the others represent the data collected over the whole scanned angular range. A detailed discussion of beam patterns, aperture functions, and relative angles is presented in the next chapter.

In part III, users can select the data to be displayed. In the case of a flower plot or envelope plot, users can also choose the angle at which the data is to be displayed.

In summary, the GUIs demonstrated in this section are utilized to make beam pattern measurements and to display beam patterns, and their use significantly simplifies the control of the BPMS.

Chapter 3

Element Spacing of Transducer Arrays

In linear acoustic arrays, it is important that the spacing between line elements be of a certain size. Furthermore, since it is not physically feasible to measure the inter-element spacing after elements are put into an array, it is desirable to estimate the inter-element spacing in an electrical way. By the inter-element spacing, we mean the center-to-center distance between two adjacent elements. In this chapter, we first discuss the selection of inter-element spacing for such arrays; then, we propose a method to obtain the aperture function that is further utilized to estimate inter-element spacing; finally, we present experimental results for transducer arrays to verify the viability of the method.

3.1 Inter-element Spacing

This section outlines the inter-element spacing requirement of a transducer array used in an MASB sonar system. The requirement of the inter-element spacing mainly focuses around the range of phase differences between transducer elements for signals coming from different angles.

As mentioned in Chapter 1, for multi-element transducer arrays with inter-element

spacing of d, the phase difference between two elements in response to a signal at physical angle θ is:

$$\phi = \frac{2\pi d sin\theta}{\lambda} \tag{3.1}$$

In Equation (3.1), θ is the angle between the plane perpendicular to array axis and the direction of signal, as shown in Figure 1.1. Hence, the range of θ is $[-\pi/2, \pi/2]$. Since the phase range is $[-\pi, \pi]$, the phase difference ϕ beyond $\pm\pi$ will be wrapped into $[-\pi, \pi]$. The inability to determine $2k\pi$ (k is an integer) differences in phase results in a *phase ambiguity.*

According to the relationship between d/λ and ϕ presented in Equation (3.1), all possible situations can be divided into three cases. (1) If the array elements are placed less than half a wavelength apart, i.e., $d/\lambda < 1/2$, ϕ is confined to a region smaller than $\pm\pi$ when θ varies from $-\pi/2$ to $\pi/2$. (2) If $d/\lambda = 1/2$, then ϕ is in the range of $[-\pi, \pi]$. In both cases (1) and (2), only one θ can be specified from a given ϕ. (3) If $d/\lambda > 1/2$, then ϕ will reach beyond the range of $\pm\pi$, and it is no longer possible to uniquely determine θ from a given ϕ. These three cases are plotted in Figure 3.1.

In Figure 3.1, the curve in "$\lhd$" describes the case for $d = \lambda/4$; the one in "." describes the case for $d = \lambda/2$; the one in "$\times$" describes the case for $d = \lambda$, in which the sections beyond $\pm\pi$ can not be distinguished causing ambiguity. This case after wrapping into the range of [-π, π] is represented by the plain line in Figure 3.1.

Consequently, the transducer array with inter-element spacing $d \leq \lambda/2$ is considered to be suitable for target angle estimation in an MASB sonar system since there is no ambiguity. However, in the case of $d < \lambda/2$, the differentiable phase range is smaller than that in the case of $d = \lambda/2$. Also, the difficulty faced in manufacturing transducer arrays of small inter-element spacing should be considered in the design. Therefore, the optimal inter-element spacing for a transducer array used in

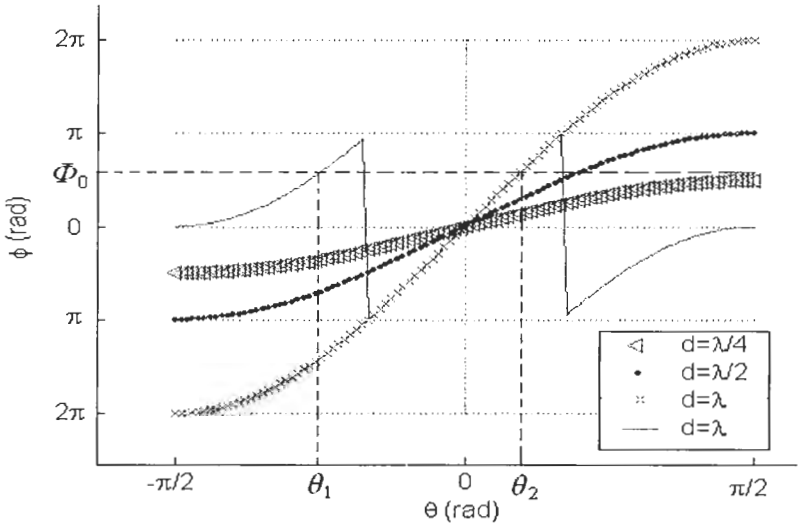

Figure 3.1: Design of different inter-element spacings

an MASB sonar system is typically $\lambda/2$. For example, if the resonant frequencies of transducer elements are 300 kHz and the sound speed is 1500 m/s in water, the optimal center-to-center distance between two adjacent array elements is 2.5×10^{-3} m.

3.2 Aperture Function and Pattern Function

The *aperture function* represents the hydrophone response or excitation along its length. The *pattern function* is the Fourier Transform of the aperture function. The aperture function can be used to measure the approximate level of acoustic or electric interference between transducer elements, and also, to assess element-to-element uniformity and quality of the separation between transducer elements [24]. The pattern function is usually utilized to represent the angular response characteristics of a transducer. In this thesis, the aperture function, which is obtained from the pattern function through the inverse Fourier Transform, is utilized to estimate the effective

inter-element spacing of multi-element transducer arrays.

This section is divided into five subsections to describe the process of obtaining aperture functions from beam patterns. The first subsection defines the aperture function and pattern function, and explains the relationship between the aperture and pattern function, and also the relationship between pattern function and beam pattern; the second subsection demonstrates the feasibility of estimating the inter-element spacing by applying the inverse Fourier Transform to the pattern function; the third subsection presents the procedure that translates the measured beam pattern into its correspondent pattern function, from which the aperture function is obtained; the fourth subsection compares the magnitude and phase of beam patterns of three transducer arrays; the last subsection presents aperture functions for arrays A, B and C obtained from their beam patterns.

3.2.1 Aperture, Pattern Function and Beam Pattern

The aperture function and pattern function, generally represented by $g(x)$ and $G(u)$, both describe the hydrophone response. The relationship between them is analogous to that between a time domain function and its corresponding frequency domain representation [8]. The aperture function can be obtained from the pattern function through the inverse Fourier Transform (IFT), and the pattern function can be obtained from the aperture function through the Fourier Transform (FT). This relationship can be formulated by:

$$\begin{aligned} G(u) &= \int_{-\infty}^{+\infty} g(x) e^{-j2\pi xu} dx \\ g(x) &= \int_{-\infty}^{+\infty} G(u) e^{j2\pi xu} du \end{aligned} \tag{3.2}$$

In Equation (3.2), x is the physical width of the transducer array, and the variable u is:

$$u = \frac{sin\theta}{\lambda} \tag{3.3}$$

where θ is the physical angle, and λ is the wavelength.

While the beam pattern $B(\theta)$ describes the hydrophone response as a function of angle θ, the pattern function $G(u)$ describes the hydrophone response as a function of the variable u. Notice that the variable u is confined to $\pm 1/\lambda$ as θ varies over the range $[-\pi/2, \pi/2]$. This results in a *visible region* $[-1/\lambda, 1/\lambda]$ for the pattern function $G(u)$. For example, if the resonant frequency of a transducer array is 300 kHz and the sound speed is 1500 m/s, the visible region of $G(u)$ is $[-200, 200]$ 1/m, as shown in Figure 3.2.

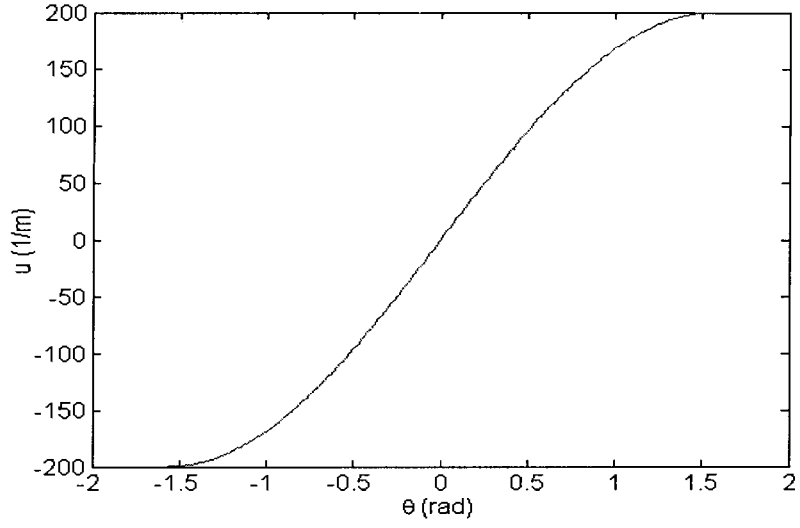

Figure 3.2: The relationship between θ and u

In the following paragraphs, we present the approach used for obtaining the aperture function from the visible region of the pattern function. As discussed in Chapter 2, the Beam Pattern Measurement System in the Underwater Research Lab enables us

to obtain the hydrophone response as a function of physical angle θ. With Equation (3.3), we can convert it into the hydrophone response versus u, i.e., $G(u)$. Applying the IFT to $G(u)$, the aperture function is determined (with limitations discussed in the next subsection) and used to estimate the inter-element spacing of transducer arrays.

3.2.2 The Aperture Function and the Visible Region of the Pattern Function

In the previous subsection, the concepts of the aperture function and pattern function, and also the relationship between them were discussed. In this subsection, we demonstrate that it is feasible with some limitations to obtain the aperture function by applying the IFT to the visible region of the pattern function $G(u)$.

The aperture function of a single rectangular element with a length of $L = 2 \times 10^{-3}$ m is plotted in Figure 3.3, where the x axis is the physical length, and the y axis represents the hydrophone response. The magnitude and phase of its pattern function obtained by applying the FT to this aperture function are illustrated in Figure 3.4(a) and (b), respectively. From a mathematical viewpoint, the visible region can be produced by multiplying an ideal rectangular window function with the length of $2/\lambda$ ($\lambda = 5 \times 10^{-3}$ m) as shown in Figure 3.5, by the central part of the pattern function, with the result as shown in Figure 3.6. The aperture function obtained by applying the IFT to the visible region of the pattern function shown in Figure 3.6 is reproduced in Figure 3.7 on a linear and decibel scale.

Compared to the original aperture function shown in Figure 3.3, the one in Figure 3.7 is distorted. This can be explained by the multiplication between $G(u)$ and the rectangular window in the u domain, which corresponds to a convolution between the original $g(x)$ and a sinc function in the x domain.

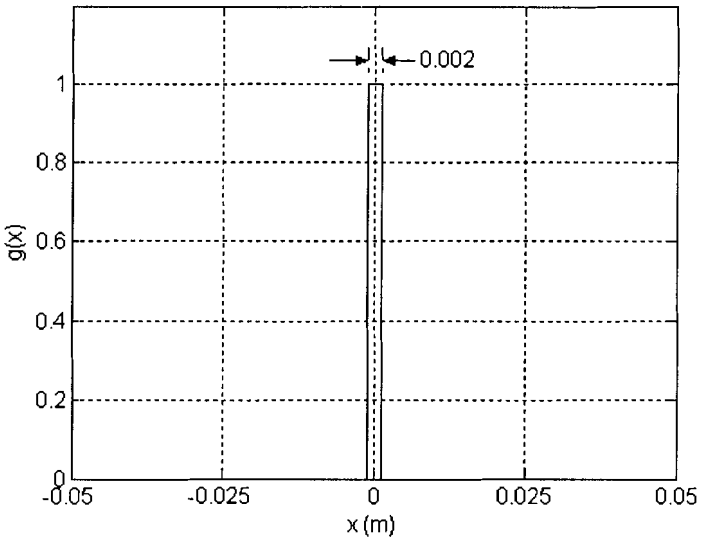

Figure 3.3: The aperture function

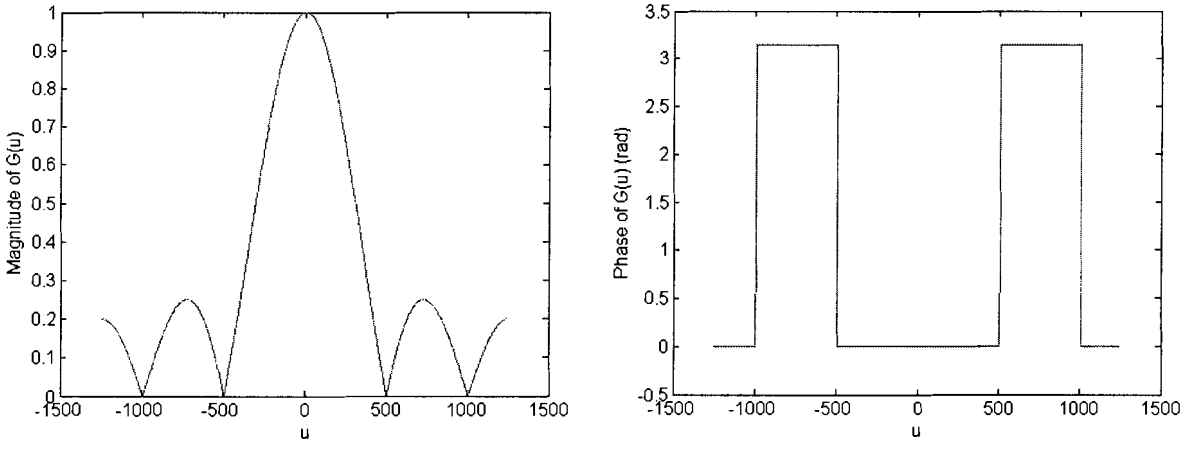

(a) (b)

Figure 3.4: The (a) magnitude and (b) phase of the pattern function

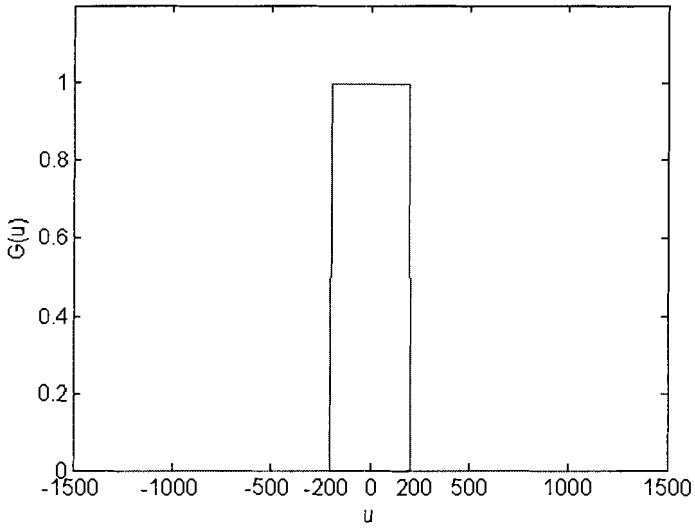

Figure 3.5: The rectangular window with a length of $2/\lambda$

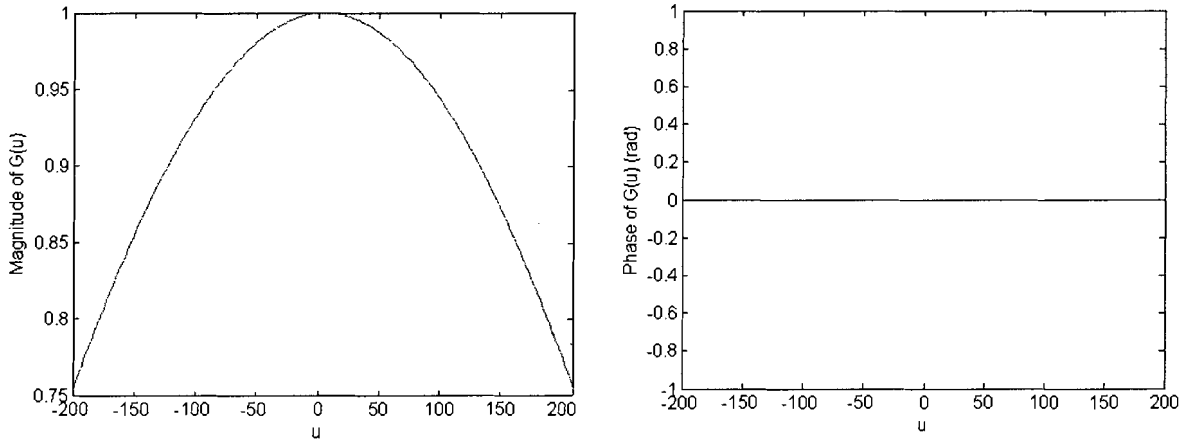

Figure 3.6: The visible region of the pattern function

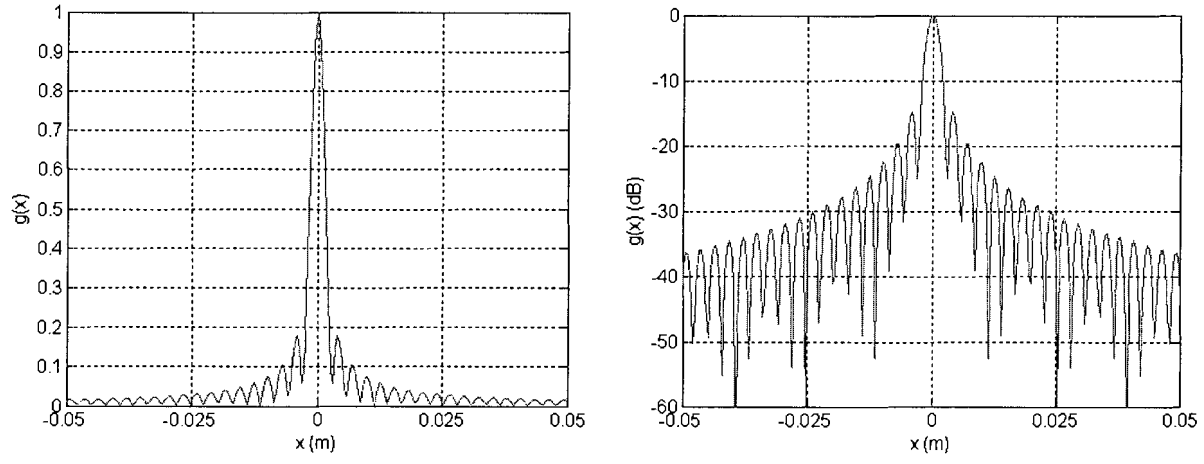

(a) (b)

Figure 3.7: The converted aperture function on a (a) linear and (b) decibel scale

If the transducer element is shifted x_0 m along the x axis to $[-L/2+x_0,\ L/2+x_0]$, its aperture function and pattern function as given by Equation (3.4) are plotted in Figures 3.8 and 3.9, respectively, where $x_0 = 4 \times 10^{-3}$ m, and $L = 2 \times 10^{-3}$ m.

$$g(x - x_0) \longleftrightarrow e^{-j2\pi u x_0} G(u) \tag{3.4}$$

It is evident that the magnitude of the pattern function in Figure 3.9 is identical with the magnitude shown in Figure 3.4, while the phase differs. This is the same result as we expected from Equation 3.4. The visible region of the pattern function is plotted in Figure 3.10.

Theoretically, applying the IFT to the pattern function shown in Figure 3.9 should obtain the shifted aperture function, while applying the IFT to the visible region of $G(u)$ shown in Figure 3.10 results in a distorted aperture function with the result as shown in Figure 3.11. Compared to the original shifted aperture function shown in Figure 3.8, although the appearance of g(x) in Figure 3.11 is distorted, its central

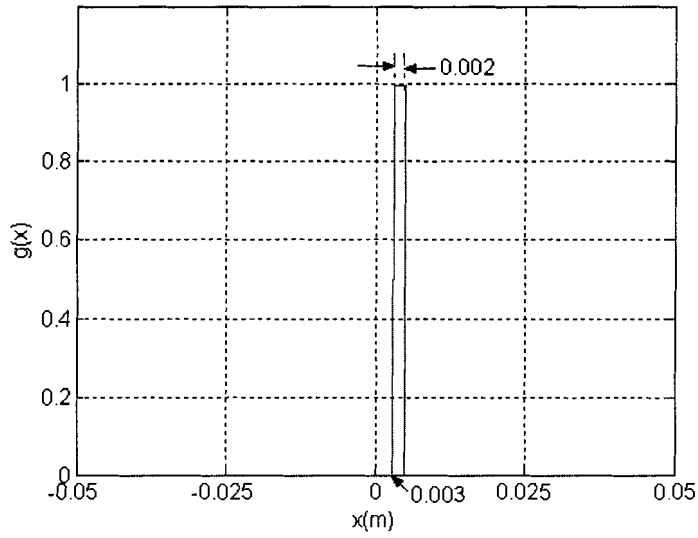

Figure 3.8: The shifted aperture function

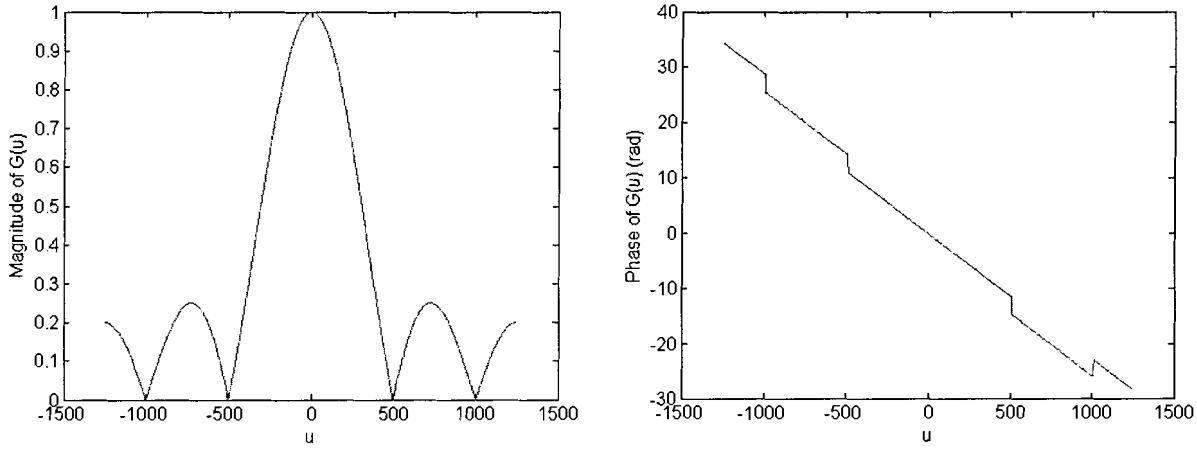

(a) (b)

Figure 3.9: The (a) magnitude and (b) phase of the pattern function

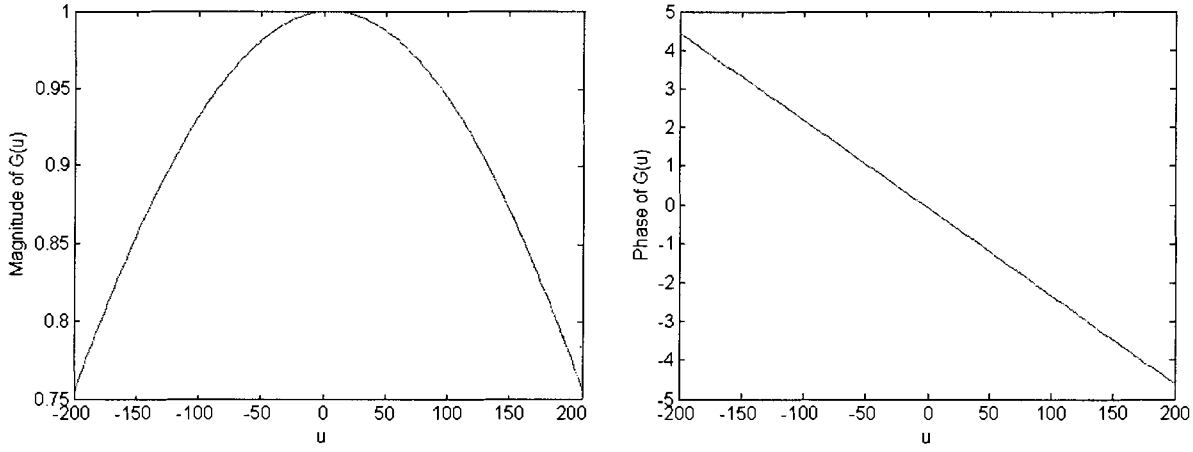

Figure 3.10: The visible region of the pattern function

position remains identical with the original shifted g(x) at 4×10^{-3} m. This makes it possible to estimate the position of the original aperture functions by applying the IFT to the visible region of the pattern function.

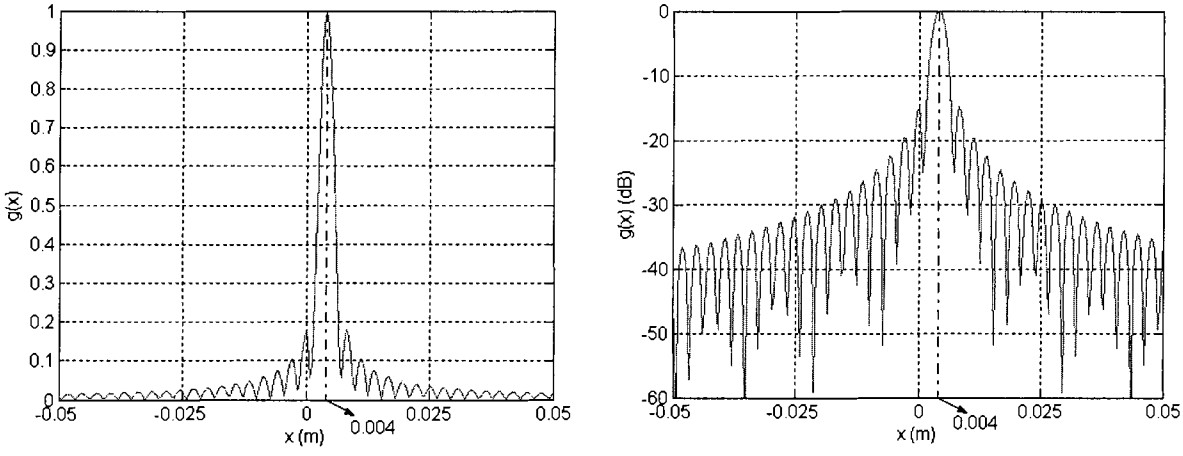

(a) (b)

Figure 3.11: The converted aperture function on a (a) linear and (b) decibel scale

For six elements uniformly placed along the x axis as shown in Figure 3.12(a), the aperture functions converted from the visible regions of pattern functions are

plotted together in Figure 3.12(b). By comparing (b) with (a), we can tell that the six curves represent six rectangular elements composing the transducer array. The distance between adjacent curves in Figure 3.12(b) is 4×10^{-3} m, which is exactly the distance between centers of adjacent elements of the original aperture function in (a). Therefore, it is viable to estimate the inter-element spacing by applying the IFT to the visible region of the pattern function. The next subsection describes the essential step for determining pattern functions from beam patterns obtained with the BPMS.

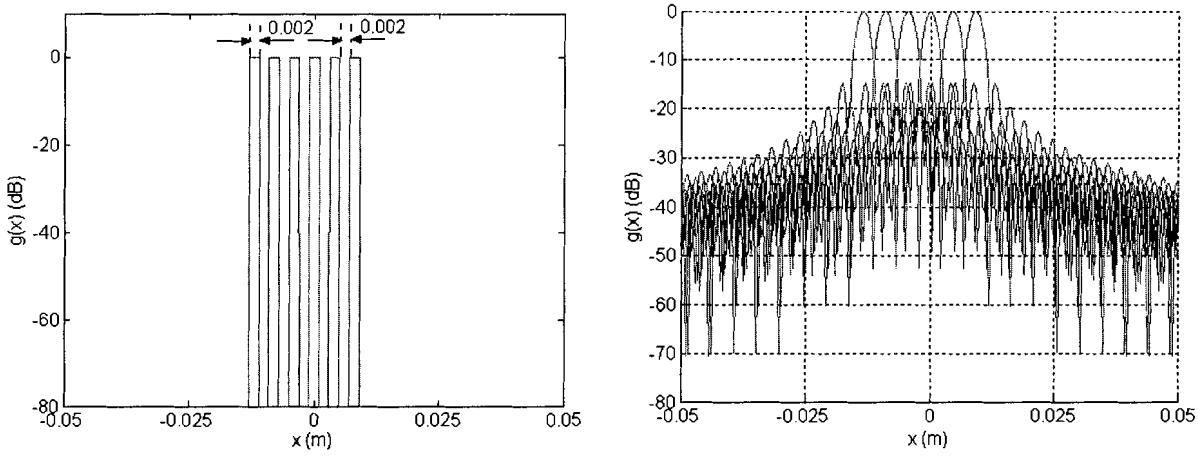

(a) (b)

Figure 3.12: The (a) original and (b) converted aperture function

3.2.3 Interpolation between the Beam Pattern and Pattern Function

In this subsection, we point out the necessity of converting the beam pattern into the pattern function, and also, a method to implement this conversion.

As we mentioned earlier, the beam pattern $B(\theta)$ can be measured with the BPMS and represents the level of transducer response at a certain physical angle θ; the pattern function $G(u)$ represents the transducer response versus the variable u. Due

to the nonlinear relationship between θ and u described in Equation (3.3), a uniformly distributed sequence of θ will produce a nonuniformly distributed sequence of u. This indicates that when the observed points of $B(\theta)$ distribute uniformly, those of $G(u)$ distribute nonuniformly, as shown in Figure 3.13.

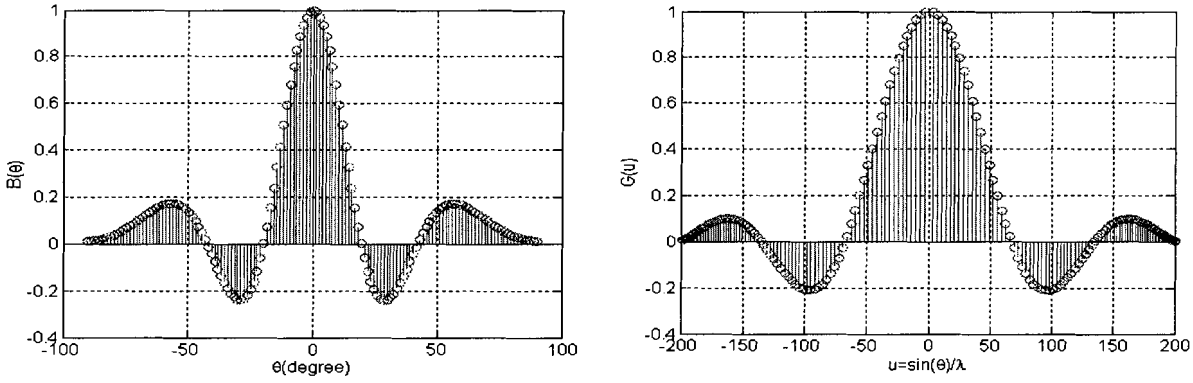

(a) (b)

Figure 3.13: (a) Beam pattern versus uniform θ and (b) pattern function versus nonuniform u

Since we will apply the inverse Fourier Transform to $G(u)$ not $B(\theta)$ to determine the aperture function, it is necessary to translate the unevenly distributed observation points of $G(u)$ into evenly distributed ones. This is done through *interpolation*. Several methods of interpolation can be found in MATLAB, such as linear interpolation, nearest neighbor interpolation, and spline interpolation. Linear interpolation is used in this thesis to convert the nonuniform observation points of $G(u)$ to the uniform ones, with the result shown in Figure 3.14.

Future discussions in this thesis will couple measured beam patterns with aperture functions and it will be understood that there is this intermediate step of interpolation to obtain the pattern function from which the aperture function is obtained. This coupling aids the discussion and reduces the number of figures.

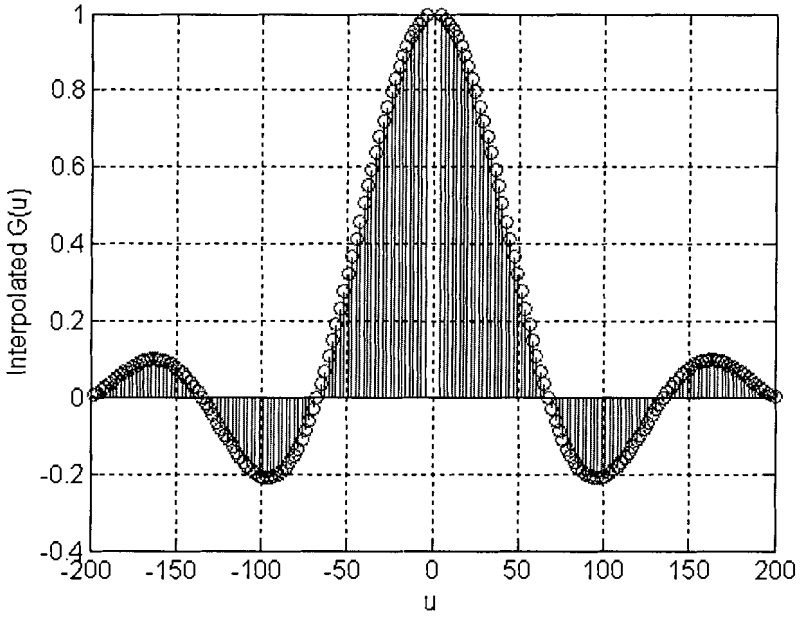

Figure 3.14: Beam patters versus uniform u after interpolation

3.2.4 Magnitude and Phase of Beam Patterns

This subsection presents and compares experimental beam patterns of arrays A, B and C, from which their aperture functions are obtained. As discussed in Chapter 2, complex-baseband signals are obtained by applying the time-domain demodulation method to data collected from a transducer array. For an N-element transducer array, N sets of complex data are collected at each angle, and consequently, N beam patterns are produced while the hydrophone rotates through the range $[-\pi/2, \pi/2]$. The magnitudes of beam patterns for arrays A, B and C are plotted in Cartesian and polar coordinates in Figures 3.15 - 3.17, where each beam pattern is normalized with respect to its maximum value and plotted on a decibel scale. Also shown is the expected beam pattern, which is an ideal cosine function.

It is evident from Figure 3.15 that apart from small variations, the beam pattern amplitudes of the six elements in array A are quite uniform. Compared with the beam

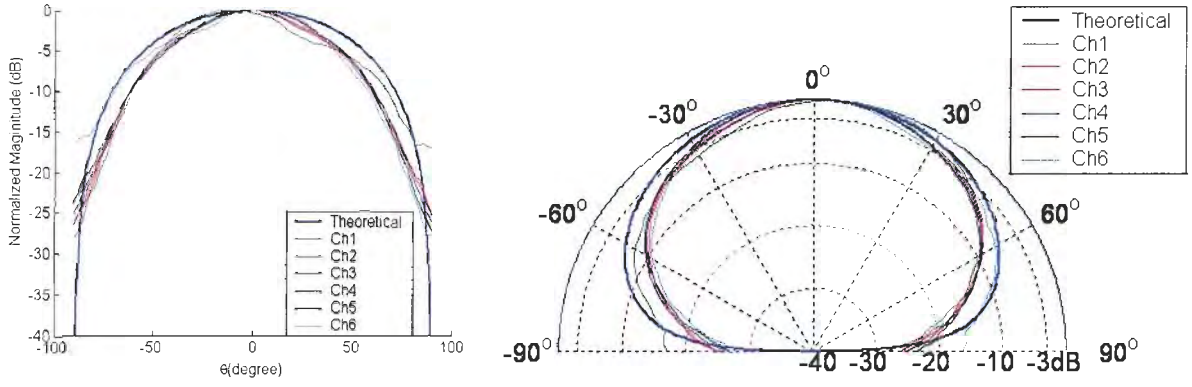

Figure 3.15: Magnitudes of beam patterns for array A

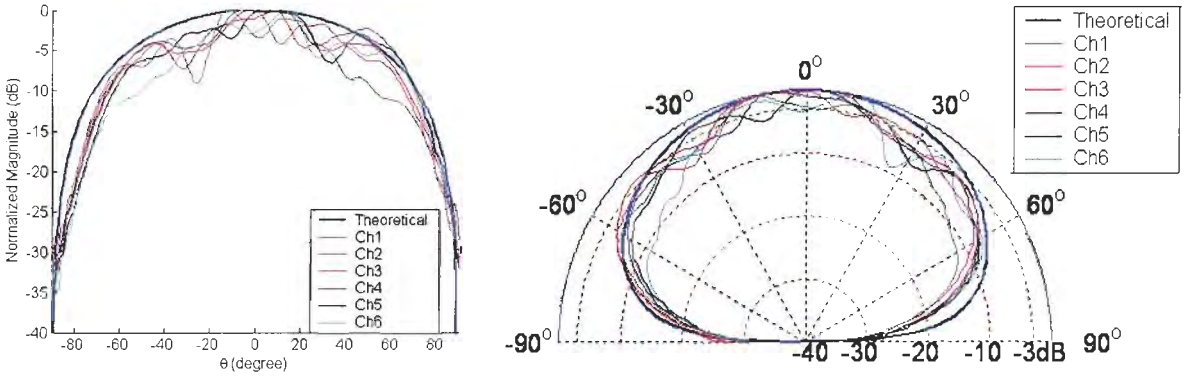

Figure 3.16: Magnitudes of beam patterns for array B

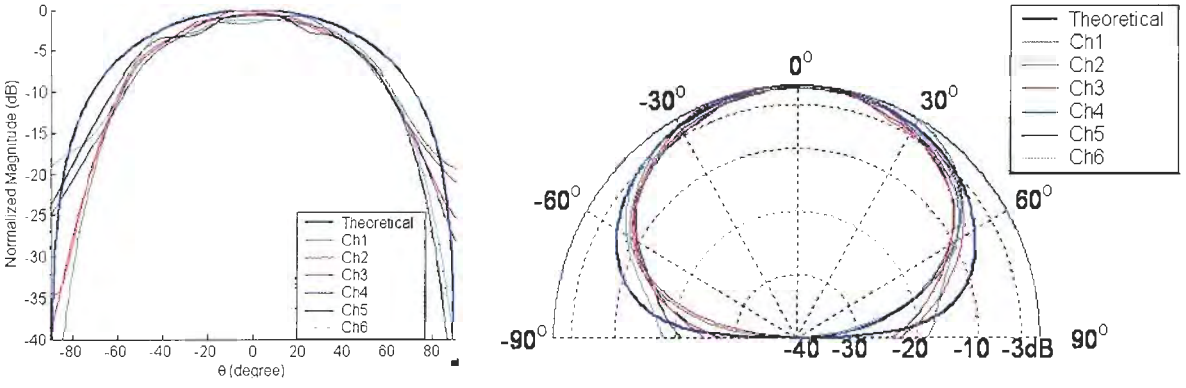

Figure 3.17: Magnitudes of beam patterns for array C

patterns in Figure 3.15, those in Figures 3.16 and 3.17 are not as smooth. Actually, arrays B and C consist of twelve elements and eight elements respectively, but only the center six elements are represented here and used to obtain the aperture function. The other three elements on each side of array B and one element on each side of array C are designed to make the crosstalk uniform over the center six [6]. Despite the careful design, the crosstalk among transducer elements is not uniform, which can be concluded from the ripples in the beam patterns, and will be further discussed in Chapter 4.

The beam pattern measurements yield phase information. The phase of the complex data collected from each hydrophone element is the *absolute phase*; the phase difference between the absolute phase of one channel and that of an assigned reference channel is the *relative phase*. Both absolute and relative phases of arrays A, B and C are plotted in Figures 3.18 - 3.20. In Figures 3.18(b), 3.19(b) and 3.20(b), the relative phases are obtained by assigning the third channel as the reference channel. Also shown is the expected relative phase of each channel (with marker "o").

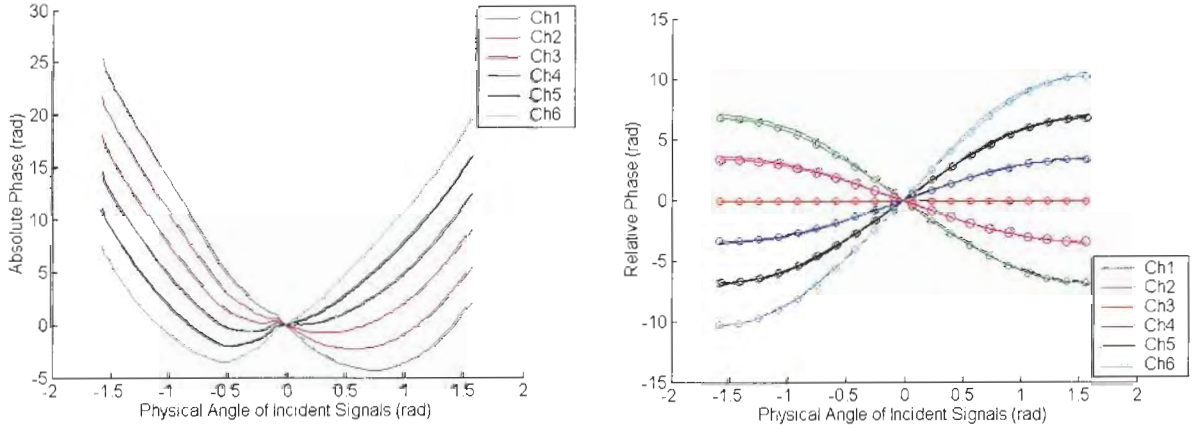

(a) (b)

Figure 3.18: (a) Absolute phase and (b) relative phase of array A

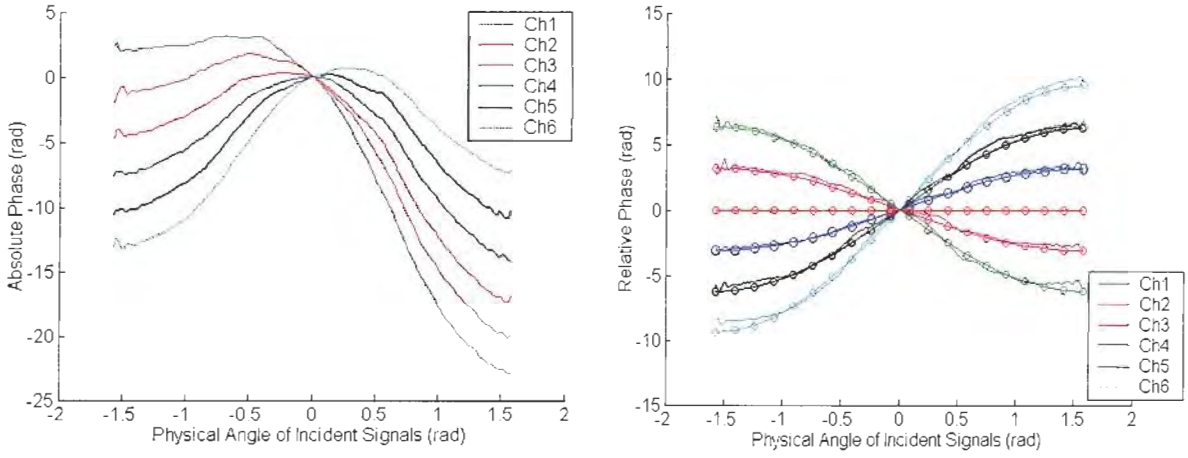

(a) (b)

Figure 3.19: (a) Absolute phase and (b) relative phase of array B

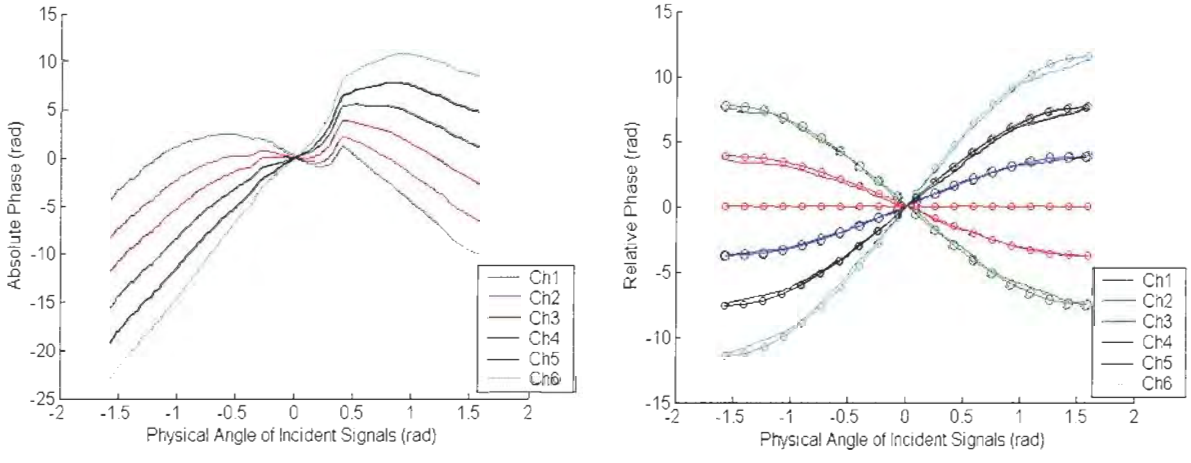

(a) (b)

Figure 3.20: (a) Absolute phase and (b) relative phase of array C

As demonstrated in 3.2.2, both the magnitude and phase information of the beam pattern are essential to obtain the aperture function that is utilized to estimate the inter-element spacing between transducer elements. It is the normalized magnitude and relative phase that are used to obtain aperture functions. While the absolute phase measurement is affected by the different acoustic center of the transducer array while it rotates in the range of $[-\pi/2, \pi/2]$, the use of the relative phase mitigates the effect by subtracting the absolute phase of the assigned channel from the others. In this thesis, we always assign the third channel as the reference channel. By applying the IFT to magnitudes and relative phases of beam patterns of an N-element array, the aperture function of the assigned reference channel is centered at 0 while others are located along the x-axis, as shown in the next subsection.

3.2.5 Aperture Functions Converted from Beam Patterns

We described the method for obtaining the aperture function thoroughly in the previous subsections. By applying the IFT to the visible region of the pattern function $G(u)$, the aperture function is determined. (Remember the beam pattern $B(\theta)$ is measured with the BPMS and $G(u)$ is obtained from applying interpolation to $B(\theta)$.)

The aperture function shown in Figure 3.12 is used as the reference here. The aperture functions of arrays A, B, and C, obtained from the measured beam patterns shown in Figures 3.15 - 3.20, are plotted in Figures 3.21 - 3.23, respectively.

For array A, the aperture functions concentrate over a range of 1.5 cm between $[-1.0, 0.5]$ cm; for array B, the concentration is across 1.4 cm between $[-0.8, 0.6]$ cm; and across 1.7 cm between $[-1.0, 0.7]$ cm for array C. From -20 dB down, all aperture functions fall off rapidly in the same fashion, and reach a floor at about -60 dB. The aperture functions of these three arrays demonstrate similar characteristics to the reference shown in Figure 3.12. However, they are less regular than the reference,

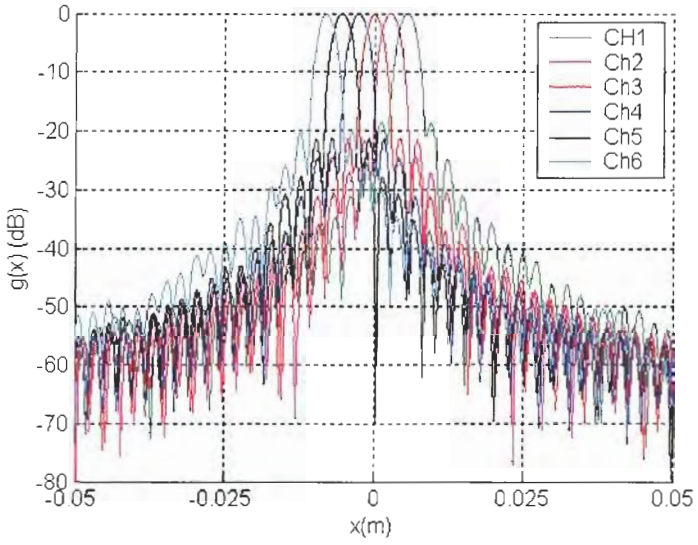

Figure 3.21: The aperture function of array A

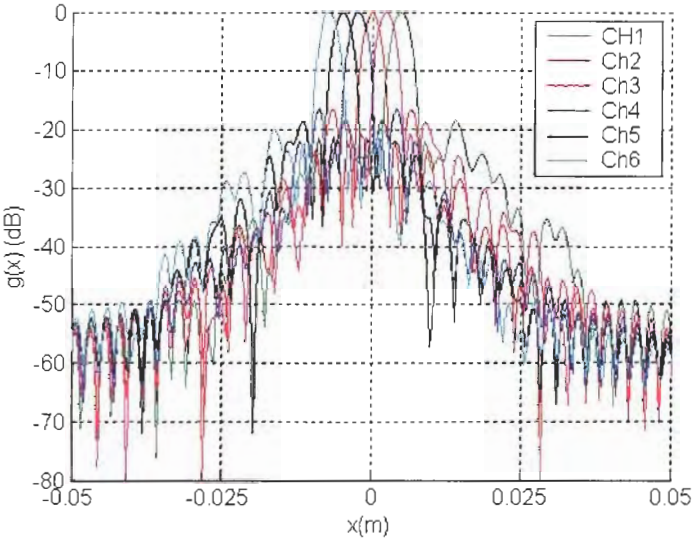

Figure 3.22: The aperture function of array B

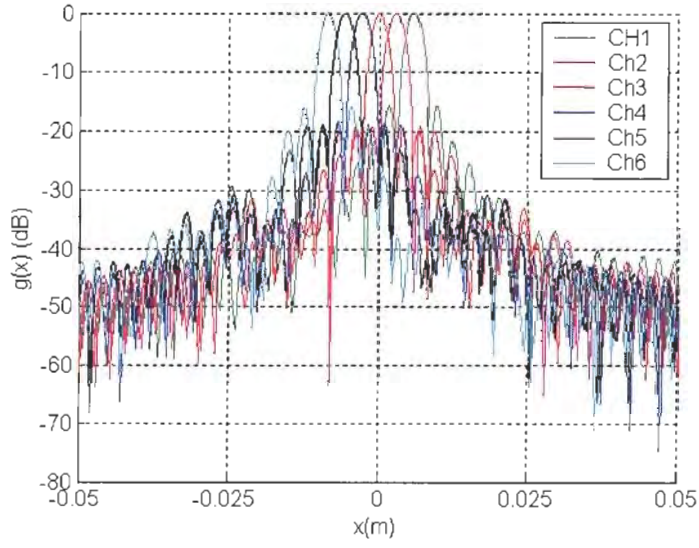

Figure 3.23: The aperture function of array C

which indicates that the three arrays probably have a certain degree of questionable acoustic properties, which will be experimentally measured and discussed in the next chapter.

3.3 Inter-element Spacing Estimation

In the previous section, a method for obtaining the aperture function was described in detail, and also, the expected and experimental aperture functions were presented and compared. In this section, these aperture functions are utilized to estimate the inter-element spacing of multi-element transducer arrays.

3.3.1 Theoretical Results

As we mentioned before, the distance between adjacent curves in the aperture functions represents the distance between the phase centers of adjacent elements in a multi-element transducer array. To improve angle estimation accuracy, the inter-element spacing is obtained from comparing the relative positions of the maximum

values of the aperture functions. For the reference estimated aperture function shown in Figure 3.12(b), the distance between every pair of adjacent peak values is uniformly 0.4 cm, which is identical to the actual value of the original aperture function shown in Figure 3.12(a).

3.3.2 Experimental Results

For the experimental aperture function of array A shown in Figure 3.21, the distances between two adjacent maximum values from the right to the left are 0.28 cm, 0.28 cm, 0.28 cm, 0.28 cm, and 0.27 cm; for the experimental aperture functions of array B shown in Figure 3.22, the distances are 0.26 cm, 0.25 cm, 0.26 cm, 0.25 cm, and 0.26 cm; for those aperture functions of array C shown in Figure 3.23, the distances are 0.29 cm, 0.29 cm, 0.29 cm, 0.29 cm and 0.30 cm in sequence. Table 3.1 lists these results, and also the design inter-element spacing.

Table 3.1: Inter-element spacing measurements

	Array A	Array B	Array C
Pair 1 (cm)	0.28	0.26	0.29
Pair 2 (cm)	0.28	0.25	0.29
Pair 3 (cm)	0.28	0.26	0.29
Pair 4 (cm)	0.28	0.25	0.29
Pair 5 (cm)	0.27	0.26	0.30
Design inter-element spacing (cm)	0.27	0.25	0.30

The measurements of the inter-element spacing of arrays A, B and C differ from the design values by 3.7%, 4%, and 3.33%, respectively. This close agreement between

the design values and experimental results demonstrated in Table 3.1 is evidence that the arrays were actually constructed properly. Furthermore, because arrays A, B and C are constructed with transparent polyurethane, the estimated spacings shown in Table 3.1 were also verified by direct measurement to approximately ± 0.01 cm. In practice, the aperture function has been effectively utilized in the URL to investigate the relative position and inter-element spacing between transducer elements for arrays that are potted with opaque polyurethane. The results of six of these arrays are listed in Table 3.2 to further verify the suitability of the aperture function method for estimating the inter-element spacing. Each array is measured twice. Two results for each distance and the difference between them are represented by d_1, d_2, and $|\Delta d|$ in Table 3.2, respectively. The largest difference between the two results is 0.0036 cm demonstrating the repeatability of the aperture function method to within approximately 0.004 cm.

Table 3.2: Inter-element spacing measurements of six testing arrays

Array		Pair 1 (cm)	Pair 2 (cm)	Pair 3 (cm)	Pair 4 (cm)	Pair 5 (cm)
Array 1	d_1	0.3614	0.3475	0.3677	0.3473	0.3380
	d_2	0.3617	0.3485	0.3672	0.3475	0.3387
	$\|\Delta d\|$	0.0003	0.0010	0.0005	0.0002	0.0007
Array 2	d_1	0.3510	0.3468	0.3447	0.3485	0.3490
	d_2	0.3492	0.3504	0.3414	0.3480	0.3488
	$\|\Delta d\|$	0.0018	0.0036	0.0033	0.0005	0.0002
Array 3	d_1	0.3351	0.3657	0.3470	0.3082	0.3602
	d_2	0.3342	0.3660	0.3473	0.3073	0.3625
	$\|\Delta d\|$	0.0009	0.0003	0.0003	0.0009	0.0023
Array 4	d_1	0.3699	0.3040	0.3889	0.3640	0.3713
	d_2	0.3703	0.3039	0.3892	0.3642	0.3711
	$\|\Delta d\|$	0.0004	0.0001	0.0003	0.0002	0.0002
Array 5	d_1	0.3769	0.3566	0.3381	0.3418	0.3883
	d_2	0.3786	0.3564	0.3362	0.3426	0.3893
	$\|\Delta d\|$	0.0017	0.0002	0.0019	0.0008	0.0010
Array 6	d_1	0.3895	0.3517	0.3281	0.3416	0.3824
	d_2	0.3893	0.3519	0.3281	0.3408	0.3828
	$\|\Delta d\|$	0.0002	0.0002	0.0000	0.0008	0.0004

Chapter 4

Crosstalk Measurement and Analysis

Although transducer arrays offer gains in radiated power and directivity over single element transducers, the mutual coupling between elements introduces crosstalk and reduces performance. For example, crosstalk leads to errors in determining the angle-of-arrival of incident signals. It is usual for transducer arrays to be analyzed assuming an ideal array and crosstalk between elements is neglected. In practice, when the separation between elements is larger than one wavelength, crosstalk is weak and the assumption of negligible inter-element crosstalk is valid. However, for arrays with smaller spacing, which is necessary to avoid grating lobes, crosstalk is an issue [25].

The primary focus of this chapter is a method for investigating and quantifying the impact of crosstalk. This chapter includes the following: 1) a brief description of the configuration and components of transducer arrays built by the URL; 2) a proposed method for measuring crosstalk; 3) experimental results are presented for different transducer arrays: A (built by the URL), B (built by the Simrad) and C (built by the Benthos); 4) factors affecting crosstalk are investigated; and 5) the effects of crosstalk on array performance are analyzed.

4.1 Transducer Array

The typical geometry of transducer arrays used for MASB sonar and built by the URL is illustrated in Figure 4.1. These arrays are composed of six piezoelectric ceramic elements separated by an acoustically and electrically inactive material, and are covered and filled with a waterproof material.

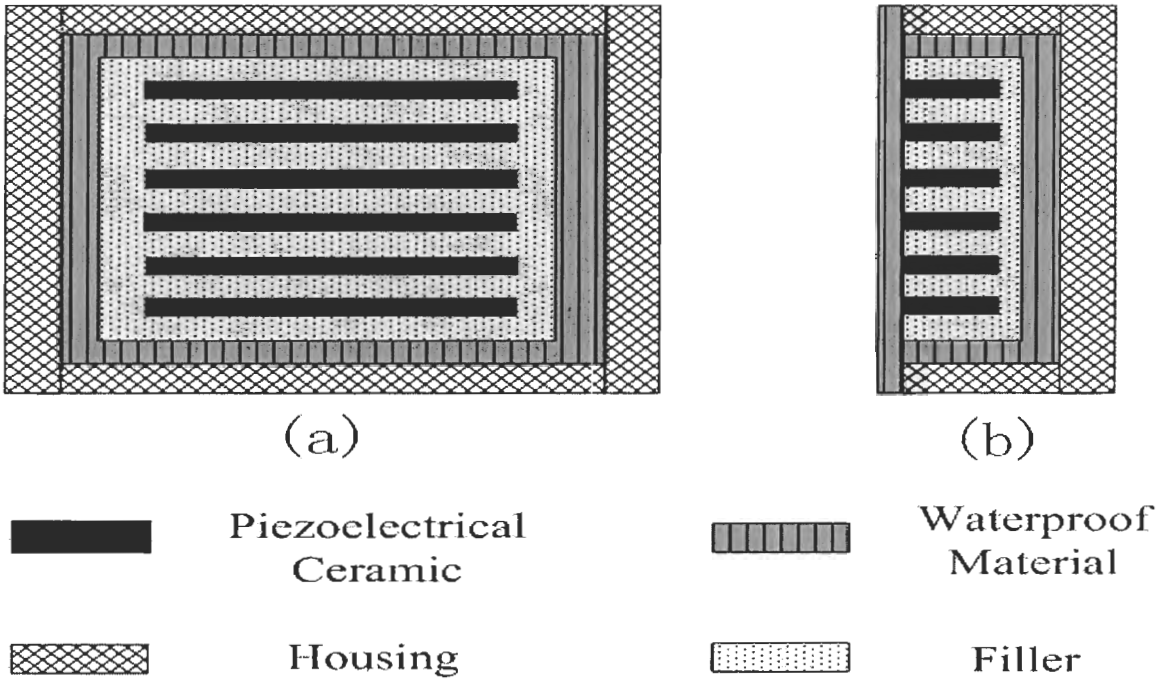

Figure 4.1: The (a) front view and (b) side view of an array built by the URL

These transducer elements embedded in arrays have a typical beamwidth of 70^o. The typical center-to-center spacing between transducer elements is $\lambda/2$. Usually, these transducers operate at their resonant frequency. If the resonant frequency is 300 kHz, the wavelength, λ, is around 5×10^{-3} m, and the transducer elements are typically designed to be separated by 2.5×10^{-3} m from center-to-center.

4.1.1 Piezoelectric Ceramic

Piezoelectric ceramic is widely used for transducer elements because it has stable and suitable piezoelectric properties, and it is possible to manufacture it in a variety of shapes and sizes. Piezoelectric properties of the transducer elements are obtained through polarization, a procedure during which the ceramic is heated to its Curie temperature and then cooled down slowly in the presence of a strong electrical field [26]. The electrical field is applied to the ceramic to generate the piezoelectric effect in the required dimension [26], such as the thickness dimension of the transducers described in this thesis. Ideally, a piezoelectric ceramic element changes its physical shape only in the polarized dimension when an electrical or an acoustic field is applied. However, this is not the case in practice, since changes in other dimensions are often excited at the same time. Fortunately, as shown in Figure 4.1, the ceramic bars of transducer arrays described in this thesis are much longer than the transducer thickness (length/thickness ratio $\approx$ 30). With a large length to thickness ratio, the frequency of vibration in the length dimension is much lower than the frequency range of practical interest, so the effect is negligible [26]. The ratio of the width to thickness dimensions is usually much less than the ratio of the length to thickness dimensions (width/thickness ratio $\approx$ 0.2), and the vibration frequency of the width dimension is not negligible. The crosstalk discussed in this thesis is caused predominately from changes in transducer width.

4.1.2 Housing

The piezoelectric elements of transducer arrays are typically mounted in a housing whose main function is to provide mechanical support for the array. Aluminium is primarily used for array housings since it is light-weight and durable.

It has been determined experimentally that the housing can be a significant contributor to crosstalk [27, 28], because the acoustic waves can potentially travel back and forth between elements and the housing. Fortunately, an acoustic isolation material can be placed between the transducer elements and the housing to attenuate acoustic wave propagation, and consequently, mitigate crosstalk generated by the housing.

4.1.3 Filler

As described earlier, there should be enough separation between the housing and transducer elements to mitigate crosstalk mechanisms introduced by the housing. Similarly, there should be sufficient gaps between transducer elements of an array to minimize interference between elements [29]. These gaps are usually filled with an acoustically and electrically inactive material to prevent acoustic wave propagation between elements. Examples of such materials are Corprene, Sonite and onionskin paper [9]. Corprene is employed in the URL designs due to its low cost, availability, reasonably low compressibility and good acoustic isolation properties. Corprene can not be used for deep water applications because it will ultimately compress beyond accepted tolerances. But for shallow water applications, depth less than 250 m, it works well.

4.1.4 Waterproof Material

A waterproof material is used to protect the piezoelectric transducer elements. This material is usually selected to possess approximately identical acoustic properties with water to reduce energy loss at the water interface. However, this causes significant energy loss at the interface between this covering material and ceramic elements. Ideally, one would want to provide a matching layer to match the acoustic impedance

of the ceramic to the water. However, matching layers tend to work well only on axis and not for signals off axis. Also they tend to produce secondary resonances and crosstalk, both of which should be avoided. Polyurethane PR1570 is chosen as the waterproof covering for transducer arrays manufactured by the URL.

4.2 Crosstalk Measurements

This section is divided into the following five parts: 1) a description of crosstalk; 2) a review of methods to analyze crosstalk; 3) a proposed method to measure crosstalk; 4) a comparison of the experimental results for transducer arrays A, B and C; and 5) a summary of the factors potentially affecting crosstalk.

4.2.1 Electrostatic and Acoustic Crosstalk

Depending on how crosstalk is generated, it is categorized as *electrostatic crosstalk* or *acoustic crosstalk*. The nature of each crosstalk mechanism is explained below by describing an example of a hydrophone array.

A piezoelectric ceramic transducer element is like a capacitor because of the conducting surfaces on the top and bottom. The stored charge in the capacitor generates an electrical field which can couple to adjacent elements. The electrical field generates a voltage in nearby elements, and therefore, this capacitive coupling generates crosstalk. Crosstalk generated by mutual capacitive coupling between transducer elements is called electrostatic crosstalk. Electrostatic crosstalk is practically instantaneous, and can be controlled effectively by carefully shielding the interconnection between transducer elements [30]. Actually, the electrostatic crosstalk is low even without the shield in the transducer arrays built by the URL, and does not cause significant variation of beam patterns.

A second crosstalk mechanism arises from acoustic wave propagation between array elements. In addition to the direct signal, each element also receives signals which are re-radiated by the other elements. This type of mutual coupling is called acoustic crosstalk. The amplitude of acoustic crosstalk depends on the magnitude of the propagating waves, and the phase is determined by the characteristics of the radiating and receiving element, and also the propagation delay between them [31]. Unlike electrostatic crosstalk, acoustic crosstalk is not instantaneous and depends on the speed at which sound waves propagate between array elements [30]. A common approach to minimize acoustic crosstalk is to fill the inter-element gaps with acoustically inactive material. This chapter focuses on exploring acoustic crosstalk between transducer elements.

4.2.2 Review of Crosstalk Analysis Methods

It is widely recognized that crosstalk in acoustic transducer arrays is very complicated and is affected by many factors, and currently, not all crosstalk mechanisms are well understood. As a result, it is difficult to establish a model to accurately reflect each individual crosstalk factor. Several approaches based on numerical methods and experimental methods have been proposed [32].

Numerical methods solve the fundamental electro-elastic equations governing piezoelectric media [5]. However, they require a complete mathematical description of the transducer and intensive computation if applied to arrays large in size. Therefore, their application is limited to transducer arrays for which practical computer analysis programs are available [5].

On the other hand, experimental approaches potentially can accurately measure the crosstalk of transducer arrays designed for specific applications. Furthermore, even if the internal geometrical parameters and acoustic properties of array components

are not available, the experimental method is suitable for exploring crosstalk inside the arrays. Therefore, in this thesis, crosstalk is investigated by experiment.

4.2.3 Crosstalk Measurement System

The proposed procedure to measure crosstalk is to excite a single element with a sinusoidal wave, and measure the induced response on each of the other array elements. Comparing the magnitudes and phase differences between the driving and induced sinusoidal signal yields information about crosstalk between elements. The employment of a periodic sinusoidal wave allows us to investigate steady-state crosstalk at a specific frequency. Some literature records a method of crosstalk measurement that drives the elements with pulses to investigate the transient nature of crosstalk [32]. This thesis is limited to steady state crosstalk measurements. Figure 4.2 illustrates schematically the experimental circuit used in this thesis to explore crosstalk between transducer elements.

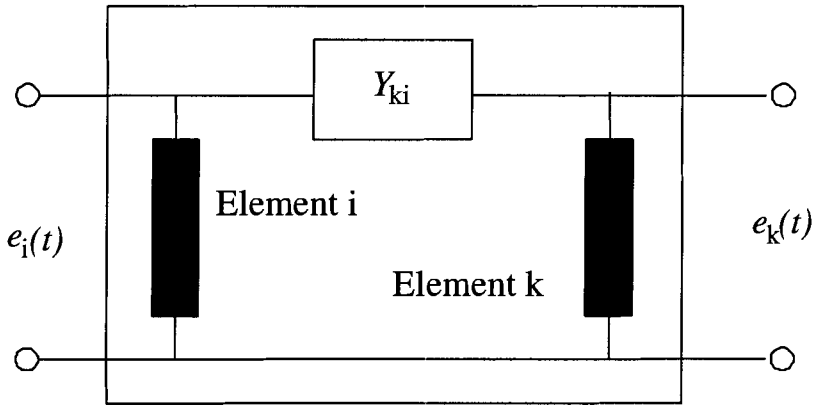

Figure 4.2: Crosstalk measurement circuit

In Figure 4.2, $e_i(t)$ is the driving signal applied to the ith element, and $e_k(t)$ is the induced response on the kth element caused by crosstalk between these two elements. Y_{ki} is the admittance representing crosstalk between the ith element and the kth

element [33].

In the crosstalk measurement system, a programmable function generator (Sony-Tektronix AFG 310) is used to provide the sinusoidal signal $e_i(t)$. A programmable oscilloscope (Tektronix 3034) is employed to record both $e_i(t)$ and $e_k(t)$. The waveforms of $e_i(t)$ and $e_k(t)$ are transferred from the oscilloscope to a personal computer for subsequent analysis. Programs written in MATLAB are used to control the system for performing the measurements. The control of the generator and oscilloscope from the computer and the communication between them are accomplished through a national instrument General Purpose Interface Bus (GPIB) installed on the computer.

The level of crosstalk in the array is defined as an *interaction* function equal to the ratio of the voltage across the non-driven element to the voltage across the driven element, and is represented by Γ in this thesis. If the driven and induced signal can be expressed by $e_i(t)$ and $e_k(t)$, and are given by:

$$\begin{aligned} e_i(t) &= E_i \cos(2\pi f_0 t + \alpha_i) \\ e_k(t) &= E_k \cos(2\pi f_0 t + \alpha_k) \end{aligned} \tag{4.1}$$

where f_0 is the frequency of the signal, the magnitude and phase of the interaction at the frequency of f_0 Hz, $\Gamma(f_0)$, are given by Equations (4.2) and (4.3), respectively.

$$|\Gamma(f_0)| = \frac{E_k}{E_i} \tag{4.2}$$

$$\angle\Gamma(f_0) = \alpha_k - \alpha_i \tag{4.3}$$

Usually, the magnitude of the interaction is expressed in decibels, so Equation (4.2) becomes:

$$\Gamma(f_0)(dB) = 20\log_{10}(|\Gamma(f_0)|) = 20\log_{10}(\frac{E_k}{E_i}) \tag{4.4}$$

To analyze crosstalk at different frequencies in an array, the driving signal is swept over a band of frequencies near the resonant frequency of the transducer elements. Also, the measurements are performed between all possible combinations of distinct transducer elements, i.e., $i \neq k$.

4.2.4 Experimental Results

In the following paragraphs, the experimental results of crosstalk measurements of transducer arrays A, B and C are presented. First, we present array A for the case of $i = 3$ as an illustrative example to describe the crosstalk pattern. After this, the crosstalk in arrays A, B and C versus the frequency of the driving signal and the distance between elements is shown and discussed. Finally, conclusions are drawn from the experimental results indicating that crosstalk generally achieves a peak at the resonant frequency and decreases with distance, as results from arrays A and C show; however, many other factors, such as internal interference, and multiple coupling paths, have significant effect on the crosstalk pattern, as results from array B show.

In the crosstalk measurements performed for this thesis, the driving signals are sinusoidal waves with peak to peak values of 20V over a band of frequencies near 300 kHz.

Figure 4.3 illustrates the results of crosstalk measurements between the 3rd element and the other elements in array A. The crosstalk levels between the 3rd element and the 2nd/4th element are similar. This symmetry is a result of the physical properties: identical elements and equal distance between the driven element and the two induced elements. The difference is probably due to asymmetrical distances between the 2nd and 4th element in relation to other elements and the housing. In addition, the magnitude of crosstalk reaches a maximum at the resonant frequency, and decreases for frequencies away from the resonant frequency. At the resonant frequency,

the amplitude of vibration of the driven element is maximized and spurious wave propagation is also the largest generating the higher levels of crosstalk.

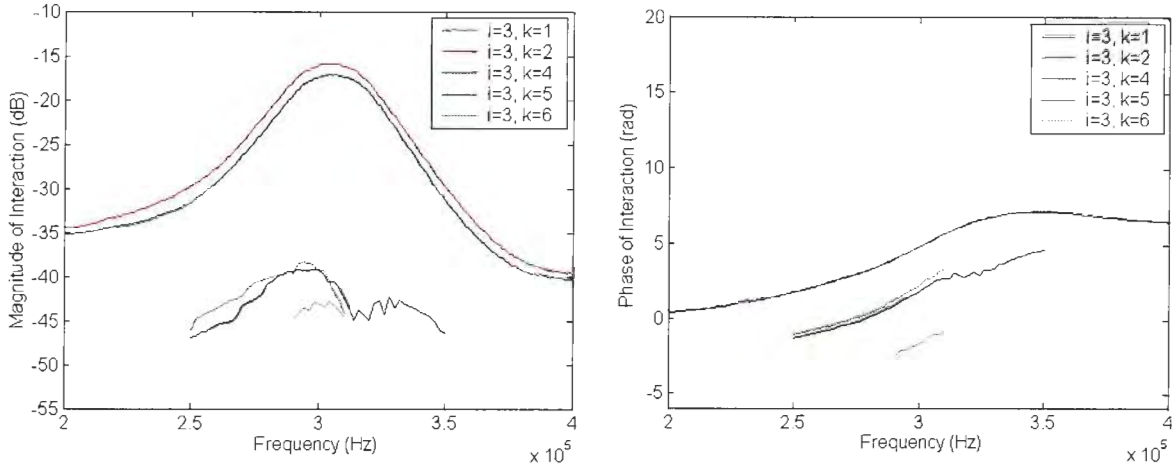

(a) (b)

Figure 4.3: (a) Magnitude and (b) phase of interaction in array A when i=3

The frequency range while investigating crosstalk between more distant elements, i.e., the 3rd and the 1st/5th/6th elements, is set narrower than the frequency range while investigating nearest neighbors, because the crosstalk levels outside of this frequency range are too low to be measured accurately by the oscilloscope. It is evident from Figure 4.3(a) that the coupling between the 3rd and its distant neighbors is smaller than that between the 3rd element and its nearest ones, which indicates that the level of crosstalk decreases as the distance between the driven element and the interfered element increases.

Crosstalk measurements while exciting the other elements in array A were made and the results are shown in Figures 4.4 - 4.8, where i denotes the driven element and k denotes the interfered element.

As shown in Figures 4.4 - 4.8, the magnitude and phase of crosstalk over the

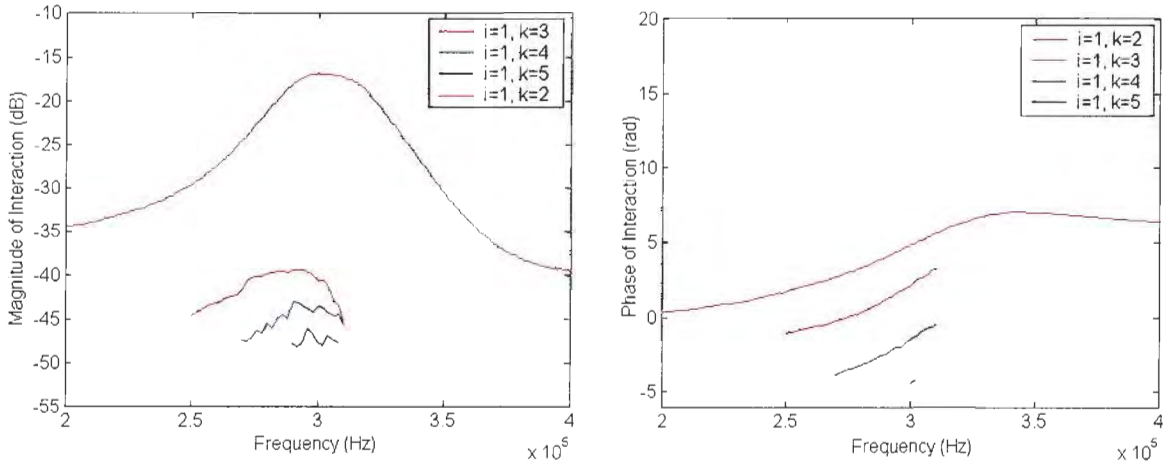

(a) (b)

Figure 4.4: (a) Magnitude and (b) phase of interaction in array A when i=1

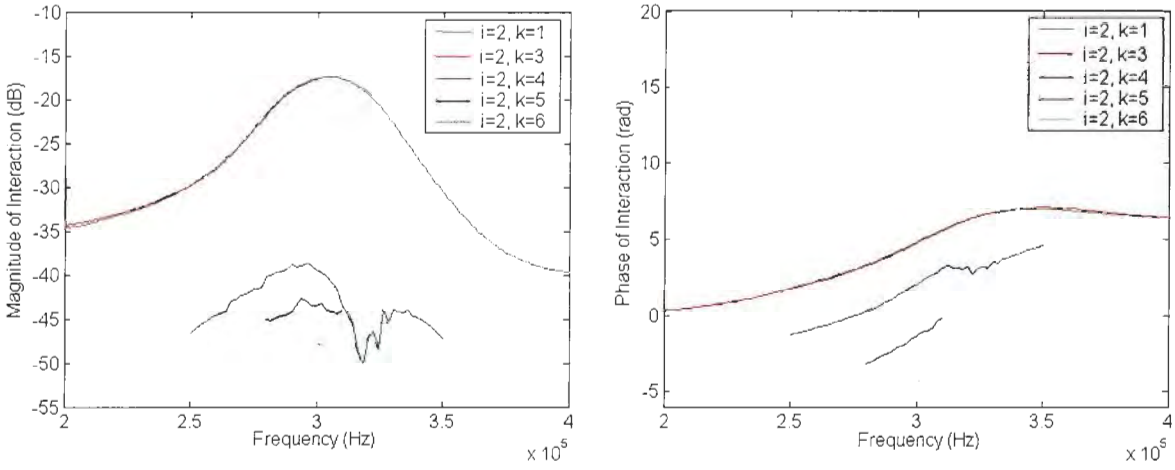

(a) (b)

Figure 4.5: (a) Magnitude and (b) phase of interaction in array A when i=2

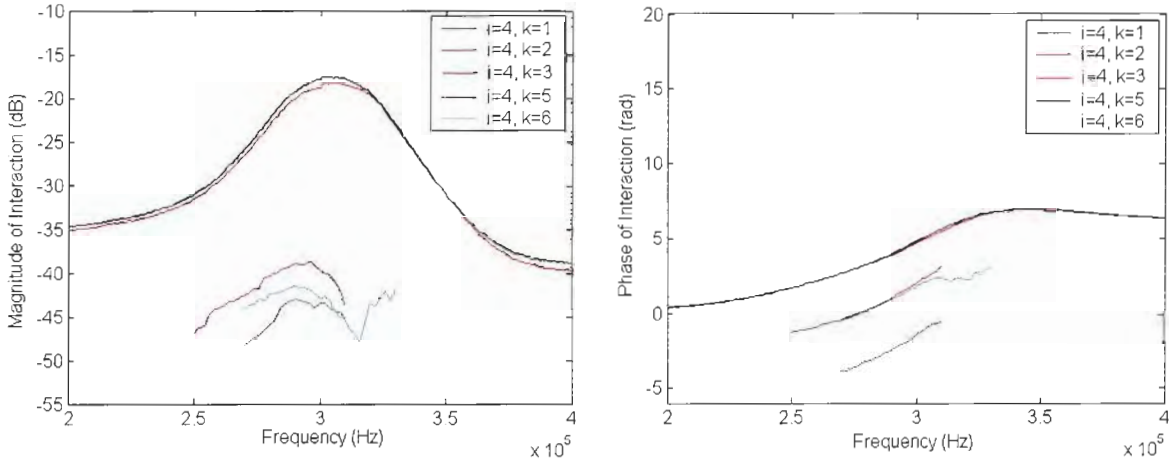

(a) (b)

Figure 4.6: (a) Magnitude and (b) phase of interaction in array A when i=4

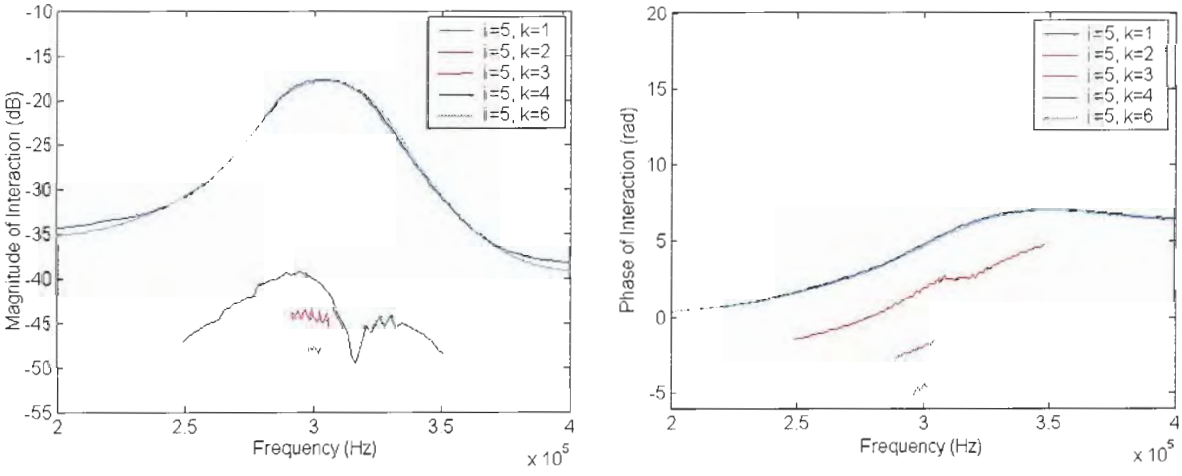

(a) (b)

Figure 4.7: (a) Magnitude and (b) phase of interaction in array A when i=5

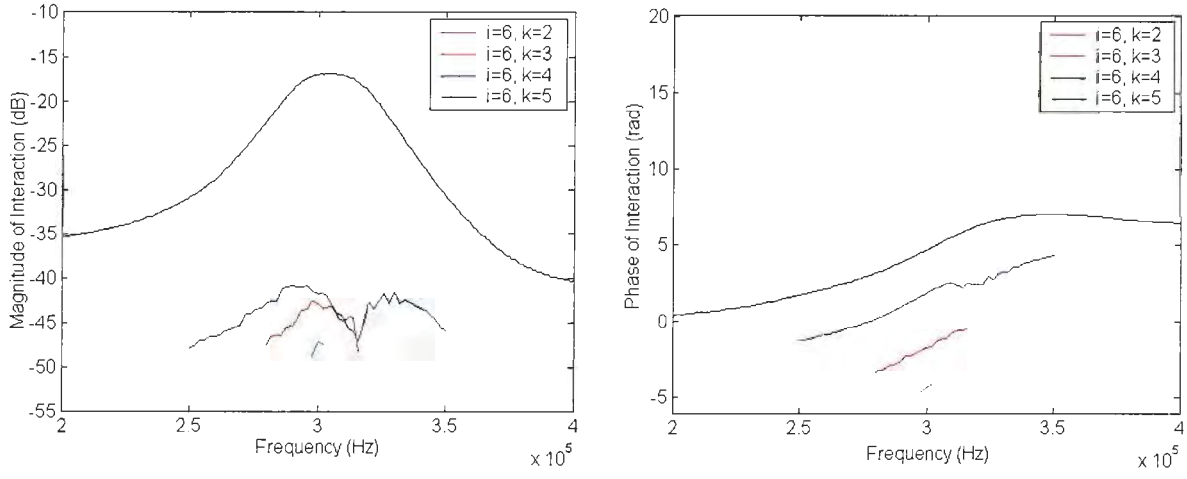

(a) (b)

Figure 4.8: (a) Magnitude and (b) phase of interaction in array A when i=6

measured frequency band in array A are approximately symmetric between elements which are equally spaced from the driven elements. Also, the crosstalk levels decrease monotonically as the operating frequency moves away from the resonant frequency of the transducer element. Furthermore, due to the symmetry of the array, the measurement results while exciting the 1st, 2nd and 3rd element are very similar to those obtained when exciting the 6th, 5th and 4th element, respectively.

The magnitude and phase difference of crosstalk were also measured for each element of arrays B and C. Figures 4.9 - 4.10 show the experimental data obtained while exciting the 3rd element and measuring the induced response on other array elements. The data obtained from exciting each element of arrays B and C are shown in Appendix A.

As shown in Figures 4.9 - 4.10, the relative magnitudes and phases of crosstalk tend to vary in a less regular pattern in arrays B and C than in array A over a frequency range of [200, 400] kHz, especially in array B.

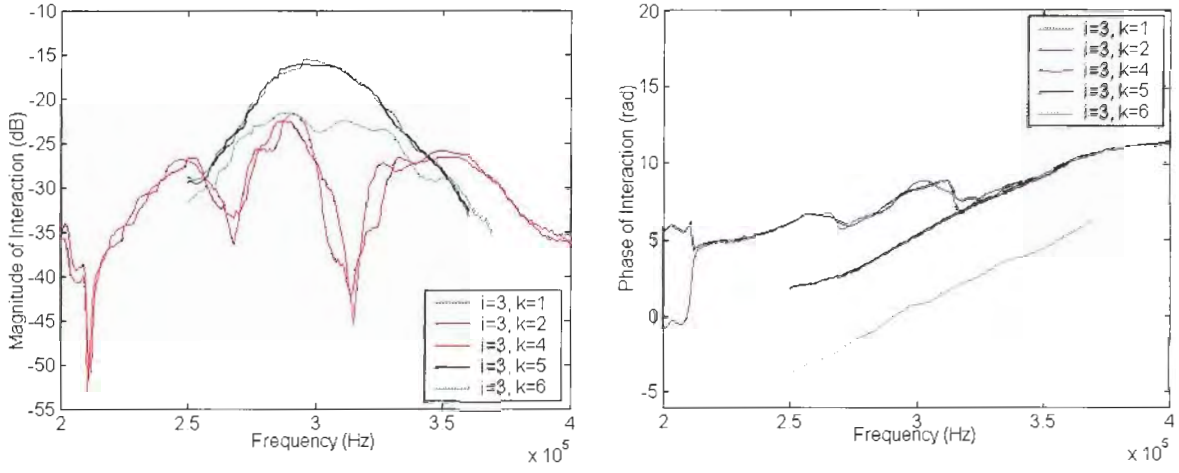

(a) (b)

Figure 4.9: (a) Magnitude and (b) phase of interaction in array B when i=3

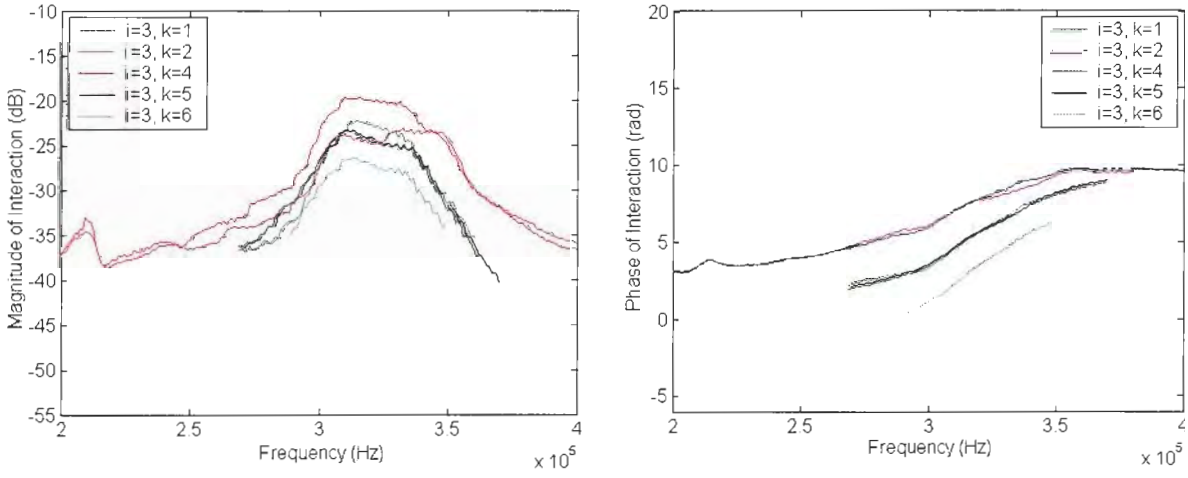

(a) (b)

Figure 4.10: (a) Magnitude and (b) phase of interaction in array C when i=3

In array B, the magnitude peaks correspond approximately to the resonant frequency. However, for the magnitude of crosstalk between the 3rd and 2nd/4th element, the magnitudes do not monotonically decrease as the frequency deviates from its resonant frequency. The crosstalk has local maximums at frequencies of 250k, 290k, and 350k Hz, and minimums at frequencies of 215k, 270k, and 315k Hz. These maximums may be caused by constructive interference from multiple acoustic waves generated by the housing and other elements, while minimums may be caused by destructive interference from multiple acoustic waves [34]. The phase difference over the measured frequency band varies in an irregular pattern, in that the plots of the phase differently spaced elements overlap at some frequencies.

In array C, the crosstalk magnitudes reach a maximum around the resonant frequency, and tend to decrease as the frequency deviates further away from the resonance.

Generally, the most common way to display crosstalk levels in an array is to plot the results at the resonant frequency versus normalized distance relative to the signal wavelength [35]. Before we move on to present crosstalk in this way, the first thing to note is that we assume the actual distances between neighboring elements of arrays A, B and C are identical with the design values, which are 0.543λ, 0.5λ, and 0.607λ as shown in Chapter 2 (λ is the wavelength in water at the frequency of 300 kHz). Taking array A as an example, while the 3rd element is excited, the measured responses on the 2nd/4th, 1st/5th and 6th elements are plotted at 0.543λ, $2 \times 0.543\lambda$, and $3 \times 0.543\lambda$, respectively. Using this display technique, the crosstalk at the frequency of 300 kHz while exciting each element and measuring the response on the other elements of arrays A, B and C are replotted in Figures 4.11 - 4.13.

While Figures 4.3 - 4.10 illustrate the relationship between crosstalk and frequency,

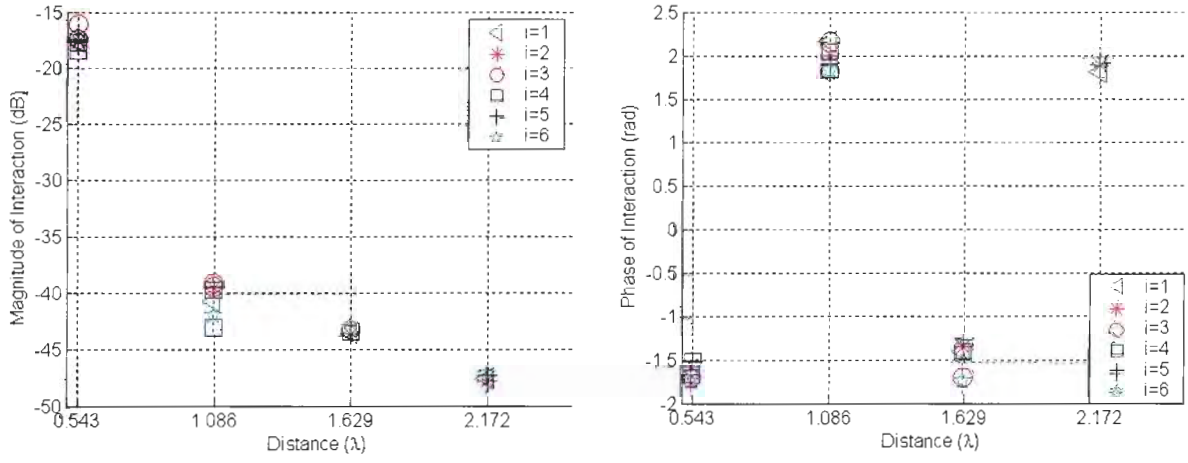

(a) (b)

Figure 4.11: (a) Magnitude and (b) phase of interaction vs λ at 300 kHz in array A

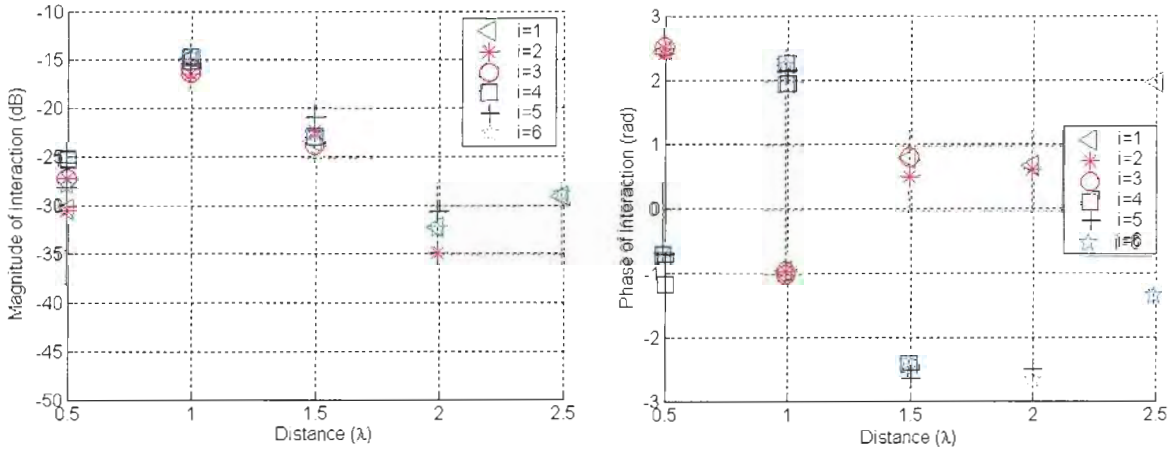

(a) (b)

Figure 4.12: (a) Magnitude and (b) phase of interaction vs λ at 300 kHz in array B

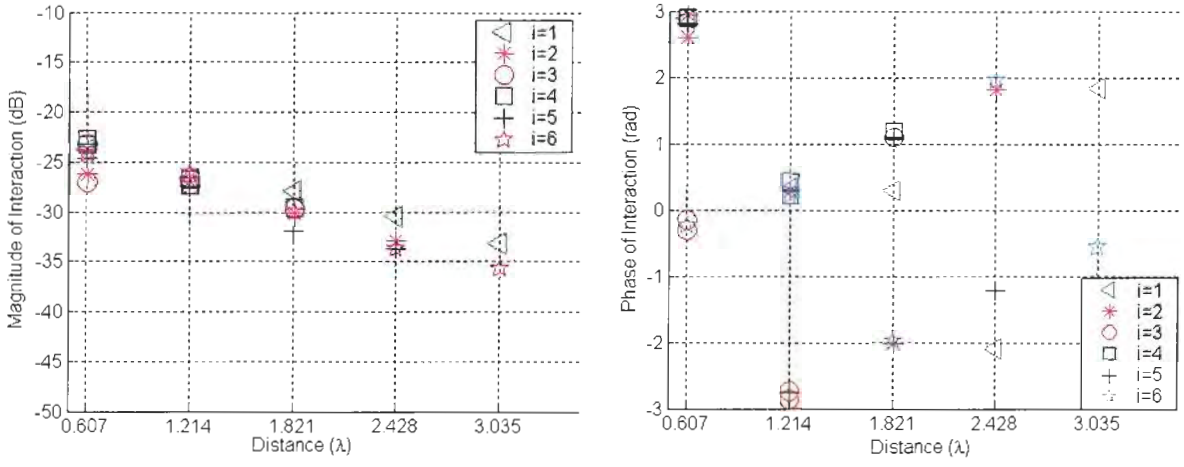

(a) (b)

Figure 4.13: (a) Magnitude and (b) phase of interaction vs λ at 300 kHz in array C

Figures 4.11 - 4.13 show the variation with distance. For array A, the magnitude of interaction between adjacent elements is about -15 dB, and is about 25 dB lower between elements separated by one element, and even lower between more distantly spaced elements. The crosstalk between the two outside elements is too insignificant to be observed. Therefore, for array A the main source of crosstalk is between adjacent array elements. The phase between equally spaced elements is approximately same. Also, it displays periodic features in that the close neighbors and the third neighbors, the second neighbors and the fourth neighbors have the same phase difference. Overall, the data plotted in Figure 4.11 show that for array A, crosstalk varies in a regular pattern, and is approximately the same between equally spaced elements.

The data plotted in Figure 4.12 indicate that crosstalk of array B changes unexpectedly as the distance between elements increases. The magnitude of interaction between the driven element and its second neighbors is about 10 dB higher than that between the driven element and its closest neighbors. The phase delay is not same,

but around π difference between equally spaced elements. These results indicate complicated interference mechanisms in array B that may be caused by multiple coupling paths between the elements and the housing and surface layer. We conclude that the crosstalk in array B changes irregularly and unexpectedly through complicated coupling mechanisms.

In array C, the magnitude of interaction is inversely proportional to the distance between elements, and is about 3 dB less between those separated by one more element. This indicates regular crosstalk patterns; however, multiple crosstalk sources are present in array C, because the magnitude of interaction between widely spaced elements is not significantly less than that between adjacent elements. Also, the phase of interaction in array C does not change as regularly as that in array A.

The interaction data plotted in Figures 4.3 - 4.10 can also be easily represented with an interaction matrix $\mathbf{\Gamma}$, whose element, $\mathbf{\Gamma}_{ki}$ if $k \neq i$, stands for crosstalk caused by the ith element on the kth element; if $k = i$, $\mathbf{\Gamma}_{ki}$ is the response on the driven element, and is 0 dB. The interaction matrix of an N-element array has dimensions of $N \times N$ and is capable of representing the crosstalk between all combinations of two elements. The following interaction matrices represent the crosstalk levels of arrays A, B and C at 300 kHz. For array A, the interaction matrix at 300 kHz is:

$$\mathbf{\Gamma}_A = \begin{bmatrix} 0 & -17.65e^{-j1.57} & -39.41e^{j2.17} & -43.50e^{j4.88} & -47.28e^{j1.94} & -\infty \\ -17.63e^{-j1.60} & 0 & -16.04e^{-j1.71} & -39.69e^{j2.06} & -43.53e^{-j1.26} & -47.14e^{j1.97} \\ -40.76e^{j2.07} & -17.48e^{-j1.75} & 0 & -18.42e^{-j1.67} & -39.39e^{j1.91} & -43.02e^{-j1.72} \\ -43.62e^{j4.90} & -39.55e^{j2.02} & -17.39e^{-j1.70} & 0 & -17.38e^{-j1.52} & -41.96e^{j1.85} \\ -47.64e^{j1.84} & -43.53e^{-j1.33} & -39.15e^{j1.82} & -17.70e^{-j1.61} & 0 & -17.07e^{-j1.74} \\ -\infty & -47.78e^{j1.92} & -43.15e^{-j1.68} & -43.02e^{j1.84} & -17.61e^{-j1.66} & 0 \end{bmatrix}$$

The interaction matrix of array B at the frequency of 300 kHz is:

$$\mathbf{\Gamma}_B = \begin{bmatrix} 0 & -30.50e^{j2.43} & -15.77e^{-j0.95} & -22.97e^{j3.89} & -30.61e^{j10.06} & -28.89e^{j4.96} \\ -30.42e^{j8.74} & 0 & -27.25e^{j8.81} & -14.74e^{j1.94} & -20.93e^{j9.93} & -32.46e^{j9.89} \\ -14.81e^{j5.32} & -27.25e^{j8.80} & 0 & -25.35e^{j5.10} & -15.27e^{j2.15} & -22.59e^{j3.90} \\ -23.35e^{j0.80} & -16.32e^{-j0.96} & -27.25e^{j8.81} & 0 & -25.56e^{j5.57} & -14.58e^{j8.52} \\ -32.25e^{j0.70} & -22.35e^{j0.51} & -16.20e^{-j1.00} & -25.28e^{j5.57} & 0 & -28.10e^{j5.63} \\ -29.08e^{j1.95} & -34.83e^{j6.92} & -23.71e^{j0.81} & -15.04e^{j2.26} & -28.16e^{j5.60} & 0 \end{bmatrix}$$

The interaction matrix of array C at the resonant frequency of 300 kHz is:

$$\mathbf{\Gamma}_C = \begin{bmatrix} 0 & -23.78e^{j2.60} & -27.28e^{j3.41} & -29.58e^{j1.19} & -33.68e^{-j1.22} & -35.67e^{-j0.58} \\ -23.78e^{j2.89} & 0 & -26.98e^{j6.13} & -27.33e^{j6.69} & -31.94e^{j1.09} & -33.65e^{j1.94} \\ -26.63e^{j0.31} & -26.23e^{j2.94} & 0 & -23.33e^{j2.91} & -27.44e^{-j2.76} & -29.98e^{j4.29} \\ -27.94e^{j6.58} & -26.95e^{j0.27} & -23.1e^{j5.98} & 0 & -23.16e^{j2.79} & -26.08e^{j0.21} \\ -30.51e^{j4.19} & -30.08e^{j4.26} & -26.64e^{j3.54} & -22.64e^{j2.88} & 0 & -24.26e^{j6.05} \\ -33.24e^{j1.84} & -32.98e^{j1.81} & -29.61e^{j1.10} & -26.82e^{j0.20} & -24.54e^{j2.81} & 0 \end{bmatrix}$$

The magnitudes in the above interaction matrices are on a decibel scale, and they are converted into a linear scale in the following analysis. In general, the interaction matrix $\mathbf{\Gamma}$ has no special structure. However, for an ideal N-element array with no mutual coupling we expect an $N \times N$ identity matrix. For a symmetrical array which has infinite boundary conditions and well balanced crosstalk, we expect an $N \times N$ interaction matrix with descending terms in the same row or column. The rationale behind this model is the fact that in such an array, the cross coupling decreases with distance between elements.

In summary, we can easily explore crosstalk in an array by exciting one element and measuring the response of the other elements. By investigating the crosstalk in transducer arrays A, B and C, it is concluded that in general terms, the magnitude

of crosstalk is maximum at the resonant frequency of elements, and decreases with distance. However, these conclusions are not true for those acoustic transducer arrays with significant internal interference and multiple coupling paths.

4.2.5 Parameters Affecting Crosstalk

In the previous part of this section, a method for measuring crosstalk was described and experimental results were presented for three transducer arrays. In the following paragraphs, the parameters that affect crosstalk are discussed.

The most significant observation from the experimental measurements is that crosstalk depends on the separation between transducer elements in an array. For a linear transducer array with uniform acoustic characteristics, such as array A, crosstalk levels are inversely proportional to the distance between the elements. Although the crosstalk characteristics of arrays B and C are more complex than array A, crosstalk levels were still significantly affected by the distance between elements.

A second observation from the experimental results is that crosstalk properties depend on the frequency of the driven signal. Generally, crosstalk levels peaked at the resonant frequency of the transducer elements, and in some cases there were multiple maxima resulting from other resonant frequencies depending on array dimensions.

A third observation from the experimental results is that the relative placement of transducer elements in the array influences crosstalk levels. For inner transducer elements, crosstalk level is different than that for outer elements near the edge of the array, since the outer elements are more easily affected by the housing and less affected by the other elements than the inner elements are [36].

Research on crosstalk has shown that the choice of materials for the transducer elements and arrays has a significant impact on crosstalk levels [37]. The housing and surface-layer materials are key factors and contribute to multiple coupling paths. In

addition, the geometry of transducer arrays also influences crosstalk [37].

A fifth factor affecting crosstalk is the angle-of-arrival (AOA). Studies have shown that crosstalk and AOA are strongly coupled [38]. Waves impinging on transducer elements from different angles generate waves in different directions and change the induced crosstalk levels.

In summary, the crosstalk between transducer elements depends on element separation, the frequency and angle of the arriving signal, the relative location of elements in the array, and physical properties of the materials used to construct the array.

4.3 Impact of Crosstalk on Array Performance

Crosstalk between array elements distorts beam patterns and degrades AOA estimations for the incident signal. Therefore, in addition to characterizing crosstalk, it is important to analyze the impact of crosstalk on the beam pattern and angle estimation. In this section, degradation in array performance resulting from crosstalk is analyzed in three main parts. First, a theoretical crosstalk model is developed to predict the impact of crosstalk on array performance and is based on an admittance coupling matrix. Second, a method is shown that relates the elements in the coupling matrix to elements in the measured interaction matrix. In the third part, the theoretical model is compared with the experimental results for transducer arrays.

4.3.1 Theoretical Crosstalk Model

A theoretical model is constructed to illustrate the mechanism by which crosstalk affects the output signal of array elements. A transducer equivalent circuit is introduced as a prerequisite for the modelling.

4.3.1.1 Transducer Equivalent Circuit

Piezoelectric transducers can be modeled as an RLC circuit around resonance as shown in Figure 4.14 [8].

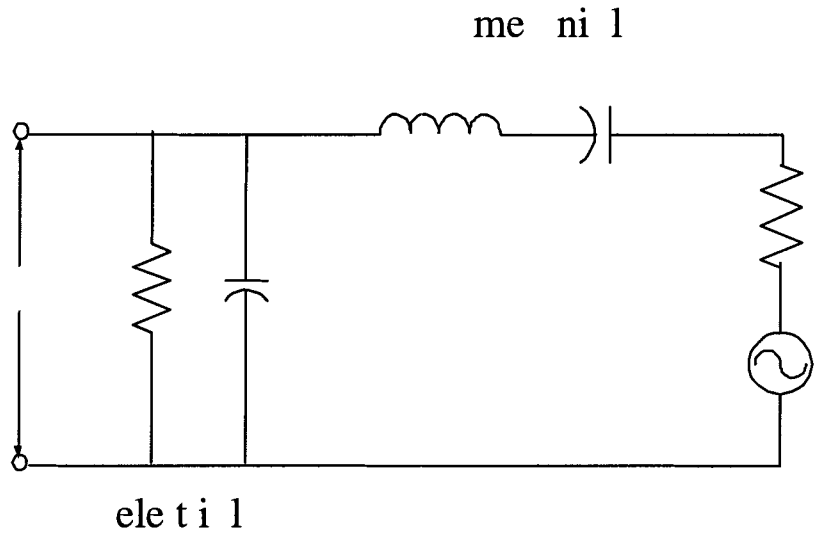

Figure 4.14: Equivalent circuit of a transducer

We analyze the circuit in Figure 4.14 as a hydrophone in the following analysis, which is also valid for a projector if the voltage source E is removed. E represents the result of an incident acoustic pressure on the hydrophone. The series arm, $L_1C_1R_1$, represents the mechanical impedance, where L_1 is the effective inductance, C_1 is the effective capacitance, and R_1 models the internal mechanical losses and radiation resistance. The parallel combination of R_0 and C_0 models the electrical characteristics of the transducer, where R_0 represents the electrical losses, and C_0 is the clamped capacitance of the transducer element. The transducer output voltage V_0 across resistor R_0 is generated from E. The electrical impedance of the transducer Z is complex and expressed as $Z = R + jX$, where R and X are the resistive and reactive components, respectively. For the subsequent analysis, it is more convenient to consider

the transducer in terms of its admittance Y rather than its impedance Z, where the conductance is G and the susceptance is B.

For the equivalent circuit shown in Figure 4.14, let the admittance of the series arm $L_1C_1R_1$ be Y_S and let the admittance of the parallel combination of R_0 and C_0 be Y_P, then

$$Y_S = \frac{1}{R_1 + j(wL_1 - \frac{1}{wC_1})}$$
$$Y_P = \frac{1}{R_0} + jwC_0 \tag{4.5}$$

The input admittance of the equivalent circuit referred to the electrical side is given by $Y = Y_S + Y_P$.

4.3.1.2 Array Crosstalk Model

A crosstalk model for a transducer array is developed below. In this model, it is assumed that 1) all array elements have the same electrical admittances; and 2) the crosstalk between equally spaced elements is identical. Figure 4.15 shows a three-element array where crosstalk coupling is represented by the admittances Y_1 and Y_2. Y_1 is the crosstalk admittance between adjacent elements, while Y_2 is the crosstalk admittance between the two outside elements. The individual series and parallel transducer admittances are Y_S and Y_P. This diagram is analyzed to compute the output voltages from each array element, V_1, V_2, and V_3, assuming an incident acoustic pressure E is acting on only the first element.

Nodal analysis is used to analyze the circuit in Figure 4.15, i.e. $\sum I_{in} = \sum I_{out}$. The current at each node is:

$$\begin{aligned}
&(Node\ \ 1) \quad Y_S(E - V_1) = Y_P V_1 + Y_1(V_1 - V_2) + Y_2(V_1 - V_3) \\
&(Node\ \ 2) \quad Y_1(V_1 - V_2) = (Y_S + Y_P)V_2 + Y_1(V_2 - V_3) \\
&(Node\ \ 3) \quad Y_1(V_2 - V_3) + Y_2(V_1 - V_3) = (Y_S + Y_P)V_3
\end{aligned} \tag{4.6}$$

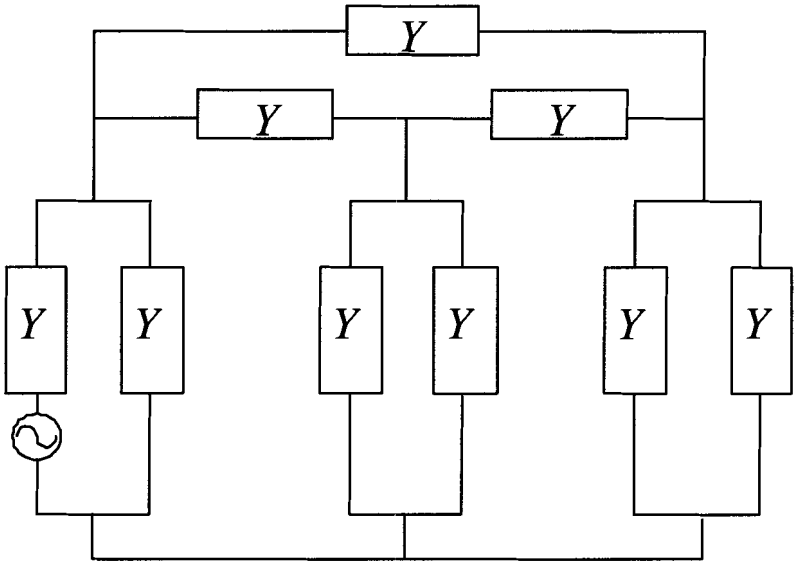

Figure 4.15: Crosstalk circuit model

Equation (4.6) is rewritten in matrix form as:

$$\frac{1}{Y_S}\begin{bmatrix} Y_S+Y_P+Y_1+Y_2 & -Y_1 & -Y_2 \\ -Y_1 & Y_S+Y_P+2Y_1 & -Y_1 \\ -Y_2 & -Y_1 & Y_S+Y_P+Y_1+Y_2 \end{bmatrix}\begin{bmatrix} V_1 \\ V_2 \\ V_3 \end{bmatrix} = \begin{bmatrix} E \\ 0 \\ 0 \end{bmatrix} \tag{4.7}$$

or

$$\mathbf{QX} = \mathbf{S} \tag{4.8}$$

where $\mathbf{Q}$ is the coupling matrix describing the coupling interference between elements, $\mathbf{X}=[V_1, V_2, V_3]^T$ is the vector of the output signals, and $\mathbf{S}=[E, 0, 0]^T$ is the incident signal on the array. Substituting $Y = Y_S + Y_P$ into $\mathbf{Q}$ gives:

$$\mathbf{Q} = \frac{1}{Y_S}\begin{bmatrix} Y+Y_1+Y_2 & -Y_1 & -Y_2 \\ -Y_1 & Y+2Y_1 & -Y_1 \\ -Y_2 & -Y_1 & Y+Y_1+Y_2 \end{bmatrix} \tag{4.9}$$

Assuming identical admittances for each element and identical crosstalk between equally spaced elements, it is easy to generalize $\mathbf{Q}$ for an N-element array. For example, for a six-element array, if Y_1 denotes the crosstalk admittance between a driven element and its first neighbor, and Y_2 denotes the crosstalk between an element and its second neighbor, and so on, then, $\mathbf{Q}$ is given by:

$$\mathbf{Q} = \frac{1}{Y_S}\begin{bmatrix} \mathbf{Q}_{11} & -Y_1 & -Y_2 & -Y_3 & -Y_4 & -Y_5 \\ -Y_1 & \mathbf{Q}_{22} & -Y_1 & -Y_2 & -Y_3 & -Y_4 \\ -Y_2 & -Y_1 & \mathbf{Q}_{33} & -Y_1 & -Y_2 & -Y_3 \\ -Y_3 & -Y_2 & -Y_1 & \mathbf{Q}_{44} & -Y_1 & -Y_2 \\ -Y_4 & -Y_3 & -Y_2 & -Y_1 & \mathbf{Q}_{55} & -Y_1 \\ -Y_5 & -Y_4 & -Y_3 & -Y_2 & -Y_1 & \mathbf{Q}_{66} \end{bmatrix} \tag{4.10}$$

where:

$$\begin{aligned} \mathbf{Q}_{11} &= \mathbf{Q}_{66} = Y + Y_1 + Y_2 + Y_3 + Y_4 + Y_5 \\ \mathbf{Q}_{22} &= \mathbf{Q}_{55} = Y + 2Y_1 + Y_2 + Y_3 + Y_4 \\ \mathbf{Q}_{33} &= \mathbf{Q}_{44} = Y + 2Y_1 + 2Y_2 + Y_3 \end{aligned} \tag{4.11}$$

From Equation (4.8), $\mathbf{X}$ is given by:

$$\mathbf{X} = \mathbf{Q}^{-1}\mathbf{S} \tag{4.12}$$

4.3.1.3 Impact of Crosstalk on the Beam Pattern and AOA Estimation

It is our goal to analyze the impact of crosstalk on the array beam pattern and compute the estimated error in measuring AOA using the crosstalk model in Equation (4.12). The analysis assumes the matrix $\mathbf{Q}$ is known, and in a later section, it is shown how an estimate $\widehat{\mathbf{Q}}$ of the matrix $\mathbf{Q}$ is found from the measured interaction matrix $\mathbf{\Gamma}$.

Assume an incident signal at angle θ is received by a symmetrical N-element transducer array. Each transducer element is modelled as a point source and it is

assumed no crosstalk between elements. The vector of incident signals corresponding to each transducer element is given by

$$\mathbf{S}(\phi) = a \begin{bmatrix} e^{-j\phi_0} \\ e^{-j(\phi+\phi_0)} \\ \vdots \\ e^{-j((N-1)\phi+\phi_0)} \end{bmatrix} = ae^{-j\phi_0} \begin{bmatrix} 1 \\ e^{-j\phi} \\ \vdots \\ e^{-j(N-1)\phi} \end{bmatrix} \tag{4.13}$$

In Equation (4.13), a is the magnitude of the signal, ϕ_0 is the phase of the signal incident at the first channel, ϕ is the phase difference of the arrival signal between neighboring elements, and is related to the angle θ by:

$$\phi = \frac{2\pi d}{\lambda} \sin\theta \tag{4.14}$$

where d is the space between array elements, and λ is the wavelength. Assuming that crosstalk characteristics do not change significantly and can be described by a matrix $\mathbf{Q}$, and also because the pattern shaping function is a cosine function as described in Chapter 2, the output signal vector from the array is then

$$\mathbf{X}(\phi) = \mathbf{Q}^{-1}\mathbf{S}(\phi)\cos(\theta) \tag{4.15}$$

For an N-element transducer array, if θ varies over an angular range of $[-90^o, 90^o]$ in steps of 1^o, $\mathbf{X}$ is a matrix with the dimension of $N \times 181$. The relative magnitudes of N row vectors of $\mathbf{X}$ determine the N beam patterns, while the phase differences ϕ between two row vectors are used to estimate AOAs in the range of $[-90^o, 90^o]$ with:

$$\widehat{\theta} = \arcsin\frac{\phi\lambda}{2\pi d} \tag{4.16}$$

It is important to emphasize that both the beam pattern and estimation of the incident signal angle are determined by *relative*, rather than *absolute*, measurements

obtained from the components of $\mathbf{X}$. Therefore, (4.15) can be multiplied by an arbitrary constant α without affecting the beam pattern or AOA estimation. As shown in section 4.3.2, the coupling matrix $\mathbf{Q}$ is estimated with a scale factor from the measured interaction matrix $\mathbf{\Gamma}$ and hence is consistent with the crosstalk model.

Given that the array output signals are modelled as shown in (4.15), the effect of crosstalk on array performance can be quantified by computing the average standard deviation of the beam pattern and AOA estimation over a range of incident angles [6]. In other words, the coupling matrix $\mathbf{Q}$ introduces amplitude and phase variations in the components of $\mathbf{X}$ and the average variation is defined as the standard deviation of the beam pattern (B) and AOA estimations ($\widehat{\theta}$) over incident angles in $[\theta_1, \theta_2]$. The standard deviation of the beam pattern e_B and the AOA estimation error e_θ are expressed as:

$$\begin{aligned} e_B &= \frac{1}{i_2 - i_1 + 1} \sum_{i=i_1}^{i_2} \sqrt{\frac{1}{N} \sum_{n=1}^{N} (B[n,i] - \bar{B}(i))^2} \\ e_\theta &= \frac{1}{i_2 - i_1 + 1} \sum_{i=i_1}^{i_2} \sqrt{\frac{1}{N-1} \sum_{n=1}^{N-1} (\widehat{\theta}[n,i] - \bar{\widehat{\theta}}(i))^2} \end{aligned} \tag{4.17}$$

where i_1 and i_2 are the indexes corresponding to θ_1 and θ_2, respectively; $\bar{B}$ and $\bar{\widehat{\theta}}$ are the means of N beam patterns and N-1 pairs of AOA estimations over incident angles of θ_1 to θ_2. Since crosstalk seems to depend on incident angle in the measured data, the interval $[\theta_1, \theta_2]$ is restricted to $\pm 40^o$ with hopes that crosstalk does not change significantly within this range.

Calculating the standard deviation with Equation (4.17) assumes that the N observations of arrays are random variables and uncorrelated, which they obviously are not. However, the standard deviation does give a measure of variation from a mean. It should be noted that the standard deviation is not used here in the statistical sense. We are simply using it as a measure of spread from an average value. In this sense,

it is a useful measurement even without its traditional interpretation, and indicates how much crosstalk affects the beam patterns and AOA estimations.

4.3.2 Estimating Coupling Matrix

The coupling matrix $\mathbf{Q}$ is required to predict the standard deviation of errors introduced in the beam pattern and AOA estimation. The matrix elements are admittances and in this section the unknown terms are related to the elements in the measured interaction matrix $\mathbf{\Gamma}$.

Figure 4.16 shows an equivalent circuit of the measurement method for a three-element array and it differs from the theoretical model shown earlier in Fig. 4.15. In the theoretical model, the voltage V_1 is different from the incident voltage E generated by an acoustic wave, while in the measurement, the incident voltage E is not used and instead a function generator is applied directly across the transducer element as shown in Fig 4.16. In other words, for measuring $\mathbf{\Gamma}$ the driven element's voltage is clamped by the signal generator and in calculating $\mathbf{Q}$ none of the element voltages are clamped. The objective now is to relate these two models so that $\mathbf{Q}$ can be determined from $\mathbf{\Gamma}$.

Applying Kirchhoff's Current Law to the measurement model gives:

$$\begin{aligned} &(Node\ \ 1) \qquad V_1 = E \\ &(Node\ \ 2) \qquad Y_1(V_1 - V_2) = (Y_S + Y_P)V_2 + Y_1(V_2 - V_3) \\ &(Node\ \ 3) \qquad Y_1(V_2 - V_3) + Y_2(V_1 - V_3) = (Y_S + Y_P)V_3 \end{aligned} \tag{4.18}$$

After substituting Y for the sum $Y_S + Y_P$ and letting $\mathbf{\Gamma}_{ki} = V_k/V_i$, nodes 2 and 3

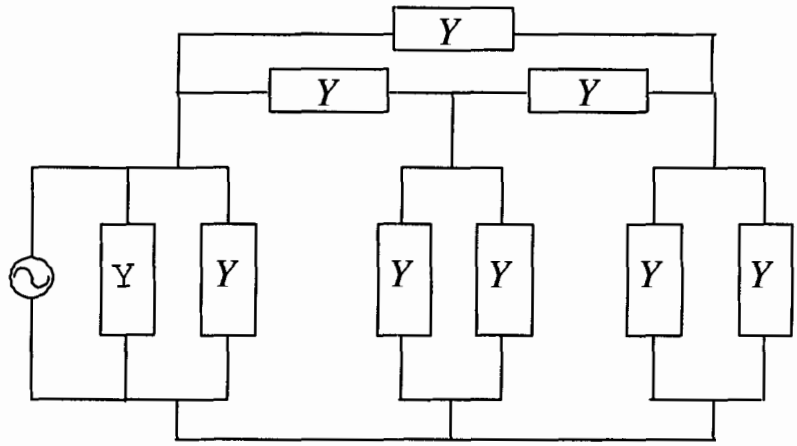

Figure 4.16: Circuit of crosstalk measurement

in (4.18) are expressed as:

$$\begin{aligned} (Node \quad 2) \qquad & -Y_1 + (Y + 2Y_1)\Gamma_{21} - Y_1\Gamma_{31} = 0 \\ (Node \quad 3) \qquad & -Y_2 - Y_1\Gamma_{21} + (Y + Y_1 + Y_2)\Gamma_{31} = 0 \end{aligned} \tag{4.19}$$

The equations in (4.19) are rearranged to solve for Y_1 and Y_2 yielding:

$$\begin{aligned} Y_1 &= \frac{\Gamma_{21}}{1 - 2\Gamma_{21} + \Gamma_{31}} Y \\ Y_2 &= \frac{\Gamma_{31} - \Gamma_{21}\Gamma_{31} + \Gamma_{31}^2 - \Gamma_{21}^2}{1 - 2\Gamma_{21} + 2\Gamma_{21}\Gamma_{31} - \Gamma_{31}^2} Y \end{aligned} \tag{4.20}$$

The equations of Y_1 and Y_2 are normalized by dividing by Y to get the relative admittances:

$$\begin{aligned} \frac{Y_1}{Y} &= \frac{\Gamma_{21}}{1 - 2\Gamma_{21} + \Gamma_{31}} \\ \frac{Y_2}{Y} &= \frac{\Gamma_{31} - \Gamma_{21}\Gamma_{31} + \Gamma_{31}^2 - \Gamma_{21}^2}{1 - 2\Gamma_{21} + 2\Gamma_{21}\Gamma_{31} - \Gamma_{31}^2} \end{aligned} \tag{4.21}$$

The crosstalk matrix $\mathbf{Q}$ shown in Equation (4.9) is rewritten as:

$$\mathbf{Q} = \frac{1}{Y_S}\begin{bmatrix} Y+Y_1+Y_2 & -Y_1 & -Y_2 \\ -Y_1 & Y+2Y_1 & -Y_1 \\ -Y_2 & -Y_1 & Y+Y_1+Y_2 \end{bmatrix}$$

$$= \frac{Y+Y_1+Y_2}{Y_S}\begin{bmatrix} 1 & -\frac{Y_1}{Y+Y_1+Y_2} & -\frac{Y_2}{Y+Y_1+Y_2} \\ -\frac{Y_1}{Y+Y_1+Y_2} & \frac{Y+2Y_1}{Y+Y_1+Y_2} & -\frac{Y_1}{Y+Y_1+Y_2} \\ -\frac{Y_2}{Y+Y_1+Y_2} & -\frac{Y_1}{Y+Y_1+Y_2} & 1 \end{bmatrix}$$

$$= \frac{1+Y_1/Y+Y_2/Y}{Y_S/Y}\begin{bmatrix} 1 & -\frac{Y_1/Y}{1+Y_1/Y+Y_2/Y} & -\frac{Y_2/Y}{1+Y_1/Y+Y_2/Y} \\ -\frac{Y_1/Y}{1+Y_1/Y+Y_2/Y} & \frac{1+2Y_1/Y}{1+Y_1/Y+Y_2/Y} & -\frac{Y_1/Y}{1+Y_1/Y+Y_2/Y} \\ -\frac{Y_2/Y}{1+Y_1/Y+Y_2/Y} & -\frac{Y_1/Y}{Y+Y_1/Y+Y_2/Y} & 1 \end{bmatrix} \tag{4.22}$$

If the constant α is defined as

$$\alpha = \frac{1+Y_1/Y+Y_2/Y}{Y_S/Y} \tag{4.23}$$

then the terms in $\mathbf{Q}$ depend only on the ratios Y_1/Y and Y_2/Y. Since the ratios are known in terms of the interaction matrix variables as given in (4.21), $\mathbf{Q}$ is known within an arbitrary complex constant α.

In section 4.3.1 it was shown that the beam pattern and AOA equations are unaffected by the multiplication of an arbitrary constant since relative vector components are used for determining these parameters. Hence, an estimate of $\mathbf{Q}$ denoted as $\widehat{\mathbf{Q}}$ is

found in terms of measurement variables and given by:

$$\widehat{\mathbf{Q}} = \begin{bmatrix} 1 & -\frac{Y_1/Y}{1+Y_1/Y+Y_2/Y} & -\frac{Y_2/Y}{1+Y_1/Y+Y_2/Y} \\ -\frac{Y_1/Y}{1+Y_1/Y+Y_2/Y} & \frac{1+2Y_1/Y}{1+Y_1/Y+Y_2/Y} & -\frac{Y_1/Y}{1+Y_1/Y+Y_2/Y} \\ -\frac{Y_2/Y}{1+Y_1/Y+Y_2/Y} & -\frac{Y_1/Y}{1+Y_1/Y+Y_2/Y} & 1 \end{bmatrix} \tag{4.24}$$

The same method can be generalized to an N-element transducer array except the expressions for the matrix elements in terms of the interaction matrix terms $\mathbf{\Gamma}_{ki}$ become more complex. MAPLE is employed to manipulate expressions for larger matrices and used to generate the results in subsequent sections.

The method for estimating the coupling matrix $\mathbf{Q}$ is valid only if the admittance of transducer elements and crosstalk between equally spaced elements in the array are identical. In the experimental arrays A, B, and C, the transducer elements are approximately the same, but the crosstalk between equally spaced elements is not always the same. As shown in Figures 4.11 - 4.13, the crosstalk phase between equally spaced elements differs in arrays B and C, while both the crosstalk magnitude and phase between equally spaced elements in array A are approximately same. Hence, the theoretical crosstalk model can be compared with measured results for array A, while arrays B and C will require a more complex model which is beyond the scope of this thesis. In the next section, the theoretical model is compared with experimental results for array A, and comments are made on the crosstalk characteristics of arrays B and C.

4.3.3 Comparing Crosstalk Model with Measurement Result

Before comparing the theoretical model of crosstalk with the measured results for array A, two hypothetical arrays denoted as D and E, are first considered to gain insight into the impact of crosstalk on array performance. In array D, the coupling

matrix is assumed to be symmetrical and consists of only adjacent element coupling Y_1, while in array E, additional coupling is modelled between each element and its second neighbor Y_2. A value of $0.1\angle(2/3\pi)Y$ is assumed for Y_1 and a value of $0.05\angle(4/3\pi)Y$ is assumed for Y_2. The coupling matrices for arrays D and E are:

$$\mathbf{Q}_D = \begin{bmatrix} 1+0.1e^{j2/3\pi} & -0.1e^{j2/3\pi} & 0 & 0 & 0 & 0 \\ -0.1e^{j2/3\pi} & 1+0.2e^{j2/3\pi} & -0.1e^{j2/3\pi} & 0 & 0 & 0 \\ 0 & -0.1e^{j2/3\pi} & 1+0.2e^{j2/3\pi} & -0.1e^{j2/3\pi} & 0 & 0 \\ 0 & 0 & -0.1e^{j2/3\pi} & 1+0.2e^{j2/3\pi} & -0.1e^{j2/3\pi} & 0 \\ 0 & 0 & 0 & -0.1e^{j2/3\pi} & 1+0.2e^{j2/3\pi} & -0.1e^{j2/3\pi} \\ 0 & 0 & 0 & 0 & -0.1e^{j2/3\pi} & 1+0.1e^{j2/3\pi} \end{bmatrix} \tag{4.25}$$

$$\mathbf{Q}_E = \begin{bmatrix} \mathbf{Q}_{E11} & -0.1e^{j2/3\pi} & -0.05e^{j4/3\pi} & 0 & 0 & 0 \\ -0.1e^{j2/3\pi} & \mathbf{Q}_{E22} & -0.1e^{j2/3\pi} & -0.05e^{j4/3\pi} & 0 & 0 \\ -0.05e^{j4/3\pi} & -0.1e^{j2/3\pi} & \mathbf{Q}_{E33} & -0.1e^{j2/3\pi} & -0.05e^{j4/3\pi} & 0 \\ 0 & -0.05e^{j4/3\pi} & -0.1e^{j2/3\pi} & \mathbf{Q}_{E44} & -0.1e^{j2/3\pi} & -0.05e^{j4/3\pi} \\ 0 & 0 & -0.05e^{j4/3\pi} & -0.1e^{j2/3\pi} & \mathbf{Q}_{E55} & -0.5e^{j2/3\pi} \\ 0 & 0 & 0 & -0.05e^{j4/3\pi} & -0.1e^{j2/3\pi} & \mathbf{Q}_{E66} \end{bmatrix} \tag{4.26}$$

where

$$\begin{aligned} \mathbf{Q}_{E11} &= \mathbf{Q}_{E66} = 1+0.1e^{j2/3\pi}+0.05e^{j4/3\pi} \\ \mathbf{Q}_{E22} &= \mathbf{Q}_{E55} = 1+2\times 0.1e^{j2/3\pi}+0.05e^{j4/3\pi} \\ \mathbf{Q}_{E33} &= \mathbf{Q}_{E44} = 1+2\times 0.1e^{j2/3\pi}+2\times 0.05e^{j4/3\pi} \end{aligned} \tag{4.27}$$

The beam patterns and angle-of-arrival estimations of arrays D and E are obtained by substituting $\mathbf{Q}_D$ and $\mathbf{Q}_E$ into Equation (4.15) and assuming that the inter-element spacing d is $\lambda/2$. The thing to note is that Equation (4.15) involves inverting $\mathbf{Q}$, which

results in $\mathbf{Q}_D^{-1}$ and $\mathbf{Q}_E^{-1}$ as

$$\mathbf{Q}_D^{-1} = \begin{bmatrix} 1.04e^{-j0.10} & 0.11e^{j1.80} & 0.01e^{-j2.59} & \epsilon_{D14} & \epsilon_{D15} & \epsilon_{D16} \\ 0.11e^{j1.80} & 1.07e^{-j0.20} & 0.12e^{j1.69} & 0.01e^{-j2.69} & \epsilon_{D25} & \epsilon_{D26} \\ 0.01e^{-j2.59} & 0.12e^{j1.69} & 1.07e^{-j0.20} & 0.12e^{j1.69} & 0.01e^{-j2.69} & \epsilon_{D36} \\ \epsilon_{D41} & 0.01e^{-j2.69} & 0.12e^{j1.69} & 1.07e^{-j0.20} & 0.12e^{j1.69} & 0.01e^{-j2.59} \\ \epsilon_{D51} & \epsilon_{D52} & 0.01e^{-j2.69} & 0.12e^{j1.69} & 1.07e^{-j0.20} & 0.11e^{j1.80} \\ \epsilon_{D61} & \epsilon_{D62} & \epsilon_{D63} & 0.01e^{-j2.59} & 0.11e^{j1.80} & 1.04e^{-j0.10} \end{bmatrix} \tag{4.28}$$

$$\mathbf{Q}_E^{-1} = \begin{bmatrix} 1.07e^{-j0.05} & 0.12e^{j1.85} & 0.07e^{-j2.29} & 0.02e^{-j0.35} & 0.01e^{j1.68} & \epsilon_{E16} \\ 0.12e^{j1.85} & 1.11e^{-j0.16} & 0.12e^{j1.74} & 0.08e^{-j2.40} & 0.02e^{-j0.51} & 0.01e^{j1.68} \\ 0.07e^{-j2.29} & 0.12e^{j1.74} & 1.15e^{-j0.11} & 0.12e^{j1.79} & 0.08e^{-j2.40} & 0.02e^{-j0.35} \\ 0.02e^{-j0.35} & 0.08e^{-j2.40} & 0.12e^{j1.79} & 1.15e^{-j0.11} & 0.12e^{j1.74} & 0.07e^{-j2.29} \\ 0.01e^{j1.68} & 0.02e^{-j0.51} & 0.08e^{-j2.40} & 0.12e^{j1.74} & 1.11e^{-j0.16} & 0.12e^{j1.85} \\ \epsilon_{Q61} & 0.01e^{j1.68} & 0.02e^{-j0.35} & 0.07e^{-j2.29} & 0.12e^{j1.85} & 1.07e^{-j0.05} \end{bmatrix} \tag{4.29}$$

where ϵ denotes the items too small to be represented with two significant digits. Compared to $\mathbf{Q}_D$ and $\mathbf{Q}_E$, $\mathbf{Q}_D^{-1}$ and $\mathbf{Q}_E^{-1}$ consist of more nonzero items in diagonals. This indicates that in addition to direct interference, there is also indirect interference between elements through neighboring elements in arrays D and E. However, it is the crosstalk from the adjacent and nearest two elements that dominate in arrays D and E, respectively. The beam pattern and AOA estimations predicted from Equation (4.15) are plotted in Figures 4.17 - 4.18, where the x axis represents the physical

angle of the signal θ in the range of $[-90^o, 90^o]$, and the y axis represents the beam pattern relative amplitude and estimated AOA, respectively.

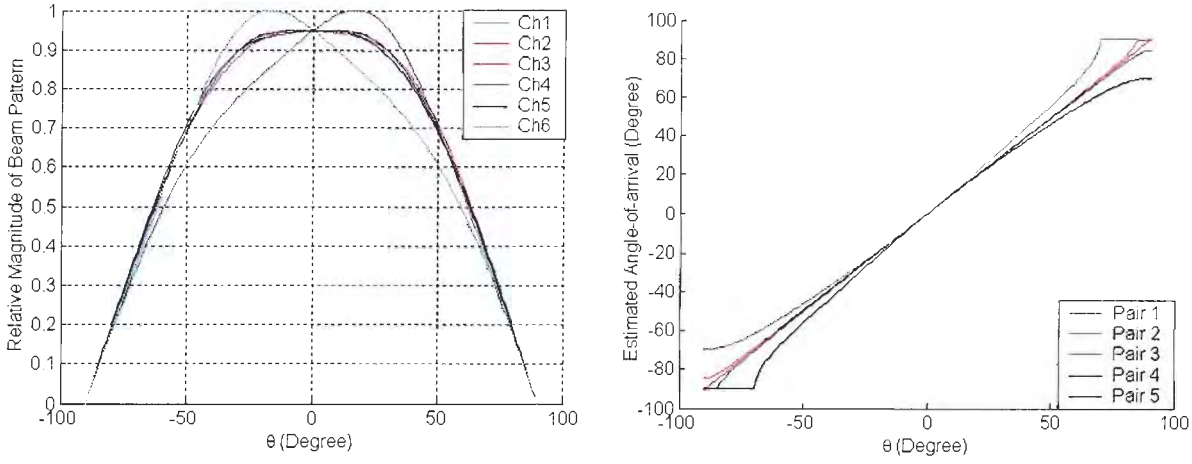

(a) (b)

Figure 4.17: The predicted (a) beam patterns and (b) AOA estimations of array D from $\mathbf{Q}_D$

In Figure 4.17, it is noticed that the beam patterns for the corresponding elements on each side of array D are mirror images of each other due to the symmetrical geometry and crosstalk in the array. The impact of crosstalk on the outer elements (1 and 6) is more significant than that on the inner elements (2, 3, 4 and 5). The beam patterns for elements 2, 3, 4 and 5 differ slightly since adjacent element coupling dominates in array D. Similar mirror images are evident in plots of estimated AOAs. For array E, in which crosstalk is significant not only between adjacent elements but also between elements spaced by one element, the variations in the beam patterns and AOAs of the inner four elements are larger than those of array D; and also, only the center two elements display approximately identical beam patterns in the range of $[-\pi/2, \pi/2]$ since a single driven element affects two neighboring elements on each side significantly.

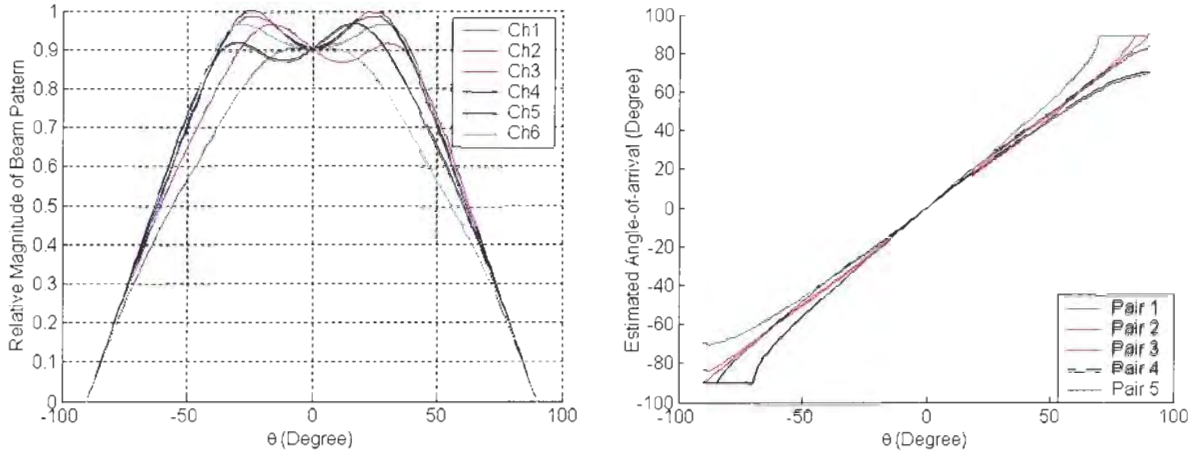

(a) (b)

Figure 4.18: The predicted (a) beam patterns and (b) AOA estimations of array E from $\mathbf{Q}_E$

It is evident from Figures 4.17 - 4.18 that with a symmetrical array structure and identical crosstalk between equally spaced elements, the beam patterns and estimated AOAs for the corresponding elements on each side are mirror images of each other. Only the beam patterns and AOAs of the outer elements are obviously affected if only one crosstalk source is dominant; if not only adjacent elements but also indirect neighboring elements strongly interfere each other, more elements are affected, and the level of the variation of the beam patterns and AOAs depends on the level of crosstalk.

The crosstalk effect on AOA estimations can be reduced by averaging the $N-1$ estimates of AOA for an N-element array, which reduces the error standard deviation by a square root of $N-1$, under the assumption that the N observations from each array are random variables and uncorrelated. For example, if five estimates are made for a six-element array, the spatial error rate can be reduced by $\sqrt{5}$ under the assumption that the six observations from each array are random variables and

uncorrelated. Again it is noted that the AOA estimations are not random variables and there is likely correlation between estimates. Nevertheless, averaging does reduce the spread and this is one measurement of what the resulting spread might be.

Equation (4.17) is used to compute the average variations of beam patterns and AOA errors over the range of $[-40^o, 40^o]$ for arrays D and E. The beam pattern variations are 4.22% and 4.97% respectively, and the AOA variations are 1.02^o, and 1.37^o, respectively. The resulting error in spatial position at a given range can be expressed as a percentage of range by expressing the error of AOAs in radians and multiplying by 100%. For arrays D and E, angular errors of 1.02^o and 1.37^o translate into errors of 1.78% and 2.39%, which correspond to spatial errors of 1.78 m and 2.39 m at a range of 100 m. Under the assumption that the six observations of arrays D and E are uncorrelated, the error to range ratios drop to 0.80% and 1.07% respectively.

The beam pattern and AOA estimations calculated from the theoretical crosstalk model and measurement results of array A are presented and compared below. The coupling matrix $\hat{\mathbf{Q}}_A$ is obtained from the experimental interactions with the result:

$$\hat{\mathbf{Q}}_A = \begin{bmatrix} \hat{\mathbf{Q}}_{A11} & -0.13e^{-j1.86} & -0.02e^{j0.22} & -0.01e^{-j2.05} & \epsilon_{A15} & \epsilon_{A16} \\ -0.13e^{-j1.86} & \hat{\mathbf{Q}}_{A22} & -0.13e^{-j1.86} & -0.02e^{j0.22} & -0.01e^{-j2.05} & \epsilon_{A26} \\ -0.02e^{j0.22} & -0.13e^{-j1.86} & \hat{\mathbf{Q}}_{A33} & -0.13e^{-j1.86} & -0.02e^{j0.22} & -0.01e^{-j2.05} \\ -0.01e^{-j2.05} & -0.02e^{j0.22} & -0.13e^{-j1.86} & \hat{\mathbf{Q}}_{A44} & -0.13e^{-j1.86} & -0.02e^{j0.22} \\ \epsilon_{A51} & -0.01e^{-j2.05} & -0.02e^{j0.22} & -0.13e^{-j1.86} & \hat{\mathbf{Q}}_{A55} & -0.13e^{-j1.86} \\ \epsilon_{A61} & \epsilon_{A62} & -0.01e^{-j2.05} & -0.02e^{j0.22} & -0.13e^{-j1.86} & \hat{\mathbf{Q}}_{A66} \end{bmatrix} \tag{4.30}$$

where

$$\begin{aligned}
\hat{\mathbf{Q}}_{A11} &= \hat{\mathbf{Q}}_{A66} = 1 + 0.13e^{-j1.86} + 0.02e^{j0.22} + 0.01e^{-j2.05} + \epsilon_{A15} + \epsilon_{A16} \\
\hat{\mathbf{Q}}_{A22} &= \hat{\mathbf{Q}}_{A55} = 1 + 2 \times 0.13e^{-j1.86} + 0.02e^{j0.22} + 0.01e^{-j2.05} + \epsilon_{A15} \\
\hat{\mathbf{Q}}_{A33} &= \hat{\mathbf{Q}}_{A44} = 1 + 2 \times 0.13e^{-j1.86} + 2 \times 0.02e^{j0.22} + 0.01e^{-j2.05}
\end{aligned} \tag{4.31}$$

The estimated beam patterns and AOAs, and those obtained from the measured data of array A are plotted in Figures 4.19 and 4.20. For both cases, the beam patterns and AOAs of the center four elements are approximately uniform and smooth, since the main source of crosstalk is from the adjacent element.

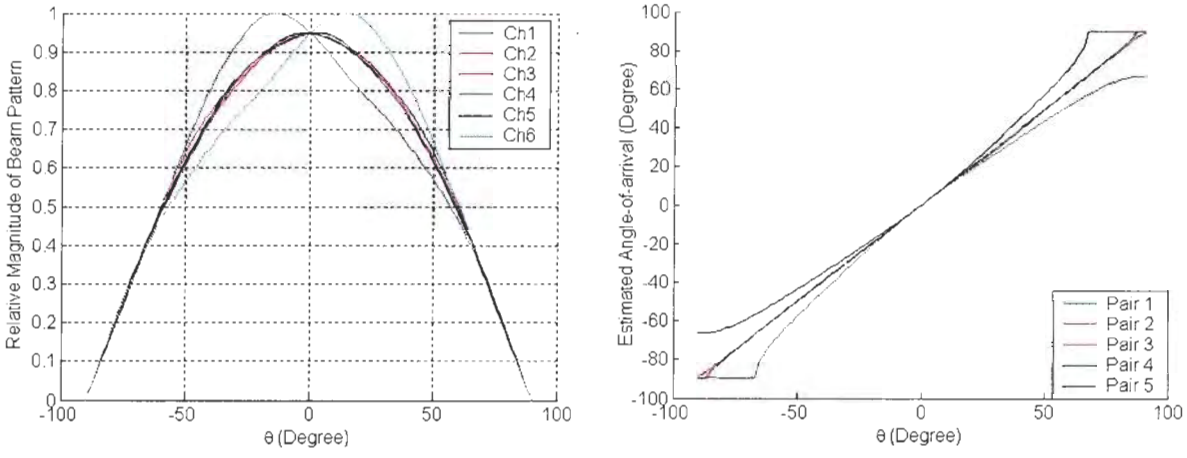

(a) (b)

Figure 4.19: The predicted (a) beam patterns and (b) AOA estimations of array A from $\hat{\mathbf{Q}}_A$

The variations of the beam patterns calculated from the theoretical models and the measured data are 5.06% and 4.56%, respectively; the corresponding spatial error rates are 2.20% and 2.22%, which can be reduced to 0.98% and 0.99% by averaging. Both the approximate shape of the beam pattern and estimated AOA, and the error margins for crosstalk approximately match the estimated values. The difference between estimated and experimental data probably is caused by a small housing effect

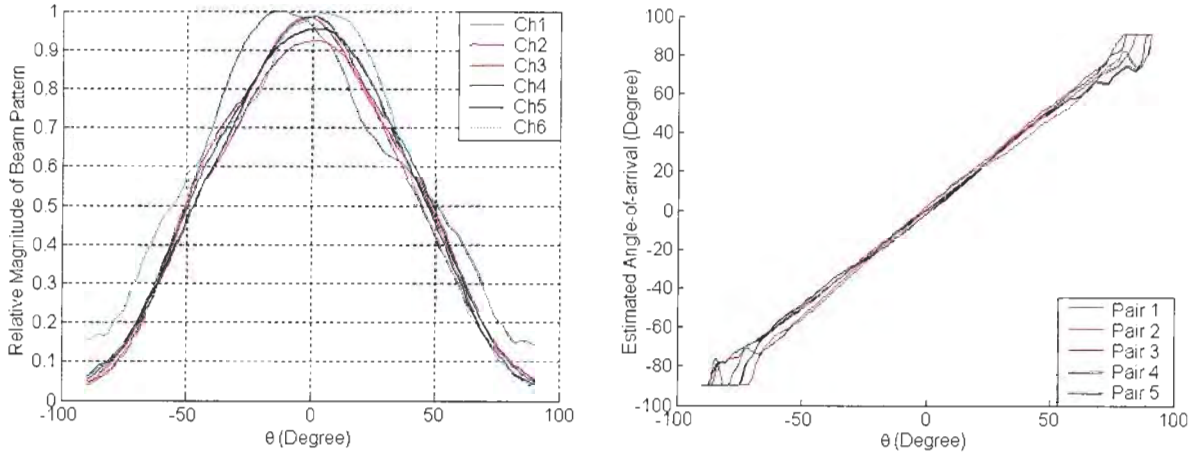

(a) (b)

Figure 4.20: The measured (a) beam patterns and (b) AOA estimations of array A

that is not considered here and the fact that crosstalk does change slightly in the range of angles $[-40^o, 40^o]$. Therefore, it is possible to predict the beam pattern and AOA variations using the interaction matrix $\mathbf{\Gamma}$ provided the crosstalk interactions are reasonably symmetrical, do not change much with angle, and boundary interactions are reasonably small. If these conditions are not met as in arrays B and C, at least we can identify this situation.

In the case of asymmetrical crosstalk, as in arrays B and C, Equation (4.17) is only used to quantify the variation of the beam patterns and estimated AOAs from the measured data. The measured beam patterns and estimated AOAs of arrays B and C at 300 kHz are plotted in Figures 4.21 - 4.22.

In Figure 4.21, the beam patterns and AOA estimations vary significantly over incident angles in the range of $[-90^o, 90^o]$. The large and frequent variation in these plots is due to significant crosstalk and multiple crosstalk sources. The average variation of the beam patterns and spatial error rate calculated from the actual output signals of array B are 9.30% and 8.02%, the latter of which translates into a spatial

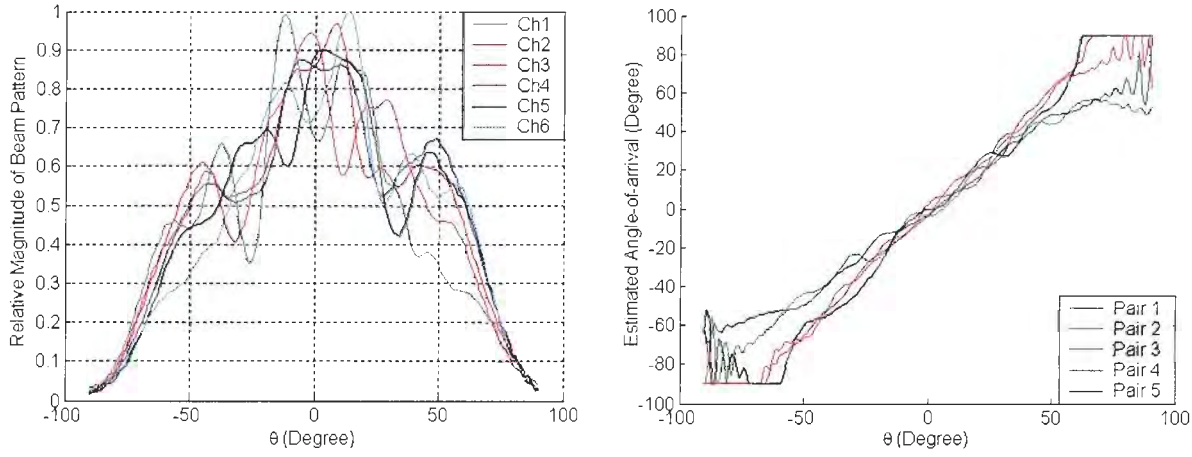

(a) (b)

Figure 4.21: The measured (a) beam patterns and (b) AOA estimations of array B

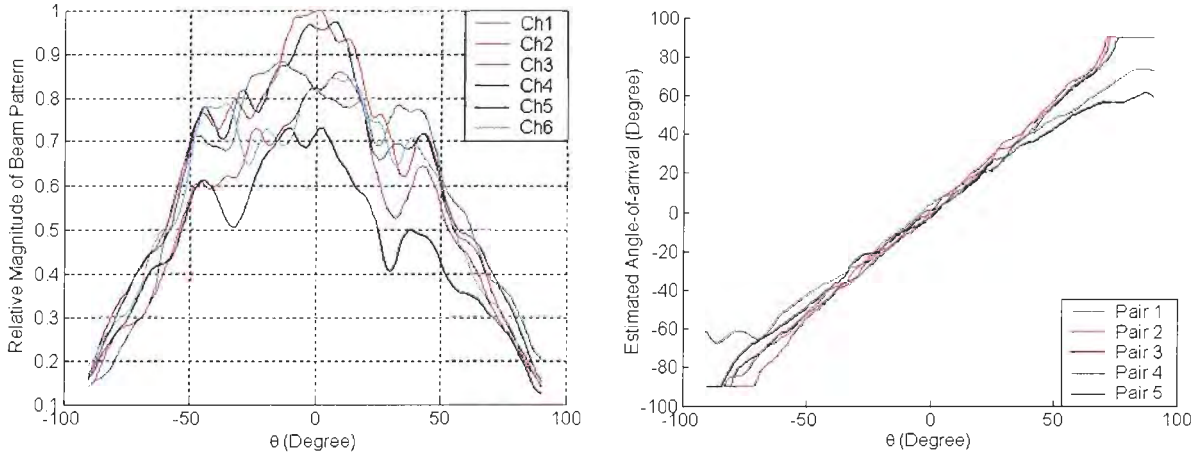

(a) (b)

Figure 4.22: The measured (a) beam patterns and (b) AOA estimations of array C

error of 8.02 m at a range of 100 m.

As shown in Figure 4.22 for array C, crosstalk levels affect the integrity of the beam pattern and estimation accuracy of AOA. Similarly, over a range of incident angles spanning $\pm 40^{o}$, the average variation of the beam patterns and spatial error rate of array C are 9.96% and 5.21%.

Spatial errors can be reduced further by averaging. Therefore, the spatial error rates obtained from the measurements of arrays B and C would drop to 3.59%, and 2.33%, respectively.

Chapter 5

Conclusions and Future Work

The main results of this thesis are reviewed in this chapter, and some general conclusions are drawn, followed by proposed future work.

5.1 Conclusions

The focus of this research was to experimentally investigate the performance of underwater acoustic transducer arrays in terms of the beam pattern, inter-element spacing, and crosstalk for the special application of MASB sonars. Experimental and analytic methods were shown and applied to characterize the performance of three transducer arrays: array A built by the Underwater Research Lab, array B by Simrad, and array C by Benthos.

A Beam Pattern Measurement System developed by the Underwater Research Lab was used to measure the beam patterns, aperture functions, and angle-of-arrival estimations for the three arrays. Improvements to the measurement system have been made since it was last documented [17] and the updated system was described in Chapter 2. The system now includes a function to estimate inter-element spacing, a graphical user interface, and updated hardware, and the results presented in this work are the first published work to take advantage of the upgraded beam pattern

system.

In Chapter 3, a method to estimate the inter-element spacing of an array by taking the inverse Fourier Transform of measured beam patterns was shown. Prior methods relied on manufacturer data, and with the proposed method, inter-element spacing can be accurately characterized independent of the manufacturer. Close agreement was obtained between design and measured inter-element spacing with the difference being 3.7%, 4%, and 3.33%, for arrays A, B, and C respectively. The transform method with beam pattern data avoids making physical measurements of the element placement in the array and yields similar measurement accuracy (± 0.01 cm).

Crosstalk significantly affects array performance and prior methods for evaluating array crosstalk required complicated mathematical models which included geometrical, material and environmental information. In Chapter 4, an experimental method was proposed to examine crosstalk by exciting an element and measuring coupled signals on other non-excited array elements. The crosstalk measurements are easily made in a laboratory and the measurement results were further utilized in a crosstalk model to predict the impact of crosstalk on array performance with some limitations. A theoretical crosstalk model was based on the synthesis of a coupling matrix which used experimental data to compute model values without specific knowledge of the transducer impedance, transducer size, or array geometry. In the model, the crosstalk between equally spaced elements is assumed to be the same and the coupling matrix is symmetrical. The crosstalk model was used to predict the impact of crosstalk on beam patterns and angle-of-arrival estimations for array A and the modelled results were compared with experimental results. The close agreement between the modelled and measured results demonstrated the usefulness of the theoretical model. Crosstalk measurements were also made on asymmetrical arrays (B and C) and it was shown

that a more complex theoretical model is required to predict the impact of crosstalk with asymmetrical arrays.

5.2 Future Work

There are a couple of areas where the research on array crosstalk could be extended.

The first area for future research is to model asymmetrical crosstalk effects on array performance. The model developed in this thesis assumed that the equally spaced elements have identical crosstalk coupling and in some array designs, like arrays B and C, this assumption is not valid. A more comprehensive model could be developed to model both symmetrical and asymmetrical crosstalk characteristics.

A second area for future research is to consider how a crosstalk model could be utilized in signal processing to improve the accuracy of beam pattern and angle-of-arrival estimation. Using such a crosstalk model in sonar system signal analysis should improve system accuracy by compensating for crosstalk effects.

Appendix A

Figures of Crosstalk Measurement

The relative magnitude and phase of interaction between all elements of arrays B and C are plotted in Figures A.1 - A.12.

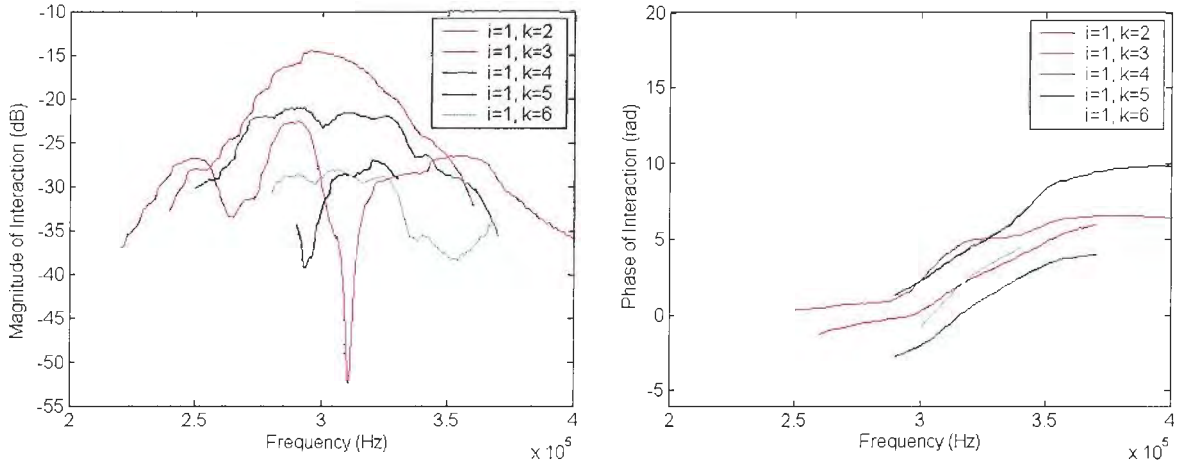

(a) (b)

Figure A.1: (a) Magnitude and (b) phase of interaction in array B when i=1

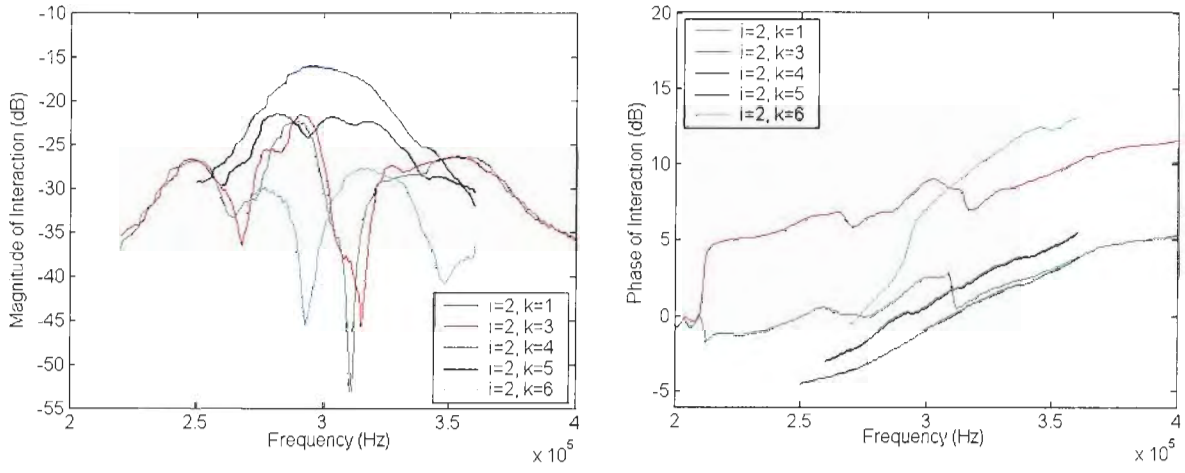

(a) (b)

Figure A.2: (a) Magnitude and (b) phase of interaction in array B when i=2

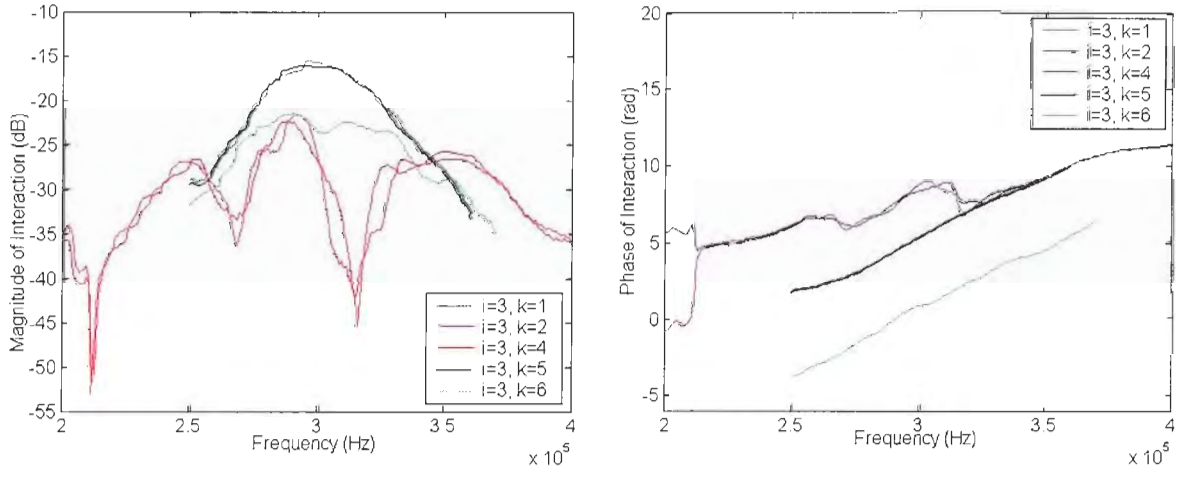

(a) (b)

Figure A.3: (a) Magnitude and (b) phase of interaction in array B when i=3

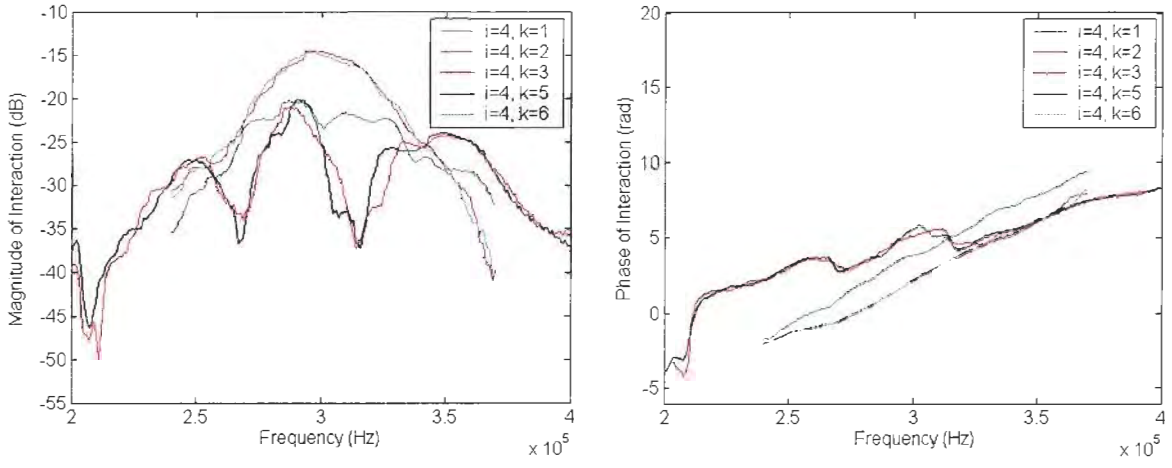

(a) (b)

Figure A.4: (a) Magnitude and (b) phase of interaction in array B when i=4

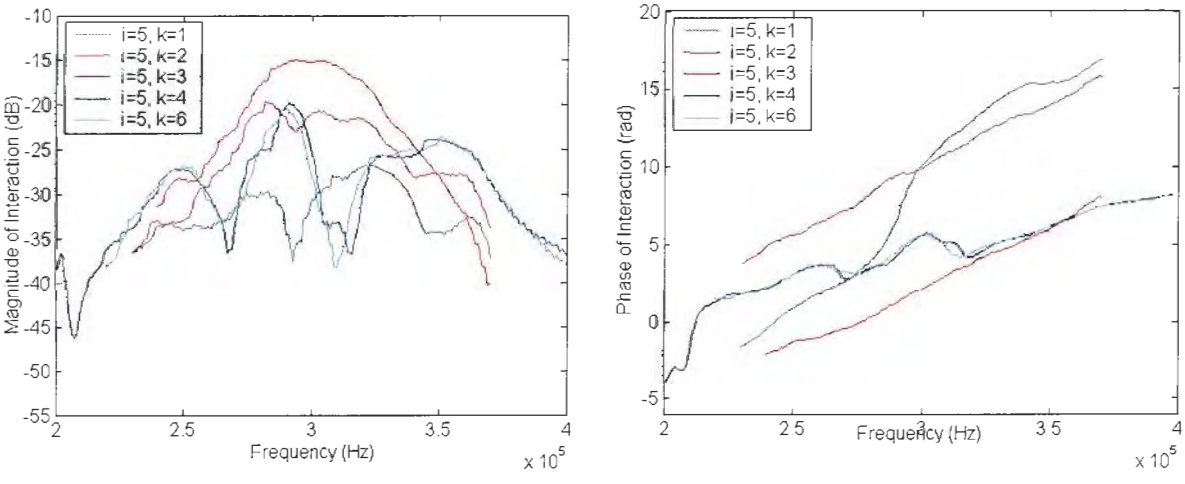

(a) (b)

Figure A.5: (a) Magnitude and (b) phase of interaction in array B when i=5

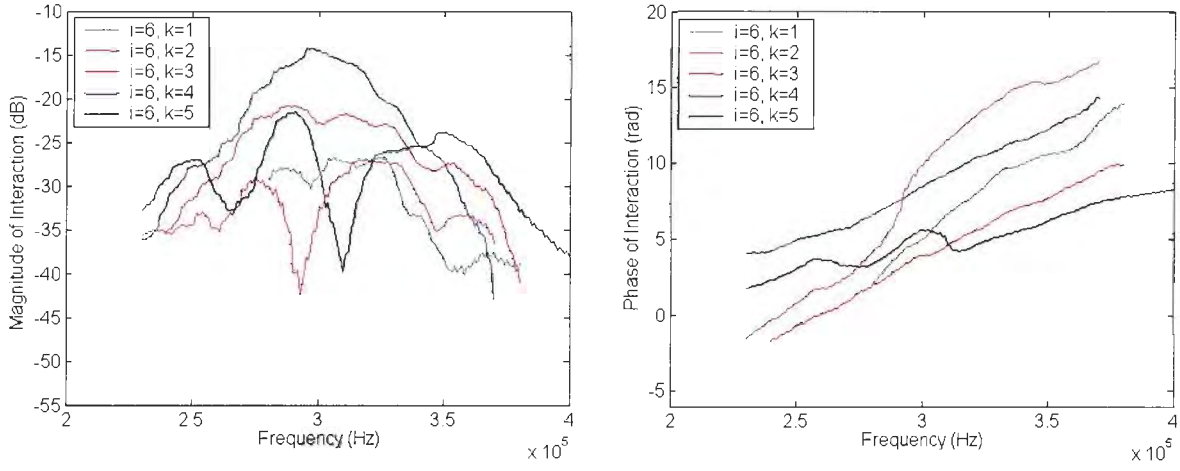

(a) (b)

Figure A.6: (a) Magnitude and (b) phase of interaction in array B when i=6

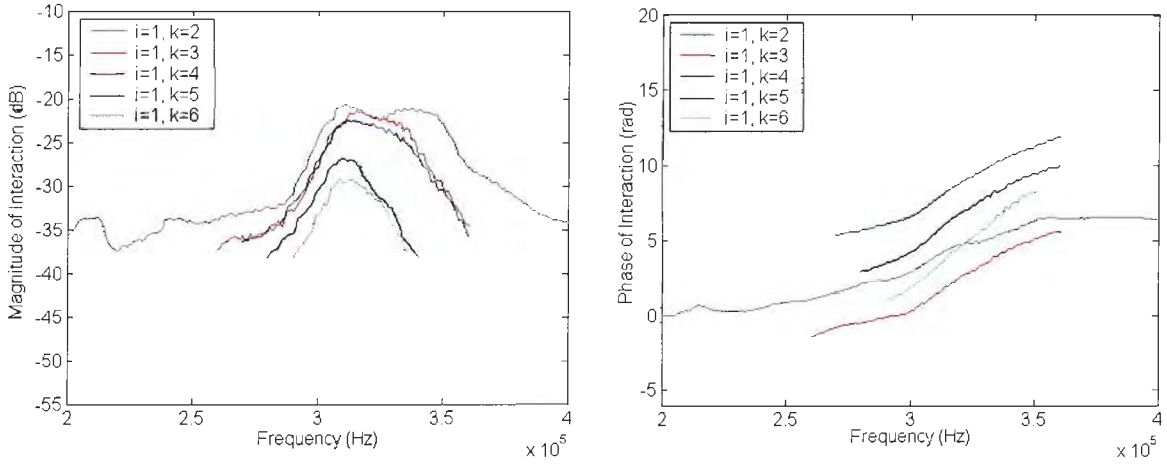

(a) (b)

Figure A.7: (a) Magnitude and (b) phase of interaction in array C when i=1

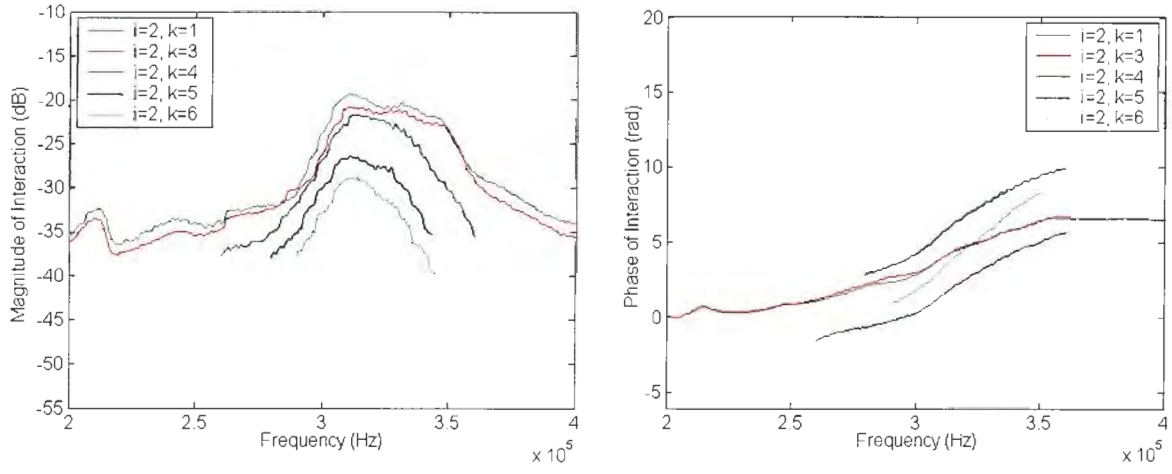

(a) (b)

Figure A.8: (a) Magnitude and (b) phase of interaction in array C when i=2

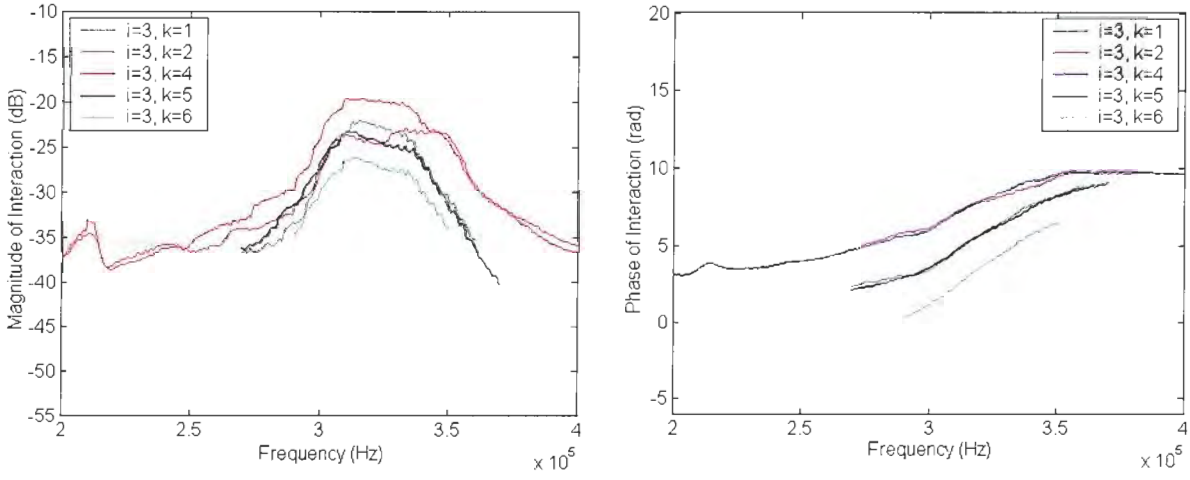

(a) (b)

Figure A.9: (a) Magnitude and (b) phase of interaction in array C when i=3

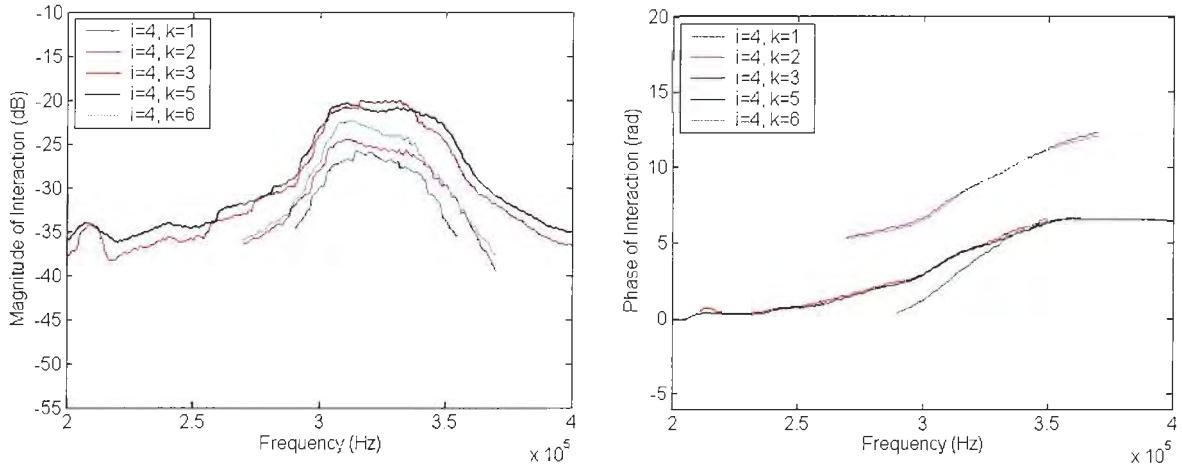

(a) (b)

Figure A.10: (a) Magnitude and (b) phase of interaction in array C when i=4

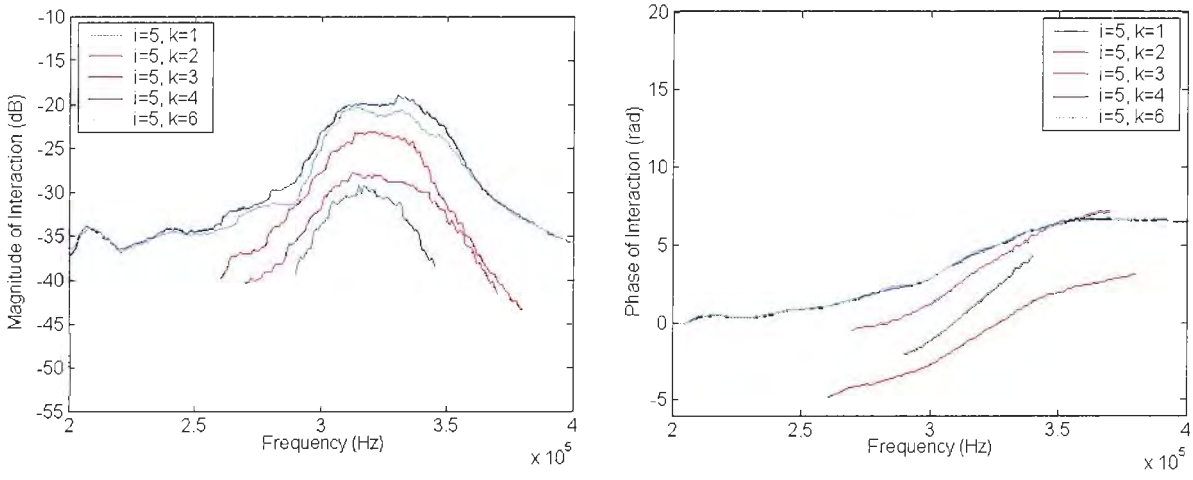

(a) (b)

Figure A.11: (a) Magnitude and (b) phase of interaction in array C when i=5

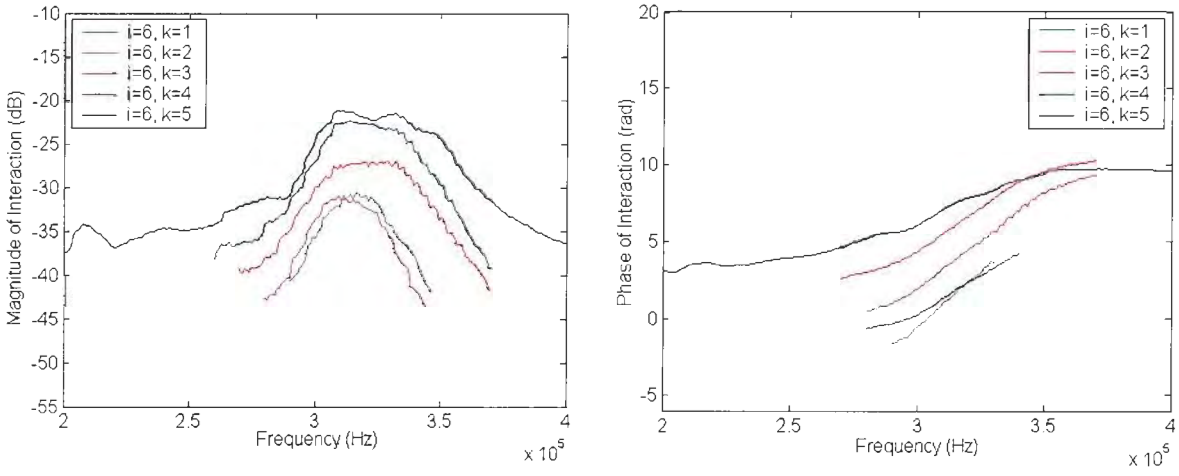

(a) (b)

Figure A.12: (a) Magnitude and (b) phase of interaction in array C when i=6

Bibliography

[1] Anderson V., "Acoustic Communication is Better than None", *IEEE Spectrum*, vol.7, pp. 63-68, Oct. 1970.

[2] Paul H. Kraeutner and J. S. Bird, "Seafloor Scatter Induced Angle of Arrival Errors in Swath Bathymetry Sidescan Sonar", in *OCEANS '95. MTS/IEEE Conference Proceedings*, vol.2, pp. 975-980, Oct. 1995.

[3] Paul H. Kraeutner and J. S. Bird, "Cramer-Rao Bound Investigation of Swath Bathymetry Accuracy", in *OCEANS'01 MTS/IEEE Conference and Exhibition*, vol.3, pp. 1640-1647, Nov. 2001.

[4] Xavier Lurton, "Swath Bathymetry Using Phase Difference: Theoretical Analysis of Acoustical Measurement Precision", *IEEE Journal of Oceanic Engineering*, vol.25, pp. 351-363, July 2000.

[5] Reinhard Lerch, "Simulation of Piezoelectric Devices by Two- and Three-Dimensional Finite Elements", *IEEE Transactions on Ultrasonics, Ferroelectrics, and Frequency Control*, vol.37, pp. 233-247, May 1990.

[6] John S.Bird, Sabir Asadov and Paul Kraeutner, "Improving Arrays for Multi-Angle Swath Bathymetry", in *Oceans 2003. Proceedings*, vol.4, pp. 2085-2092, Sept. 2003.

[7] Seambeam Intruments Technical Staff, *Communications SeaBeam Instruments*, Seabeam Instruments, 2003.

[8] William S. Burdic, "Underwater Acoustic System Analysis", *Prentice Hall*, 1991.

[9] D. Stansfield, "Underwater Electroacoustic Transducers", *Bath University Press and Institute of Acoustics*, 1991.

[10] P. H. Kraeutner and J. S. Bird, "Principal Components Array Processing for Swath Acoustic Mapping", in *Oceans'97. MTS/IEEE Conference Proceeding*, vol.2, pp. 1246-1254, Oct. 1997.

[11] Matt Geen, "Applications of Interferometric Swath Bathymetry", in *Oceans'98 Conference Proceedings*, vol.2, pp. 1126-1130, Sept. 1998.

[12] P.H.Kraeutner and J.S.Bird, "Beyond Interferometry, Resolving Multiple Angles-of-Arrival in Swath Bathymetric Imaging", *OCEANS'99. MTS/IEEE Conference Proceedings*, vol.1, pp. 37-45, Sept. 1999.

[13] P. H. Kraeutner and J. S. Bird, "Multi-Angle Swath Bathymetry Sidescan Quantitative Performance Analysis", *Oceans*, vol.4, pp. 2253-2263, Oct. 2002.

[14] B. Delannoy, H. Lasota, C. Brunnel, R. Torguet, and E. Bridoux, "The infinite planar baffles problem in acoustic radiation and its experimental verification", *Journal of Applied Physics*, pp. 5189-5195, Aug. 1979.

[15] http://www.rpaelectronics.com.

[16] http://www.ics-ltd.com.

[17] Pavel Haintz, "Multi Channel Coherent Beam Pattern Measurement System", M. Eng. project, Simon Fraser University, Burnaby, BC, Canada, 2003.

[18] http://www.simrad.com.

[19] http://www.benthos.com.

[20] Interactive Circuits and System Ltd., "The ICS-645 32-Channel, High Speed, High Precision PCI Bus ADC Board", *Technical Reporting From ICS*, No.38 Rev.D, Nov. 2000.

[21] Dion C. M. Horvat, John S. Bird, and Martie M.Goulding, "True Time-Delay Bandpass Beamforming", *IEEE Journal of Oceanic Engineering*, vol.17, pp. 185-192, April 1992.

[22] Hulin Liu, Arif Ghafoor, and Peter H.Stockmann, "A New Quadrature Sampling and Processing Approach", *IEEE Transactions on Aerospace and Electronic Systems*, vol.25, pp. 733-748, Sep. 1989.

[23] Michael Sayer, and Abhai Mansingh, "Measurement, Instrumentation and Experiment Design in Physics and Engineering", *Prentice Hall*, 2000.

[24] Earl G.LeDet, and Claudio I.Zanelli, "A Novel, Rapid Method to Measure the Effective Aperture of Array Elements", in *IEEE Ultrasonics Symposium*, vol.2, pp. 1077-1080, Oct. 1999.

[25] Xiao Peng, and Feng Zhenghe, "A Pattern Synthesis Method for Linear Array Considering Mutual Coupling Effect", in *2002 3rd International Conferences on Microwave and Millimeter Wave Technology Proceedings*, pp. 676-680, 2002.

[26] K.Kirk Shung and Michael Zipparo, "Ultrasonic Transducers and Arrays", *IEEE Engineering in Medicine and Biology*, vol.15, pp. 20-30, 1996.

[27] J. F. Dias, "An experimental investigation of the crosscoupling between elements of an acoustic imaging array transducer", *Ultrasonic Imaging*, vol.4, pp. 44-55, 1982.

[28] J. D. Larson, "A new vibration mode in tall, narrow piezoelectric elements", in *IEEE Ultrasonics Symposium Proceedings*, vol.51, pp. 108-113, 1979.

[29] Y. Gorfu, G. Hayward and D. D. N. Hall, "Theoretical and experimental evaluation of a two dimensional composite matrix array", *IEEE Ultrasonics Symposium*, vol.2, pp. 781-784, Dec. 1990.

[30] Shiwei Zhou, Gregory L. Wojcik, and John A. Hossack, "An Approach for Reducing Adjacent Element Crosstalk in Ultrasound Arrays", *IEEE Transactions on Ultrasonics, Ferroelectrics, and Frequency Control*, vol.50, pp. 1752-1761, Dec. 2003.

[31] A. Manikas and N. Fistas, "Modelling and Estimation of Mutual Coupling Between Array Elements", in *1994 IEEE International Conference on Acoustics, Speech, and Signal Processing*, vol.IV, pp. 553-556, April 1994.

[32] NLamberti, N., Gori P., Caliano G., Iula A., C arotenuto R., and Pappalardo M., "Radiation Pattern Distortion Caused by the Interelement Coupling in Linear Array Transducers", in *1999 IEEE Ultrasonics Symposium*, vol.2, pp. 1071-1075, Oct. 1999.

[33] J. F. Guess, C. G. Oakley, S. J. Douglas, and R. D. Morgan, "Cross-talk Paths in Array Transducers", in *IEEE Ultrasonics Symposium*, vol.2, pp. 1279-1282, Nov. 1995.

[34] Mikael Wilm, Raphael Armati, William Daniau, and Sylvain Ballandras, "Cross-talk phenomena in a 1-3 connectivity piezoelectric composite", *The Journal of the Acoustic Society of America*, vol.116, pp. 2948-2955, Nov. 2004.

[35] Stuart A. Long, Robert J. Dorris, and Russell Long, "Mutual Coupling between Cylindrical, Probe-Fed Dielectric Resonator Antennas", in *Antennas and Wireless Propagation Letters*, vol.1, pp. 8-9, 2002.

[36] Xiao Peng, and Feng Zhenghe, "A Pattern Synthesis Method for Linear Array Considering Mutual Coupling Effect", in *2002 3rd International Conference on Microwave and Millimeter Wave Technology*, pp. 676-680, 2002.

[37] Carlos Negreira, Hector Gomez, Nicolas Perez, and Ismael Nunez, "Lateral Modes and Diffracted Field Behavior in Non-periodical 1-3 Piezocomposite Transducers", in *IEEE Ultrasonics Symposium*, vol.1, pp. 641-644, Oct. 1998.

[38] B. Wang, Y. Wang, and Y. Guo, "Mutual coupling calibration with instrumental sensors", *Electronics Letters*, vol.40, pp. 406-408, April 2004.